HZDR-102

TRANSVERSE ELECTRON BEAM DYNAMICS IN THE BEAM LOADING REGIME

Alexander Köhler

Wissenschaftlich-Technische Berichte
HZDR-102 · ISSN 2191-8708

WISSENSCHAFTLICH-
TECHNISCHE BERICHTE

HZDR
HELMHOLTZ
ZENTRUM DRESDEN
ROSSENDORF

Wissenschaftlich-Technische Berichte
HZDR-102

Alexander Köhler

TRANSVERSE ELECTRON BEAM DYNAMICS IN THE BEAM LOADING REGIME

HZDR

HELMHOLTZ
ZENTRUM DRESDEN
ROSSENDORF

Druckausgabe: ISSN 2191-8708

Elektronische Ausgabe: ISSN 2191-8716

https://www.hzdr.de/publications/Publ-29299

urn:nbn:de:bsz:d120-qucosa2-343938

Die vorliegende Arbeit wurde sowohl als Dissertation an der Fakultät Mathematik und Naturwissenschaften der Technischen Universität Dresden sowie als Wissenschaftlich-Technischer Bericht des Helmholtz-Zentrum Dresden – Rossendorf mit der Berichtsnummer **HZDR-102** veröffentlicht.

2019

Herausgegeben vom

Helmholtz-Zentrum Dresden - Rossendorf

Bautzner Landstraße 400

01328 Dresden

Germany

Wissenschaftlich-Technische Berichte
HZDR-102

Alexander Köhler

TRANSVERSE ELECTRON BEAM DYNAMICS IN THE BEAM LOADING REGIME

HZDR

HELMHOLTZ
ZENTRUM DRESDEN
ROSSENDORF

Druckausgabe: ISSN 2191-8708

Elektronische Ausgabe: ISSN 2191-8716

https://www.hzdr.de/publications/Publ-29299

urn:nbn:de:bsz:d120-qucosa2-343938

Die vorliegende Arbeit wurde sowohl als Dissertation an der Fakultät Mathematik und Naturwissenschaften der Technischen Universität Dresden sowie als Wissenschaftlich-Technischer Bericht des Helmholtz-Zentrum Dresden – Rossendorf mit der Berichtsnummer **HZDR-102** veröffentlicht.

2019

Herausgegeben vom

Helmholtz-Zentrum Dresden - Rossendorf

Bautzner Landstraße 400

01328 Dresden

Germany

TECHNISCHE UNIVERSITÄT DRESDEN

HZDR
HELMHOLTZ ZENTRUM DRESDEN ROSSENDORF

Faculty of Science
Department of Physics

Institute of Radiation Physics
Laser Particle Acceleration Division

TRANSVERSE ELECTRON BEAM DYNAMICS IN THE BEAM LOADING REGIME

Dipl.-Phys. Alexander Köhler
Born on: 21st October 1986 in Sebnitz

DISSERTATION

to achieve the academic degree

DOCTOR RERUM NATURALIUM (DR. RER. NAT.)

First referee
Prof. Dr. Ulrich Schramm

Second referee
Prof. Dr. Thomas Cowan
Prof. Dr. Michael C. Downer

Supervisor
Dr. Arie Irman

Submitted on: 28th January 2019
Defended on: 21st May 2019

DRESDEN concept
Exzellenz aus Wissenschaft und Kultur

Für meine Familie und meine Freunde.

ABSTRACT

GeV electron bunches accelerated on a centimeter scale device exemplify the extraordinary advances of laser-plasma acceleration. The combination of high charges from optimized injection schemes and intrinsic femtosecond short bunch duration yields kiloampere peak currents. Further enhancing the current while reducing the energy spread will pave the way for future applications, e.g. drivers for compact secondary radiation sources such as high-field THz, high-brightness x-ray or γ-ray sources. One essential key for beam transport to a specific application is an electron bunch with high quality beam parameters such as low energy spread as well as small divergence and spot size. The inherent micrometer beam diameter at the plasma exit is typically sufficient for an efficient coupling into a conventional beamline. However, energy spread and beam divergence require optimization before the beam can be transported efficiently. Induced by the high peak current, the beam loading regime can be used in order to achieve optimized beam parameters for beam transport.

In this thesis, the impact of beam loading on the transverse electron dynamic is systematically studied by investigating betatron radiation and electron beam divergence. For this reason, the bubble regime with self-truncated ionization injection (STII) is applied to set up a nanocoulomb-class laser wakefield accelerator. The accelerator is driven by 150 TW laser pulses from the DRACO high power laser system. A supersonic gas jet provides a 3 mm long acceleration medium with electron densities from $3 \times 10^{18}\,\mathrm{cm}^{-3}$ to $5 \times 10^{18}\,\mathrm{cm}^{-3}$. The STII scheme together with the employed setup yields highly reproducible injections with bunch charges of up to 0.5 nC. The recorded betatron radius at the accelerator exit is about one micron and reveals that the beam size stays at the same value. The optimal beam loading, which is observed at around 250 pC to 300 pC, leads to the minimum energy spread of $\sim$40 MeV and a 20 % smaller divergence. It is demonstrated that an incomplete betatron phase mixing due to the small energy spread can explain the experimentally observed minimum beam divergence.

KURZFASSUNG

Elektronen mit einer kinetischen Energie im Gigaelektronenvolt-Bereich, beschleunigt in einem nur wenige Zentimeter-langen Plasmakanal, kennzeichnen die außergewöhnlichen Fortschritte in der Laser-Teilchen-Beschleunigung. Die kurze Beschleunigungsstrecke beruht auf den hohen Feldstärken von typischerweise GV/m, die im Plasmakanal entstehen können. Die Kombination aus großer Strahlladung und der intrinsischen, kurzen Pulsdauer führt zu Spitzenströmen im Kiloampere-Bereich. Eine weitere Erhöhung des Strahlstromes bei gleichzeitiger Verkleinerung der Energiebreite wird den Weg für neue Anwendungen ebnen: Zum Beispiel als Antrieb für kompakte Sekundärstrahlungsquellen wie Hochfeld-THz, superhelle Röntgen- oder Gammastrahlungsquellen. Eine essentielle Voraussetzung für den Strahltransport zu spezifischen Anwendungen ist eine hohe Qualität der erzeugten Teilchenpakete, das heißt eine geringe Energiebreite bei einer kleinen Strahlemittanz. Der typischerweise nur Mikrometer-große Strahldurchmesser am Plasmakanalende ist ausreichend für eine effiziente Strahlkopplung in konventionelle Strahlführungssysteme. Allerdings müssen die Energiebreite und Strahldivergenz für einen effizienten Strahltransport angepasst werden. Die extrem hohen Ladungen, die mit dem Beschleuniger erreichbar sind, erzeugen ein Coulomb-Feld welches die Plasmafelder überlagert. In diesem Fall spricht man von Beam-Loading, weil die Beschleunigungsfelder signifikant verändert werden. Beam-Loading kann genutzt werden um die Strahlparameter für den Strahtransport zu optimieren.

In der vorliegenden Arbeit wird der Einfluss von Beam-Loading auf die transversale Strahldynamik systematisch studiert. Dazu wird die Betatronstrahlung und die Divergenz des Elektronenstrahls untersucht. Um die nötigen hohen Ladungen der beschleunigten Elektronenpakete für Beam-Loading zu erhalten wird ein Beschleuniger der Nanocoulomb-Klasse aufgebaut und Elektronen werden durch Self-Truncated-Ionization (STII) injiziert. Der 150 TW-Arm des DRACO Hochintensitätslasers dient als Antrieb für den Beschleuniger. Eine Überschall-Gasdüse stellt das 3 mm-lange Beschleunigungsmedium mit Elektronendichten von $3 \times 10^{18}\,\mathrm{cm}^{-3}$ bis $5 \times 10^{18}\,\mathrm{cm}^{-3}$ bereit. Der eingesetzte Aufbau mit STII ermöglicht stabile Injektionsbedingungen, Ladungen bis 0.5 nC und Energiebreiten von ca. 40 MeV. Der aufgezeichnete Betatronradius belegt, dass die Strahlgröße am Ende der Beschleunigung etwa 1 µm beträgt. Optimales Beam-Loading ist bei einer Ladung von 250 pC bis 300 pC beobachtbar, während gleichzeitig ein Minimum für die Energiebreite und Strahldivergenz beobachtet werden. Das Divergenzminimum kann mit der hier gegebenen Hypothese zur transversalen Phasenraumdynamik mit Betatronoszillationen erklärt werden.

PUBLICATIONS BY THE AUTHOR

- **A. Köhler**, R. Pausch, J.P. Couperus Cabadağ, O. Zarini, J.M. Krämer, M. Bussmann, A. Debus, U. Schramm & A. Irman
  "Minimizing betatron coupling of energy spread and divergence in laser-wakefield accelerated electron beams."
  In: Physical Review Letters (submitted, 07.05.2019) [1]

- O. Zarini, J.P. Couperus Cabadağ, **A. Köhler**, T. Kurz, S. Schöbel, W. Seidel, M. Bussmann, U. Schramm, A. Irman & A. Debus
  "A Single-shot, ultra-broadband and highly sensitive spectrometer for short pulse, high resolution and low light diagnostic applications."
  (in preparation) [2]

- J. P. Schwinkendorf, S. Bohlen, J. P. Couperus Cabadağ, H. Ding, A. Irman, S. Karsch, **A. Köhler**, J. M. Krämer, T. Kurz, S. Kuschel, J. Osterhoff, L. F. Schaper, D. Schinkel, U. Schramm, O. Zarini & R. D'Arcy
  "Charge calibration of DRZ scintillation phosphor screens."
  In: Journal of Instrumentation (accepted) [3]

- A. Lumpkin, M. LaBerge, D. Rule, R. Zgadzaj, A. Hannasch, M. Downer, O. Zarini, B. Bowers, A. Irman, J. Couperus, A. Debus, **A. Köhler** & U. Schramm
  "Observations of Coherent Optical Transition Radiation Interference Fringes Generated by Laser Plasma Accelerator Electron Beamlets."
  In: IEEE conf. proc. of 18th AAC, (2018). DOI: 10.1109/AAC.2018.8659381 [4]

- O. Zarini, **A. Köhler**, J. Couperus, R. Pausch, T. Kurz, S. Schöbel, H. Meißner, M. Bussmann, U. Schramm, A. Irman & A. Debus
  "Advanced Methods For Temporal Reconstruction Of Modulated Electron Bunches."
  In: IEEE conf. proc. of 18th AAC, (2018).
  DOI: 10.1109/AAC.2018.8659388 [5]

- A. Irman, J.P. Couperus, A. Debus, **A. Köhler**, J.M. Krämer, R. Pausch, O. Zarini & U. Schramm.
  "Improved performance of laser wakefield acceleration by tailored self-truncated ionization injection."
  In: Plasma Physics and Controlled Fusion, 60(4), 044015 (2018).
  DOI: 10.1088/1361-6587/aaaef1 [6]

- J.M. Krämer, A. Jochmann, M. Budde, M. Bussmann, J.P. Couperus, T.E. Cowan, A. Debus, **A. Köhler**, M. Kuntzsch, A. Laso Garcia, U. Lehnert, P. Michel, R. Pausch, O. Zarini, U. Schramm & A. Irman.
  "Making spectral shape measurements in inverse Compton scattering a tool for advanced diagnostic applications."
  In: Scientific Reports, 8(1), 1398 (2018).
  DOI: 10.1038/s41598-018-19546-0 [7]

- T. Kurz, J.P. Couperus, J.M. Krämer, H. Ding, S. Kuschel, **A. Köhler**, O. Zarini, D. Hollatz, D. Schinkel, R. D'Arcy, J.P. Schwinkendorf, A. Irman, U. Schramm & S. Karsch.
  "Calibration and cross-laboratory implementation of scintillating screens for electron bunch charge determination."
  In: Review of Scientific Instruments, 89(9), 093303 (2018).
  DOI: 10.1063/1.5041755 [8]

- J.P. Couperus, R. Pausch, **A. Köhler**, O. Zarini, J.M. Krämer, M. Garten, A. Huebl, R. Gebhardt, U. Helbig, S. Bock, K. Zeil, A. Debus, M. Bussmann, U. Schramm & A. Irman.
  "Demonstration of a beam loaded nanocoulomb-class laser wakefield accelerator."
  In: Nature Communications, 8(1), 487 (2017).
  DOI: 10.1038/s41467-017-00592-7 [9]

- T. Heinemann, B. Hidding, R.W. Assmann, A. Martinez de la Ossa, A. Knetsch, O. Kononenko, J.P. Couperus, A. Irman, **A. Köhler**, T. Kurz, U. Schramm & O. Zarini.
  "Investigating the Key Parameters of a Staged Laser- and Particle Driven Plasma Wakefield Accelerator Experiment."
  In: Proceedings of International Particle Accelerator Conference (IPAC17), TUPIK010, 1703-1706 (2017) [10]

- U. Schramm, M. Bussmann, A. Irman, M. Siebold, K. Zeil, D. Albach, C. Bernert, S. Bock, F. Brack, J. Branco, J.P. Couperus, T.E. Cowan, A. Debus, C. Eisenmann, M. Garten, R. Gebhardt, S. Grams, U. Helbig, A. Huebl, T. Kluge, **A. Köhler**, J.M. Krämer, S. Kraft, F. Kroll, M. Kuntzsch, U. Lehnert, M. Loeser, J. Metzkes, P. Michel, L. Obst, R. Pausch, M. Rehwald, R. Sauerbrey, H.P. Schlenvoigt, K. Steiniger & O. Zarini.
  "First Results with the Novel Peta-Watt Laser Acceleration Facility in Dresden."
  In: Journal of Physics: Conference Series, 874, 12028 (2017).
  DOI: 10.18429/JACoW-IPAC2017-MOZB1 [11]

- J.P. Couperus, **A. Köhler**, T.A.W. Wolterink, A. Jochmann, O. Zarini, H.M.J. Bastiaens, K.J. Boller, A. Irman & U. Schramm.
  "Tomographic characterisation of gas-jet targets for laser wakefield acceleration."
  In: Nuclear Instruments and Methods in Physics Research, Section A: Accelerators, Spectrometers, Detectors and Associated Equipment, 830, 504–509 (2015).
  DOI: 10.1016/j.nima.2016.02.099 [12]

- A. Köhler, J.P. Couperus, O. Zarini, A. Jochmann, A. Irman, & U. Schramm.
  "Single-shot betatron source size measurement from a laser-wakefield accelerator."
  In: Nuclear Instruments and Methods in Physics Research Section A: Accelerators, Spectrometers, Detectors and Associated Equipment, 829, 265–269 (2016).
  DOI: 10.1016/j.nima.2016.02.031 [13]

- J.M. Krämer, J.P. Couperus, A. Irman, A. Köhler, M. Kuntzsch, U. Lehnert, P. Michel, U. Schramm & O. Zarini.
  "Bunch Arrival-Time Monitoring for Laser Particle Accelerators and Thomson Scattering X-Ray Sources."
  In: Proceedings of the 5th International Beam Instrumentation Conference (IBIC2016), TUPG53, 468-470 (2016)
  DOI: 10.18429/JACoW-IBIC2016-TUPG53 [14]

- R.G. Pausch, H. Burau, M. Bussmann, J.P. Couperus, A.D. Debus, A. Huebl, A. Irman, A. Köhler, U. Schramm, K. Steiniger & R. Widera.
  "Computing Angularly-resolved Far Field Emission Spectra in Particle-in-cell Codes using GPUs"
  In: IPAC 2014: Proceedings of the 5th International Particle Accelerator Conference, 761-764 (2014).
  DOI: 10.18429/JACoW-IPAC2014-MOPRI069 [15]

- A. Köhler
  "Charakterisierung von Plasmatargets für Laser-Wakefield Experimente."
  Diplomarbeit, Technische Universität Dresden, (2013) [16]

NOTE

Some of the work presented in this thesis has been previously published in above-mentioned publications. As such, some overlap exists.

CONTENTS

1. INTRODUCTION

Since the invention of particle accelerators in the 1930s, highly relativistic particles have enabled both outstanding discoveries and applications in modern science, impacting various fields such as industry and medical health care. Today, rapid technical improvements lead to ever more increased particle energies and a widespread deployment of more than ten thousand accelerators worldwide. A prominent example is the Large Hadron Collider (LHC) at CERN, Geneva. It is the world's most powerful microscope, which aims to resolve the internal structure of particles like the proton and neutron. With this machine, fundamental particles have been discovered, such as the Higgs boson which grants mass to all particles.

However, the LHC illustrates one fundamental problem of conventional accelerators: the large spatial dimensions necessary to obtain high energies. At 27 km in diameter it becomes the largest accelerator on earth. The reason for the size is the acceleration process. Typically, charged particles are accelerated by passing a high electric field gradient in conventional metal cavities. The maximum field strength of these cavities scales up to about 100 MV/m [17]. Electric fields above this limit are exposed to the vacuum breakdown where electrons from the surface are locally pulled into vacuum. The result is a collapse of the accelerating field. Therefore, an increase in particle energy requires an extension of the cavity and eventually more space. In circular accelerators, particles are guided many times through the same acceleration cavities in order to multiply the energy gain. In this case, the minimum diameter of the orbit is limited by energy loss due to synchrotron radiation.

A novel acceleration technique is urgently needed to overcome the fundamental vacuum breakdown limit and to make the next generation of accelerators smaller. That would shift the possible accessibility from a limited number of large-scale facilities to universities and research institutes. Additionally, easy to deploy table-top systems could become possible.

1.1. PLASMA-BASED ACCELERATION AND DIAGNOSTIC

The fundamental limit of the vacuum breakdown can be avoided by utilizing a medium that is already ionized, i.e., plasma. Acceleration based on plasma is a relatively young

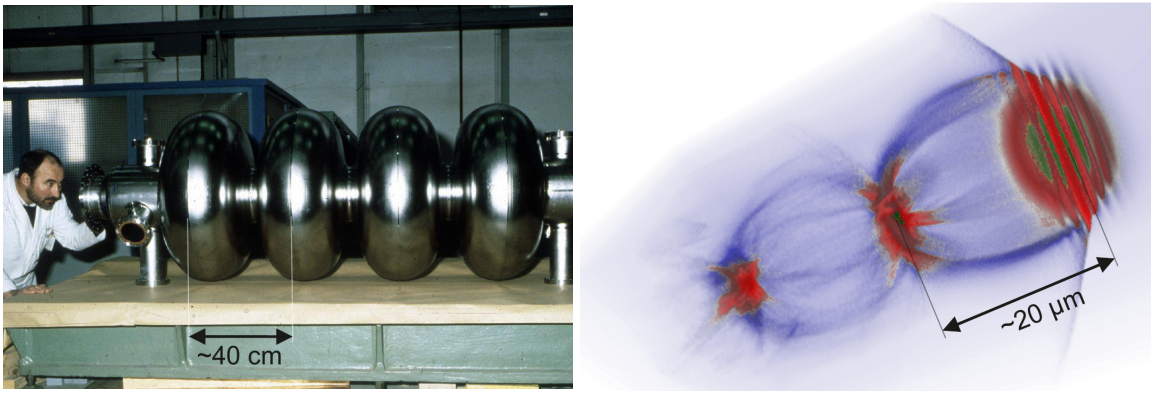

(a) Radio-frequency based cavity

(b) Plasma cavity (PIConGPU rendered)

Figure 1.1.: **Conventional and laser wakefield accelerator:** (a) shows a radio-frequency (RF) based cavity used in many conventional accelerators (Image: CERN). The cavity size is macroscopic (order of decimeters) and the used field gradients below 100 MV/m. (b) shows a plasma cavity driven by a laser pulse. The laser with the cavity are traveling with the speed of light from left to right. The dimensions of the plasma cavity are microscopic (∼10 µm). Accelerating gradients of over 100 GV/m are supported.

field with heavily ongoing research. In 1979, Tajima and Dawson [18] introduced it by proposing to use the electric fields originating from the collective oscillation of plasma electrons for acceleration of electron bunches. The plasma oscillations depend on the plasma density and can be driven by either high charge particle beams or high intensity laser pulses.

The case with a laser driver is known as laser-wakefield acceleration (LWFA). The high intensity of the laser pulse pushes electrons out of its path and thereby creates unshielded ions directly behind the driver. The Coulomb force induced by the charge separation pulls electrons back to the path of the laser. Electrons that are accelerated back to the laser axis gain energy and overshoot the equilibrium position. These collective plasma oscillations form a wakefield copropagating with the driver. Injected electrons experience a strong accelerating field and can gain highly relativistic energies.

In the late 1980s, the advent of short-pulse high power lasers triggered the first experiments with LWFA reaching ∼10 MeV electron energies [19]. One decade later, three groups simultaneously published papers in a Nature issue [20–22] and reported on the first experiments to generate quasi-monoenergetic bunches at several hundreds MeV. Nowadays, about 4 GeV of electron energies have been reached [23, 24]. Altogether, LWFA has demonstrated high energy beams with small energy spread, presenting the possibility for a good alternative for conventional accelerators.

Figure 1.1 compares the typical dimension in size for both conventional and laser plasma accelerators (LPA). Conventional accelerators have macroscopic cavities with a size ∼40 cm while plasma accelerators have plasma cavities with a typical size of 10 µm. That is roughly four orders of magnitude smaller and the sustainable field strength is roughly up to four orders of magnitude larger.

The small LPA dimensions challenge the diagnostic instrumentation for beam par-

ameters [25]. Typical wakefield accelerated electrons have beam sizes of ∼1 µm and are surrounded by hot plasma during the acceleration process. Behind the plasma exit, the beam length and transverse size can be measured via the transition radiation (TR) emitted by the electrons while passing through a dielectric foil. Note that the out-coupling of the plasma can have an impact on the transverse beam size and divergence [26] which needs to be taken into account.

An approach to measure the beam size directly at the plasma exit utilizes betatron radiation [27, 28]. In this case, effects from the out-coupling from the LPA into vacuum can be neglected and knowledge about the acceleration inside the plasma is gathered. Betatron radiation originates from oscillating motion of accelerated electrons inside the plasma and strongly correlates with the electron dynamics [29]. Thus, detection of the spectral shape of betatron radiation provides a powerful diagnostic of the betatron radius. The betatron radius is the maximum oscillation amplitude for electrons in LWFA at the end of the acceleration process. The bunch radius can be deduced from the betatron radius. Additionally, the betatron radiation can be utilized to directly image the electron trajectories of laser wakefields [30, 31]. The angular profile of the radiation can reveal the electron orbits and can indicate preferred planes of betatron oscillations [32, 33].

1.2. BETATRON RADIATION AS A HIGH FLUX X-RAY SOURCE

Many discoveries in medicine, chemistry, biology and physics have been made possible by x-ray radiation since their discovery by Roentgen [34]. X-rays can easily penetrate material and biological tissue and allow an insight into internal processes which can be, if at all possible, only accessed by disintegration. As an example, the high-resolution structure of photosynthetic core proteins has been elucidated using x-ray spectroscopy analysis [35].

LWFA accelerated beams can potentially be used as a driver for the next-generation of compact light sources [36–39]. One very direct way is to use the radiation that is created by the accelerator itself when the electrons undergo transverse oscillations due to the focusing forces inside the plasma. The so-called betatron radiation originating from these oscillations is emitted in the x-ray range with its temporal characteristics given by the transient accelerating time of electrons, i.e., a typically femtosecond time scale. Betatron radiation is collimated within a small emission cone, typically tens of milli-radians. The broadband, synchrotron-like nature of the betatron spectrum covers a large energy range at a continuous high flux. Additional to the collimation and the high flux, the intrinsic femtosecond duration of betatron radiation can provide a high temporal resolution.

The early x-ray sources such as x-ray tubes could image steady state processes. In 1960, the first pulsed x-rays became available by synchrotron facilities. Only a few decades ago, the first ultra-fast x-ray sources became accessible when Murnane et al. [40] demonstrated that a short laser pulse focused on a solid target can create x-ray flashes. These so-called $K\alpha$ sources have two major drawbacks for common experiments: Firstly, the emission angle is highly divergent with almost 4π. This requires the object to be placed within a short distance to the source and thus in-

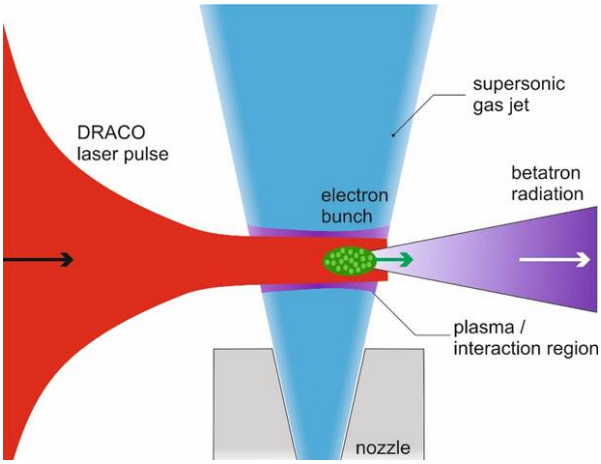

Figure 1.2.: **A simple schematic for LWFA and betatron radiation:** An intense laser pulse is focused onto a gas jet and drives a plasma wave inside a plasma channel. The focusing forces of the plasma channel cause betatron oscillations and the oscillating electrons emit synchrotron radiation.

creasing the background noise. Secondly, the emission line is small and dominated by the $K\alpha$ lines of the elemental composition of the target. A homogeneous spectral illumination over a broad range of energies is extremely challenging [41].

In contrast to $K\alpha$ sources, betatron radiation is also fast but additionally collimated and broadband in energy. When it is applied to backlit objects, spatial restrictions in a setup can be relaxed, i.e., the distance target-object. Applications such as the analysis of the absorption contrast around the K- and L-edges can probe a wide energy range at the same time and with the same source. A second typically applied method such as phase contrast imaging benefits from the high photon flux and the microscopic source size [42].

When a high temporal resolution is the main criteria for an experiment, betatron sources can be a better alternative than free-electron lasers (FELs). For example, the European XFEL provides x-ray pulses with a duration of less than 100 fs for wavelengths from 0.05 nm to 4.7 nm but is 3 km long and limited in the number of users. The biggest size factor for betatron radiation is the setup of the driver, e.g., the high power laser system. In the case of the betatron experiments in this thesis, the laser system fitted in a single room.

1.3. ABOUT THIS WORK

This thesis presents the continuing efforts to diagnose important transverse beam parameters for LWFA bunches with high charges at the Helmholtz-Zentrum Dresden–Rossendorf. The typical deployed setup for LWFA is presented schematically in figure 1.2. Here, a laser pulse is focused on a gas jet, that generates LWFA electrons and betatron radiation.

A new electron injection scheme [6] is utilized to reliably inject high charges into the wakefield while truncating the injection and thus limiting the spread in electron

energy. At the same time, the possible injection of high charges offers an operation in the beam loaded regime with a minimized energy spread under optimal beam loading conditions [43]. This enables systematic studies of different injected charges. Instead of studying the influence of beam loading on the energy spread [9], this work concentrates on the effects of high charge bunches on the transverse beam dynamic.

The beam divergence recorded in the dispersive plane of an electron spectrometer is studied for different charges and plasma densities. With the minimum normalized beam divergence found at optimal beam loading conditions, it is demonstrated that the minimized energy spread leads to an incomplete decoherence in the transverse phase space. In order to exclude space charge effects, the characteristics of betatron radiation are studied with Fresnel diffraction and with betatron spectroscopy. Betatron radii of $\sim$1 µm are measured and space charge effects on the betatron radiation are not detected. In conclusion, the optimal beam loading condition can minimize the beam divergence. The result can open a new path for beam optimization in high charge laser wakefield accelerators.

The structure of the thesis consists of chapters with theoretical fundamentals, diagnostics & analysis methods and experimental results. Chapter 2 discusses the basics of plasma and short pulse laser interactions and provides a first insight into a laser plasma accelerator. The transverse dynamics of accelerated electrons, including the emitted radiation spectrum are covered by chapter 3. Chapter 4 presents the infrastructure used for the experiments. The short-pulse high-intensity laser system DRACO, the experimental target area with the LWFA setup and the betatron diagnostics are explained in detail. The method for the careful analysis of the recorded betatron radiation is explained in chapter 5. The acquired data is presented and a hypothesis for the observed effects is discussed in chapter 6. Eventually, a conclusion of the thesis and an outlook for further possibilities of applying the results are given in chapter 7.

2. THEORY OF PLASMA-BASED ACCELERATION

This chapter highlights essential concepts in laser-wakefield acceleration, which creates the basic knowledge for the performed experiments. The aim is to provide a starting point for the reader to continue with the theoretical considerations about betatron radiation and beam dynamics in chapter 3. The theoretical basis eases the understanding of the experiments presented in chapter 5 and 6.

In LWFA, a high intensity laser pulse propagates through a transparent medium, i.e., gas or plasma. In the case of neutral gas, the rising edge of the laser pulse ionizes the gas. Thus, the main laser pulse propagates through an underdense plasma. The ponderomotive force associated with the intensity gradient of the pulse expels plasma electrons from the laser axis. These electrons experience a strong Coulomb force due to the charge separation set up by the almost immobile ions and are pulled back to their initial position. The exerted force leads to oscillations of the expelled electrons at the plasma frequency ω_P:

$$\omega_\mathrm{P} = \sqrt{\frac{n_\mathrm{e} e^2}{m_\mathrm{e} \varepsilon_0}}, \tag{2.1}$$

where n_e is the plasma density, e is the elementary charge of the electron, m_e is the electron's mass and ε_0 is the vacuum permittivity. The plasma oscillations create a plasma wave, the so-called wake, with a phase velocity close to the speed of the laser pulse. Electrons injected at the correct phase can gain energy from the fields inside the wake.

Ionization, the fundamental process of creating a plasma from neutral atoms is briefly discussed in section 2.1. Then, in section 2.2, the ponderomotive force is described, which is the fundamental net-force by the driver laser pulse that enables plasma cavities to be formed. The guiding of high intensity laser pulses in plasmas is described in section 2.3. Section 2.4 describes a model for LWFA in one and three dimensions. Injection of electrons is discussed in section 2.5. Section 2.6 describes beam loading which occurs for injected high charges. The chapter closes with a description of the electromagnetic fields inside a plasma accelerator in section 2.7.

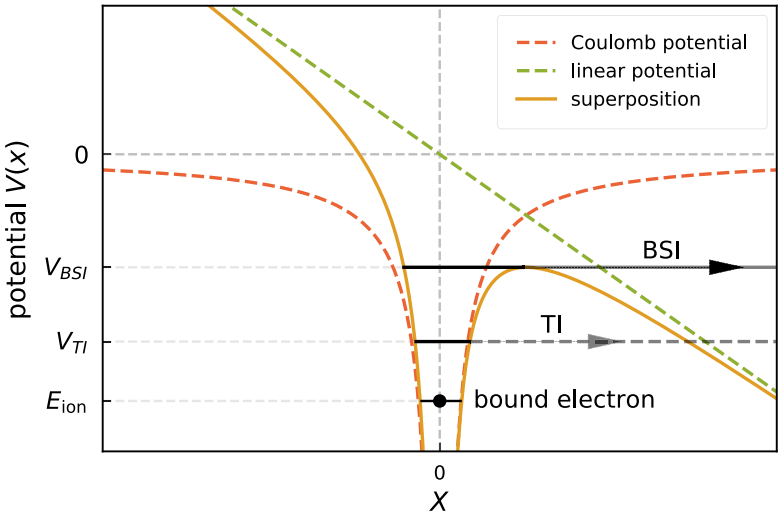

Figure 2.1.: **Barrier-Suppression and tunnel ionization:** The strong electric field of the laser pulse deforms the Coulomb potential of an atom. The complete suppression of the electric field of the atom instantly frees a bound electron with potential energy $V > V_{\mathrm{BSI}}$. An electron with a lower potential energy $V_{\mathrm{TI}} < V_{\mathrm{BSI}}$ has a nonzero probability to tunnel through the potential barrier and to leave the atom orbit.

2.1. IONIZATION OF GAS

The essential process of plasma creation is ionization where bound electrons are detached from an atom. As illustrated in figure 2.1, ionization by photons requires the bound electron to absorb energy from photons in order to escape the Coulomb potential of the atomic core. For photon energies higher than the ionization energy, an excited electron gains sufficient energy to overcome the Coulomb barrier and becomes free. This type of ionization is more relevant for photons with high energies and short wavelengths, i.e., x-ray radiation, and will be discussed in the description of the x-ray spectroscopy setup in section 4.4.

The typical electric field gradient of a bound electron of a hydrogen atom is on the order of 5 GV/m [45]. When the electric field of a laser pulse reaches that order of magnitude, it will deform the potential of the bound electrons. The effective potential is given by a superposition of the Coulomb potential of the core with Z positively charged protons and the electric field E of the laser pulse:

$$V_{eff} = -\frac{Ze^2}{|x|} - eEx, \tag{2.2}$$

where x denotes the absolute distance to the center of the core.

Two scenarios can be possible. In barrier-suppression ionization (BSI), electrons with an energy higher than the barrier V_{BSI} will spontaneously escape and will be set free. However, electrons below the barrier possess a finite probability to escape the atom. In tunnel ionization (TI), they can tunnel through the barrier with a non-zero

Table 2.1.: **Different ionization energies of typical gases for LWFA:** Values for E_{ion} are from [44]. The threshold intensity for BSI I_{BSI} is calculated with equation (2.3) and normalized laser intensity a_0 is calculated with equation (2.11).

Generated ion	E_{ion} [eV]	I_{BSI} [W/cm^2]	a_0 at 800 nm
H^+	13.7	1.4×10^{14}	8.2×10^{-3}
He^+	24.6	1.5×10^{15}	2.6×10^{-2}
He^{++}	54.4	8.8×10^{15}	6.4×10^{-2}
N^+	14.5	1.8×10^{14}	9.1×10^{-3}
N^{++}	29.6	7.7×10^{14}	1.9×10^{-2}
N^{3+}	47.4	2.2×10^{15}	3.3×10^{-2}
N^{4+}	77.5	9.0×10^{15}	6.5×10^{-2}
N^{5+}	97.9	1.5×10^{16}	8.3×10^{-2}
N^{6+}	552.1	1.0×10^{19}	2.2
N^{7+}	667.0	1.6×10^{19}	2.8

probability.

BSI requires a laser intensity to be larger than the threshold I_{BSI} [45]:

$$I_{BSI}[\mathrm{Wcm^{-2}}] = 4 \times 10^9 \frac{E_{ion}^4[\mathrm{eV}]}{Z^2}, \tag{2.3}$$

where E_{ion} is the ionization energy. Table 2.1 denotes typical values for E_{ion} and I_{BSI}. Typically, low Z-gases such as hydrogen (H_2) and helium (He) are already fully ionized by the rising edge of a high power laser pulse. It holds for the outer shell electrons of gases with larger Z, such as nitrogen (N_2). However, the situation can be different for the K-shell. The electrons are much more strongly bound to the core resulting in a larger ionization threshold. This fact is used in special injection schemes to overcome trapping limits as discussed in section 2.5.

2.2. PONDEROMOTIVE FORCE

An electron in a laser pulse experiences the electric field component of the laser. Thus, it follows the equation of motion:

$$\frac{\mathrm{d}\vec{p}}{\mathrm{d}t} = -e\vec{E}, \tag{2.4}$$

where $\vec{p}$ is the electron's momentum and $\vec{E}$ the electric field component of the laser pulse. Its absolute value E oscillates with the laser frequency ω_0:

$$|\vec{E}| = E(t) = E_\mathrm{m} \exp\left(-\frac{r^2}{w^2}\right) \sin\omega_0 t, \tag{2.5}$$

where E_m denotes the maximum field strength and the Gaussian term describes the beam envelope with beam radius w. On short time scales on the order of ω_0^{-1}, the

electron oscillates with the same frequency as the laser pulse. This motion is called the quiver motion and is linked with the quiver momentum:

$$\vec{p} \approx \frac{e}{c}\vec{A}, \tag{2.6}$$

where $\vec{A}$ is the vector potential of the electromagnetic wave and c is the speed of light in vacuum. For time scales larger than ω_0^{-1}, the longitudinal pulse shape is important for the macroscopic motion of the electron. Averaging provides the net force acting on one electron [45], called ponderomotive force:

$$\vec{F}_p = \langle \frac{\mathrm{d}\vec{p}}{\mathrm{d}t} \rangle = -\frac{e^2}{4m_\mathrm{e}\omega_0^2} \nabla(\vec{E}^2). \tag{2.7}$$

For a Gaussian laser pulse, electrons follow the gradient of the pulse envelope E^2 which is directly proportional to the intensity I, i.e., electrons are ejected from the peak intensity toward lower intensities. The ponderomotive energy U_p is the potential of $\vec{F}_p$ and is given by [46]:

$$U_p = \frac{e^2 E^2}{4m_\mathrm{e}\omega_0^2} \tag{2.8}$$

or in practical units

$$U_p[\mathrm{eV}] = 9.337 \times 10^{-14} I[\mathrm{W/cm^2}] \lambda_0^2[\mu\mathrm{m}], \tag{2.9}$$

where I denotes the laser peak intensity and λ_0 is the central laser wavelength.

Moreover, when an electron gains relativistic energies during one oscillation period, it also becomes subject to the magnetic field component. In this case, equation (2.4) must be expanded to the complete Lorentz force:

$$\frac{\mathrm{d}\vec{p}}{\mathrm{d}t} = -e(\vec{E} + \vec{v} \times \vec{B}). \tag{2.10}$$

Here it becomes clear that the second term with the magnetic field $\vec{B} \propto \vec{E}/c$ can only be neglected for small electron velocities $v \ll c$.

However, the influence of the magnetic field on the electron motion becomes relevant for relativistic velocities $v \to c$. The normalized vector potential a_0 [47] can be used to estimate the strength of the interaction between the laser pulse and electron and when relativistic effects should be considered. It is given by $a_0 = \frac{eA}{m_\mathrm{e}c} = \frac{eE}{m_\mathrm{e}c\omega_0}$ or in more practical units:

$$a_0 = \sqrt{\frac{2e^2\lambda_0^2 I}{\pi m_\mathrm{e}^2 c^5}} \approx 0.86 \times 10^{-9} \lambda_0[\mu\mathrm{m}] \sqrt{I[\mathrm{W/cm^2}]}. \tag{2.11}$$

For $a_0 = 1$, the electron gains in one half-cycle roughly the same kinetic energy as its rest energy. This defines the threshold for relativistic effects and the magnetic component of the Lorentz force cannot be neglected anymore. For laser light with $\lambda_0 = 800\,\mathrm{nm}$, the associated threshold intensity is on the order of $2 \times 10^{18}\,\mathrm{W/cm^2}$.

One other important fact visible in equation (2.11) is that the intensity depends on the square of the particle's mass. Protons and ions with a mass about three orders of magnitude larger than the electron's mass require the intensity to be about six orders of magnitude higher to become relativistic. Therefore, the ion dynamic induced by the laser pulse takes place on a larger time scale than the electron motions. At thermal energies, ions can be assumed to be immobile during the laser-plasma interaction.

2.3. GUIDING OF RELATIVISTIC LASER PULSES

LWFA requires relativistic intensities to drive plasma waves. As will be shown in section 2.4, the blowout regime [48] requires a ponderomotive force strong enough to expel all electrons from the laser pulse axis. Typically, such high intensity laser pulses are obtained by focusing high power laser pulses to a tens of micrometer spot size. However, the distance along the beam axis with the focal intensities is limited by diffraction. The characteristic distance at which the beam significantly diffracts is called the Rayleigh length [49] and defines the distance before and after the focus where the intensity is half of the peak intensity at the focus:

$$z_\mathrm{R} = \pi \frac{w_0^2}{\lambda_0}, \tag{2.12}$$

where w_0 is the e^{-2} beam waist at the focus. The beam waist increases by a factor of $\sqrt{2}$ after one Rayleigh length. As an example, a laser pulse with a central wavelength of 800 nm and a focal spot size w_0 of 19 µm reduces to half of its intensity after propagating 1.4 mm. In contradiction, typical LWFA requires multiple millimeters to centimeters of interaction length to efficiently accelerate electrons to high energies.

One possibility to overcome the fast diffraction of the laser pulse and to contain high intensities over many Rayleigh lengths is to guide the laser pulse in a plasma channel with a proper density profile, e.g., discharge capillaries [16, 50]. As it will be pointed out in section 4.3, an electrical discharge forms a parabolic density profile suitable to guide laser pulses but has some disadvantages in the experimental setup. A simple approach albeit more complex process relies on the non-linear self-focusing effect [51]. Self-focusing occurs when the laser pulse locally changes the plasma density to a radial profile with a refractive index that can guide the laser pulse.

The index of refraction η of plasma can be written as [47, 52]:

$$\eta = \frac{ck_0}{\omega_0} \simeq 1 - \frac{1}{2}\frac{\omega_\mathrm{P}^2}{\omega_0^2}\left(1 + \underbrace{\frac{\Delta n_c}{n_\mathrm{e}}\frac{r^2}{w_0^2}}_{\text{external}} + \underbrace{\frac{\Delta n}{n_\mathrm{e}}}_{\text{ponderomotive}} - \underbrace{\frac{a_0^2}{8}}_{\text{relativistic}}\right), \tag{2.13}$$

where $k_0 = 2\pi/\lambda_0$ is the laser wavenumber. Equation (2.13) incorporates different possibilities of guiding laser pulses. The first term shows external guiding by a pre-formed plasma channel with Δn_c as the channel depth. The second term represents guiding caused by the ponderomotive force where Δn is the local change in density. The last term depicts relativistic self-guiding. In the strong field of a laser, electrons

are accelerated to velocities close to the speed of light c and they become heavier by the Lorentz factor γ. A self-guiding channel forms for $a_0^2/8 \gtrsim 4/(k_P\omega_0)$ [52]. The critical power required for relativistic self-focusing is given by [51]:

$$P_c[\mathrm{GW}] = 17 \left(\frac{\omega_0}{\omega_P} \right)^2 . \tag{2.14}$$

The self-guiding channel requires a distance of $\sim c/\omega_P$ for formation due to the electron's inertia [53]. Thus, the front of the laser pulse is not guided by the channel. However, local pump depletion occurs while transferring energy to the wake. The photons at the front are shifted toward longer wavelengths. Dispersion causes the photons to slip back in the frame of the laser pulse with the etching velocity, where the channel can guide them [53]. The etching velocity v_{etch} is given by [52]:

$$v_{etch} = \frac{\omega_P^2}{\omega_0^2} c. \tag{2.15}$$

The result is an enhanced a_0 at significantly reduced diffraction losses which leads to a stronger laser driver over many z_R. The etching also affects the speed of the wake driven by the laser pulse. Without pump depletion, the plasma wave travels with the linear group velocity of the laser pulse v_g, given by [54]:

$$v_g = c\sqrt{1 - \frac{\omega_P^2}{\omega_0^2}}. \tag{2.16}$$

Pump depletion reduces the phase velocity of the wake to $v_\phi = v_g - v_{etch}$, which leads to phase slippage as given below in section 2.4.2.

At the time the laser pulse power drops below the critical power required by equation (2.14), the self-focusing of the laser pulse ends. The laser pulse diverges and the plasma cavity diminishes. Thus, a laser pulse can propagate by self-focusing a distance given by [52]:

$$L_{pd} \simeq \frac{c}{v_{etch}} c\tau \simeq \left(\frac{\omega_0}{\omega_P} \right)^2 c\tau, \tag{2.17}$$

where τ and L_{pd} are the laser pulse duration at full-width half-maximum and the pump-depletion length, respectively. Experiments with LWFA should be typically designed such that L_{pd} is longer than the plasma in order to convert as much energy as possible to the wake.

2.4. LASER-WAKEFIELD ACCELERATION

As first proposed by Tajima and Dawson [18], the basic idea of laser-wakefield acceleration is to utilize oscillations of the plasma electrons to create a wake. The accelerating field in the wake then should be higher than electric fields sustainable by conventional accelerators.

2.4.1. LWFA IN ONE DIMENSION

The basic description of LWFA can be explored in a one-dimensional model as shown by figure 2.2. The model uses the quasi-static approximation [55], which neglects the evolution of the laser pulse and assumes that the laser envelope is only a function of the co-moving variable $\xi = z - v_\phi t$. Additionally, the phase velocity of the wake v_ϕ equals the laser group velocity v_g.

The normalized vector potential of a Gaussian shaped laser pulse propagating in z is given by:

$$\vec{a} = a(z,t)\cos(k_0 z - \omega_0 t)\vec{e}_r \quad \text{with} \quad a(z,t) = a(\xi) = a_0 \exp\left(-\frac{\xi^2}{L_0^2}\right), \tag{2.18}$$

where L_0 is the length of the laser pulse and a_0 is the normalized laser potential from equation (2.11).

The plasma wakefield can be described by the normalized potential Φ which is provided by the Poisson equation of the system. The potential can be found by solving [56]:

$$\frac{\mathrm{d}^2\Phi}{\mathrm{d}\xi^2} = k_\mathrm{P}^2\gamma_\phi^2\left(\beta_\phi\left[1 - \frac{\gamma_\perp^2}{\gamma_\phi^2(1+\Phi)^2}\right]^{-1/2} - 1\right), \tag{2.19}$$

where $\gamma_\perp^2 = 1 + a_0^2$ is the transverse energy of the electron in the laser field. The Lorentz factors of the wake are $\gamma_\phi = (1 - \beta_\phi^2)^{-1/2}$ and $\beta_\phi = v_\phi/c$. The electric fields of the oscillations are on the order of the so-called cold, non-relativistic wave-breaking limit. It can be expressed for a plasma with density n_e as [56]:

$$E_0 = \frac{m_\mathrm{e} c \omega_\mathrm{P}}{e} \quad \text{or} \quad E_0[\mathrm{GV/m}] \simeq 96\sqrt{n_\mathrm{e}[10^{18}\mathrm{cm}^{-3}]}. \tag{2.20}$$

Equation (2.19) is a differential equation which can be solved numerically. The accelerating field along z can be derived by [56]:

$$\frac{E_z}{E_0} = k_\mathrm{P}^{-1}\frac{\mathrm{d}\Phi}{\mathrm{d}\xi}. \tag{2.21}$$

Additionally, the perturbation of the plasma density n is given by [56]:

$$\frac{n(\xi)}{n_\mathrm{e}} = \gamma_\phi^2\beta_\phi\left[\left(1 - \frac{\gamma_\perp^2}{\gamma_\phi^2(1+\Phi)^2}\right)^{-1/2} - \beta_\phi\right], \tag{2.22}$$

where n_e is the unperturbed plasma density. The potential, the accelerating field and the plasma density of a one-dimensional wakefield can be calculated with equations (2.19), (2.21) and (2.22), as illustrated by figure 2.2. The figure presents the linear regime with $a_0 \ll 1$ and the nonlinear regime with $a_0 \gg 1$. In the linear regime, the plasma oscillations are small and Φ, E_z, and n have a sinusoidal shape, as shown in figure 2.2a. In the nonlinear regime shown figure 2.2b, almost all electrons can be expelled by the laser pulse. The expulsion leaves a region void of electrons after the

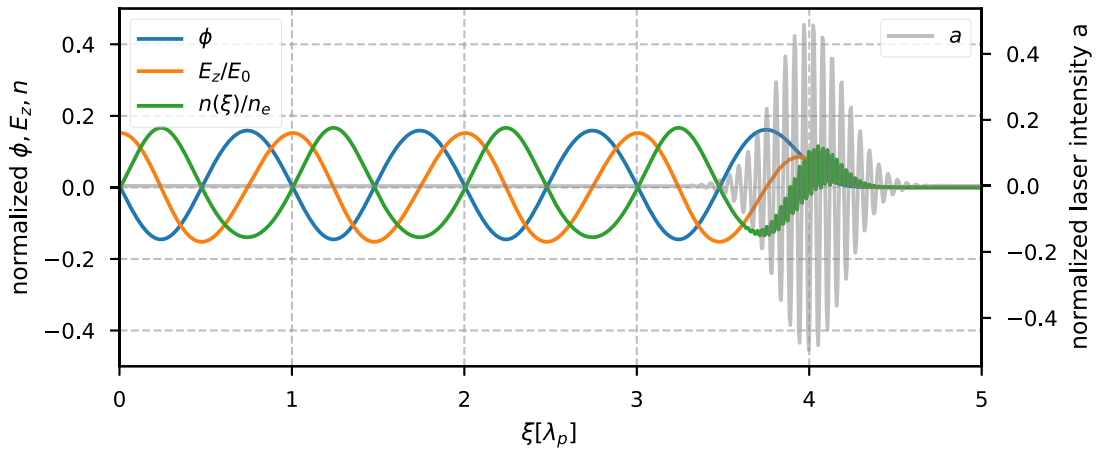

(a) Linear regime, $a_0 = 0.5$.

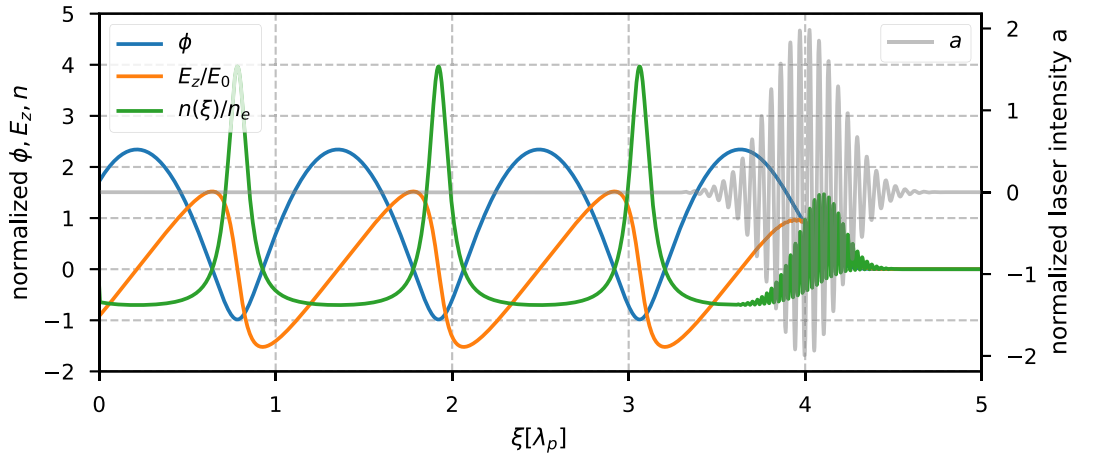

(b) Non-linear regime, $a_0 = 3$.

Figure 2.2.: **Linear and non-linear LWFA in one dimension:** The linear regime in (a) has a sinusoidal potential, density perturbation and accelerating field E_z. The non-linear regime in (b) shows a potential $\propto \xi^2$, a non-linear behavior in density and a linear acceleration field E_z within one plasma period. The laser pulse length is $c\tau = \lambda_P/5$.

laser pulse. Thereby, the electron density n can approach zero after the laser peak and can rise to a sharp peak at one plasma wavelength behind the laser pulse. The accelerating field E_z is almost linear within one plasma period.

2.4.2. LWFA IN THREE DIMENSIONS AND THE BUBBLE REGIME

Also in three dimensions, the response of the plasma to laser pulse depends on the strength of the interaction, i.e., a_0.[1] In this work, the driver is a laser pulse as studied by Pukhov and Meyer-ter-Vehn [48]. In the case of $a_0 > 2$ and a laser pulse length shorter than a plasma period, the ponderomotive force can expel all electrons in the laser path. The created electron-free structure is called a bubble or blowout [48].

Lu et al. [52] found by simulations stable spherically shaped plasma cavities with radius R_b when the laser spot size w_{laser} matches transversely with R_b such as $w_{\text{laser}} \simeq R_b$. The size of the bubble was found to depend on a_0 [52] such that the matching condition can be reformulated as:

$$w_{\text{laser}} \simeq R_b = 2\sqrt{a_0}/k_{\text{P}}. \tag{2.23}$$

As found by simulations, a spherical bubble requires at minimum an a_0 larger than four. However, for $2 < a_0 < 4$, a blowout can form a cavity that differs only a little from an absolute sphere [52].

The plasma oscillations move with the same velocity as the laser pulse in the plasma. When electrons are accelerated by the plasma fields shown in section 2.7, they will approach the speed of light and become faster than the laser pulse. At this point, they will move forward in the wake and suffer a phase slippage. Finally, they will enter the decelerating phase. The process is called dephasing and the traveled length of the electrons in the laboratory frame is the dephasing length [52]:

$$L_{\text{deph}} \simeq \frac{2\omega_0^2}{3\omega_{\text{P}}^2} R_b. \tag{2.24}$$

An LPA should operate with an interaction length close to L_{deph} in order to fully exploit the wakefield.

2.5. INJECTION OF ELECTRONS

Injection of electrons into the accelerating phase of a wake is of importance to generate high-quality electron bunches. One of the biggest challenges in plasma-based acceleration is to control the injection process. Beam parameters, such as bunch charge, energy spread and emittance, should be conserved until the end of the acceleration in an ideal plasma accelerator [58].

Conventional accelerators use electrons from separate sources, called injectors. Electron sources need to be precisely timed and synchronized with the phase of the accelerator cavities in order to maximize the energy gain and to avoid charge losses.

[1] The non-linear regime was originally studied with electron beam drivers by Rosenzweig et al. [57]. The advent of short-pulse high power laser systems triggered the utilization of laser pulses for driving a wake.

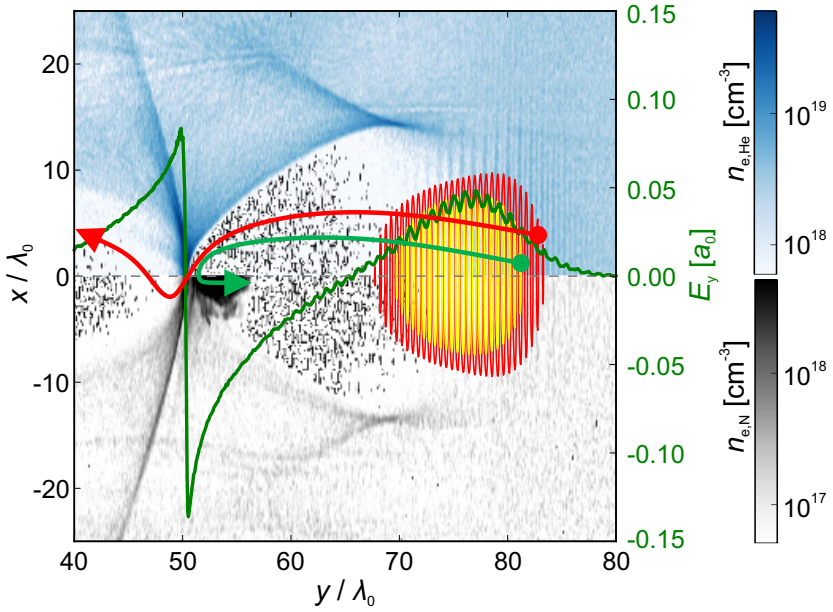

Figure 2.3.: **Ionization-induced injection in the bubble regime:** The laser pulse (red and yellow) is traveling from the left to the right. The red region indicates the region where the laser field strength is sufficient to generate N^{6+} and the yellow region shows where this is the case for N^{7+}. The electron density (blue scale) from helium electrons is shown in the top half of the figure. The density of ionized K-shell electrons (grayscale) is shown in the bottom half. The green line plot presents the longitudinal electric field. Two possible electron trajectories (green and red) originating at the rising edge of the laser are shown. The green trajectory shows a case with matched trapping condition [43] while the red trajectory illustrates the case when the trapping condition is not reached.
Image from Couperus [43].

For a plasma cavity, the temporal and spatial requirements become even more challenging because of the compactness of the accelerator. Typically, the bunch should be at relativistic energy and smaller than a plasma wavelength in all three dimensions [58]. Correct timing and positioning require sub-femtosecond and micrometer precision. Any mismatch can lead to an injection in the wrong phase and beam degradation.

The technical challenges can be avoided when electrons are injected from the background plasma instead from external sources. Internal sources in general introduce the disadvantage of a coupled injection and acceleration. Several mechanisms for internal electron injection have been used in the past [56]. In order to inject plasma electrons, the non-linearity of LWFA can be utilized by wave-breaking. Wave-breaking occurs when the maximum longitudinal velocity of plasma electrons exceeds the phase velocity of the wake v_ϕ. The maximum sustainable field before wave-breaking can take place is given by [59]:

$$E_{1D,max} = \sqrt{2(\gamma_\phi - 1)}E_0. \tag{2.25}$$

Self-injection occurs in three dimensions at least for $a_0 > 4.3$ [60]. Technically, this mechanism is simple to implement since no modifications on the setup or target are necessary. However, due to the high non-linear nature of the injection, the scheme has large shot-to-shot fluctuations. Furthermore, the direct coupling of injection and acceleration process makes it impossible to independently control the injection of electrons from the acceleration process.

The reliability of the injection dramatically increases by introducing a perturbation in the plasma density [61]. When the wake is traveling through a short ($\leq \lambda_P$) down-ramp in density, the plasma wavelength and hence the cavity radius increases, leading to a moment of reduction of the wake's phase velocity. As a result, electrons at the end of the bubble can be trapped because they are already faster than the wake's velocity [56]. Trapping of electrons means injection at the accelerating phase and subsequent acceleration of electrons.

Ionization injection [62–64] is a method utilizing the fact, that electrons in the K-shell require higher laser intensities for ionization, as shown in section 2.1 and table 2.1. Figure 2.3 illustrates the injection scheme. The K-shell electrons are freed and injected close to the peak intensity of the laser pulse located at the front part of the plasma cavity. They can be trapped at the end of the plasma cavity in the accelerating phase and can gain energy. The big advantage is the straightforward implementation that only requires the addition of a small fraction from a higher-Z gas, such as nitrogen, to the acceleration medium. The injection can continue until the end of the doped plasma region or until the laser intensity has dropped below the ionization threshold. The result is a continuous injection along a macroscopic distance and thus a typically huge energy spread.

In 2014, **S**elf-**T**runcated **I**onization **I**njection (STII) was first proposed by Zeng et al. [65] and demonstrated one year later by Mirzaie et al. [66]. STII aims to fix the large energy spread of ionization injection by utilizing a laser pulse that does not match equation (2.23). The carefully chosen mismatch between the laser spot size and the plasma cavity can lead to a temporal evolution of the laser pulse and wakefield. The varying peak intensity of the laser and variations in the trapping conditions then cause truncation of the injection [6, 43].

2.6. BEAM LOADING

The plasma cavity in the nonlinear regime as shown in section 2.4.2 has a linear acceleration gradient typically. The acceleration gradient causes electrons in the front of the bunch to gain energy at a lower rate than electrons in the tail. This introduces a large energy spread to the accelerated electrons and can limit the possibilities for further application of the bunch. However, the self-field of the bunch can superimpose the accelerating field. For a large number of injected electrons, the accelerating field can flatten due to this superposition. In this case, LWFA operates in the beam loading regime. The impact of beam loading on the laser-wakefield accelerator was investigated by Jurjen Couperus [43] in detail. This topic is reviewed here for a complete description of the physics.

In general, the impact of the injected charge on the wakefield and the resulting su-

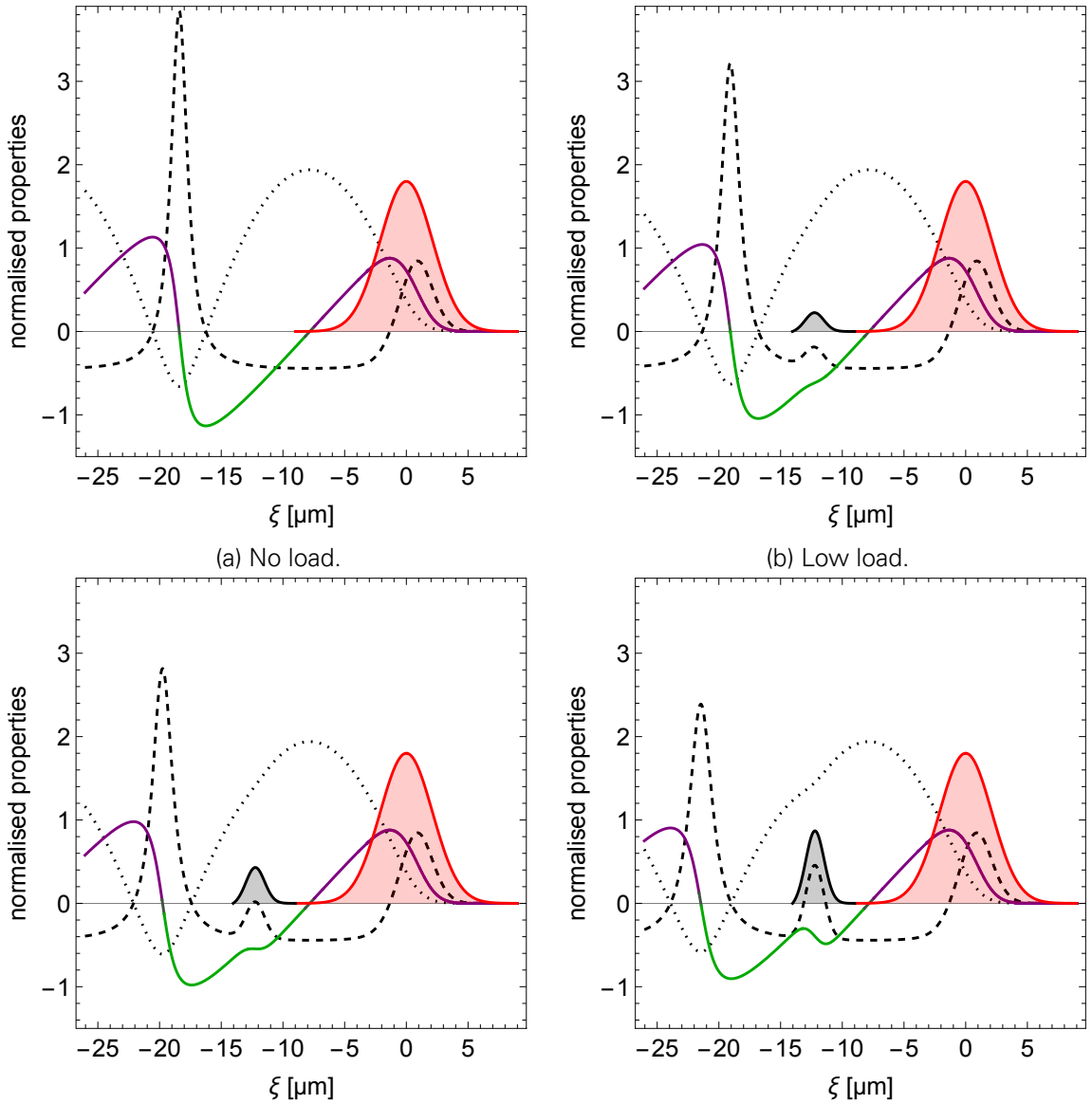

(a) No load.

(b) Low load.

(c) Medium (optimal) load.

(d) Strong load.

Figure 2.4.: **The effect of beam loading in one dimension:** The laser pulse (red, $a_0 = 1.8$, $\tau_{\text{laser}} = 10\,\text{fs}$) drives the wakefield at a plasma with $n_e = 3.7 \times 10^{18}\,\text{cm}^{-3}$. The dashed and dotted black lines represent the plasma density and the pseudo-potential of the accelerating field, respectively. In the unloaded case (a), the accelerating field (solid purple/green line) is linear within the wake. Different bunch loads (black) are introduced into the wakefield in (b)-(d). The small load in (b) leads to small deformations of the accelerating field. When the load is increased to an optimum value as in (c), then the field is the same along the bunch, while a huge load in (d) causes the field to twist completely.
Figures from Couperus [43].

perposition can be divided into different cases depending on the amount of injected charge as represented by figure 2.4: Without load, the accelerating field is linear, as shown in figure 2.4a. In the case of a low injected charge shown in figure 2.4b, the injected charge is small and the shape of the cavity field does not change significantly. Electrons in the front of the bunch experience a smaller field than in the back. Thus they gain less energy over the same acceleration distance than electrons at the back which introduces a large energy spread. The case of optimal loading is shown in figure 2.4c. The injected charge flattens the accelerating field gradient and thus the bunch can experience the same field along ξ. Consequently, the flatter gradient reduces the energy spread. An even higher charge can lead to a substantial deformation of the wake, as shown in figure 2.4d.

BEAM LOADING IN ONE DIMENSION

In 1987, Katsouleas et al. [67] developed the first one-dimensional theory for beam loading in laser-wakefield accelerators. He found the upper limit N_{max} for the number of electrons that are possible to be accelerated by a linear wakefield. The maximum number of electrons is given by [67]:

$$N_{\mathrm{max}} \approx \frac{n_1}{k_{\mathrm{P}}} A \approx 5 \times 10^5 \left(\frac{n_1}{n_0} \right) \sqrt{n_0[\mathrm{cm}^{-3}]} A[\mathrm{cm}^2], \tag{2.26}$$

where k_{P} is the wavenumber of the unperturbed plasma, n_0 is the plasma density, n_1 is the perturbed plasma density associated with the wave and A is the cross section of the wake. As an example, a wave with a radius of 30 µm in a plasma density of $5 \times 10^{18}\,\mathrm{cm}^{-3}$ and $n_1 = 0.2 n_0$ can accelerate $\sim 6 \times 10^9$ electrons or 1 nC of charge.

N_{max} defines 100 % efficiency of the accelerator by transferring all energy from the wake to the bunch. However, this is reached by introducing 100 % energy spread to the accelerated electrons [67]. Electrons in the front of the bunch experience the unperturbed electric field of the wake. While at the same time, the tail of the bunch is exposed to a reduced accelerating field caused by the overlapping of the wake and bunch fields. The reduction is linear to the number of electrons N in the loaded beam. The accelerating field experienced by the last electron vanishes in the extreme of $N = N_{\mathrm{max}}$. The relative energy spread is given by [67]:

$$\frac{\Delta\gamma_{\mathrm{max}} - \Delta\gamma_{\mathrm{min}}}{\Delta\gamma_{\mathrm{max}}} = \frac{E_f - E_b}{E_f} = \frac{N}{N_{\mathrm{max}}}, \tag{2.27}$$

where $E_{f,b}$ refer to the field at the front and back of the bunch and $\Delta\gamma_{\mathrm{max,min}}$ are the maximum and minimum energy gain of a bunch particle. Equation (2.27) indicates the crucial relation that an increase in injected charge leads to an increase in energy spread.

In 1985, S. van der Meer [68] suggested a specialized bunch shape with a finite length in order to avoid the disadvantage of beam loading exposed by equation (2.27). A triangularly shaped bunch with the peak density at the bunch's head and the density vanishing at the tail can reduce the gained energy spread. At the same time, the number of electrons can be kept large. An optimally shaped bunch would cause the

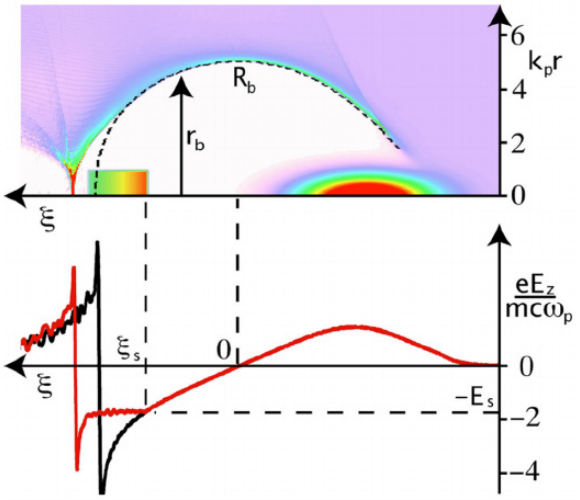

Figure 2.5.: **Beam loading in three dimensions:** The top plot illustrates the electron density from a PIC simulation with a bubble radius $k_P R_b = 5$. The driver (right) and the electron bunch (left) move to the right. The black dashed line indicates the bubble radius without load. The bottom plot shows the accelerating field along the longitudinal axis ($r = 0$) without load (black line) and with load (red line). Figure from Tzoufras et al. [69].

same accelerating field along the bunch axis due to a superposition of bunch self-fields and wakefield.

BEAM LOADING IN THREE-DIMENSIONAL, NON-LINEAR WAKES

The one-dimensional description of beam loading gives the first insight into the changes of the electron dynamics. Expanding this to an analytic description of beam loading in the non-linear and three-dimensional case is more challenging. Lu et al. [52] provided an estimate for the maximum number of electrons N inside a plasma cavity [52]:

$$N \simeq \frac{8/15}{k_0 r_e}\sqrt{\frac{P}{m_e c^3/r_e}} \simeq 2.5\times 10^8 \times \frac{\lambda_0[\mu\mathrm{m}]}{0.8}\times\sqrt{P[\mathrm{TW}]}, \tag{2.28}$$

where $r_e = e^2/(m_e c^2) \approx 2.82\,\mathrm{fm}$ is the classical electron radius. As an example, a laser pulse with $\lambda_0 = 800\,\mathrm{nm}$ and $P = 100\,\mathrm{TW}$ can drive a wake with a maximum load of 400 pC of charge.

Tzoufras et al. [69, 70] extended the non-linear, three-dimensional model from Lu et al. [52] to investigate optimal beam loading as illustrated in figure 2.5. Comparable with the one-dimensional theory, a trapezoidal bunch shape was found, that flattens the accelerating field to a value E_s along the bunch. The field E_s can conserve the energy spread of the bunch. The charge Q_s required for E_s scales as [69]:

$$Q_s[\mathrm{nC}]\frac{E_s}{E_0} \approx 0.047\sqrt{\frac{10^{16}}{n_e[\mathrm{cm}^{-3}]}}(k_P R_b)^4. \tag{2.29}$$

Equation (2.29) demonstrates that a larger charge Q_s can be accelerated without increasing the energy spread by choosing the start of the acceleration at a lower accelerating field E_s, but at the cost of a smaller energy gain.

Equation (2.29) simplifies under the following two assumptions: The laser drives the bubble under matched conditions ($k_\mathrm{P} R_b \approx 2\sqrt{a_0}$ and $a_0 = 2(P/P_c)^{1/3}$ with P_c from equation (2.14)) and the head of the bunch is injected at the highest field near the end of the cavity ($E_s = \sqrt{a_0} E_0$, see section 2.7). The resulting equation is:

$$Q_s[\mathrm{pC}] \approx 1.54 \times \lambda_0[\mu\mathrm{m}] \times \sqrt{P[\mathrm{GW}]}. \tag{2.30}$$

Equation (2.30) indicates that the optimal charge for beam loading scales with the square root of the laser power.

2.7. FIELDS INSIDE THE PLASMA CAVITY

The section describes the fields inside a plasma cavity for the three-dimensional blowout regime as discussed in section 2.4.2. The laser pulse propagates along the positive z-axis in the laboratory frame. The fields inside a plasma cavity can be described in a frame moving at the speed of light in the same direction as the laser pulse. The co-moving frame can be described by the co-moving variable $\xi = z - ct$ and transverse coordinate $r^2 = x^2 + y^2$ which assumes a cylindrical symmetry of the system. The bubble center is at $r = 0$ and $\xi = 0$.

The electromagnetic fields inside a plasma cavity are separable into a longitudinal electric field E_z, a radial electric field E_r and an azimuthal magnetic field B_θ [71]:

$$E_z \approx \frac{E_0}{2} k_\mathrm{P} \xi \quad , \qquad E_r \approx \frac{E_0}{4} k_\mathrm{P} r \qquad \text{and} \qquad B_\theta \approx -\frac{E_0}{4} k_\mathrm{P} r, \tag{2.31}$$

where E_0 is the cold relativistic wave-breaking limit given by equation (2.20). Several characteristics of the plasma cavity can be deduced from equation (2.31):

Maximum accelerating field and energy gain The maximum accelerating field can be found at the back of the plasma cavity ($\xi = R_b$) and reaches $E_\mathrm{max} = \sqrt{a_0} E_0$ for a matched driver according to equation (2.23). Thus, the maximum energy gain is [52]:

$$\Delta E \simeq \frac{2}{3} m_\mathrm{e} c^2 \left(\frac{\omega_0}{\omega_\mathrm{P}}\right) a_0 \tag{2.32}$$

or in practical units:

$$\Delta E[\mathrm{GeV}] \simeq 1.7 \left(\frac{P[\mathrm{TW}]}{100}\right)^{1/3} \left(\frac{10^{18}}{n_\mathrm{e}[\mathrm{cm}^{-3}]}\right)^{2/3} \left(\frac{0.8}{\lambda_0[\mu\mathrm{m}]}\right)^{4/3}. \tag{2.33}$$

Energy spread from linear acceleration gradient The accelerating field can differ along a bunch with a typical length $\propto k_\mathrm{P}^{-1}$. The energy gain depends on ξ which can induce an energy spread along the longitudinal bunch axis. Section 2.6 has demonstrated how the acceleration gradient can be modified in order to reduce the energy spread.

Linear focusing field From the fields in equation (2.31), it follows a linear focusing force toward the cavity axis by calculating the Lorentz-force:

$$F_\perp = e(E_r - c\beta_z B_\theta) = e\frac{E_0}{2}k_\mathrm{P} r. \tag{2.34}$$

The last term of equation (2.34) is only true for electrons which already gained relativistic energies ($\beta_z \approx 1$). In the laboratory frame, electrons at rest ($\beta_z \approx 0$) do not experience focusing by the azimuthal magnetic field B_θ. In this case, electrons are focused by a reduced focusing force $\frac{1}{2}F_\perp(\beta_z = 1)$. When these electrons attain the phase velocity of the wake, they then encounter the full focusing force $F_\perp(\beta_z = 1)$.

Panofsky-Wenzel theorem In the bubble regime, neither the acceleration gradient depends on the radial position r nor the focusing force depends on the longitudinal position ξ, which means $\partial E_z/\partial r = \partial F_\perp/\partial \xi = 0$ [72] and is a particular case of the Panofsky-Wenzel theorem [73]. It ensures emittance conservation since the focusing force is the same along the entire bunch. Additionally, there is no energy spread induced by a radially depending accelerating field.

The force experienced by a particle is related to the potential of the wakefield. Lu et al. [71] introduced the pseudo-potential of a wakefield. The pseudo-potential uses the quasi-static approximation (QSA) [55] in order to provide a simplified description for LWFA. Utilizing the different timescales for plasma oscillation and laser pulse diffraction, QSA assumes that the shape of the driver changes very little while passing by an individual plasma particle. Effects that are caused by the temporal evolution of the laser pulse, such as pump-depletion, are neglected. The pseudo-potential Ψ is given by [71]:

$$\frac{\Psi(r,\xi)}{k_\mathrm{P}E_0} = \frac{r_b(\xi)^2}{4}\left(1 + \beta(\xi)\right) - \frac{r^2}{4}, \tag{2.35}$$

where $r_b^2 = R_b^2 - \xi^2$ and $\beta(\xi)$ is a function of the cavity shape [71]. For a plasma cavity without injected electrons, $\beta(\xi)$ can be neglected. Given by equation (2.31), the fields can be found by deriving Ψ along the axis corresponding to the field. In the case of beam loading ($\beta(\xi) \neq 0$), nonlinear focusing fields are not expected from equation (2.35).

FOCUSING FIELDS WITH A LOAD

The impact of an injected charge on the internal plasma fields can be assessed with numerical simulations. Figure 2.6 shows the electromagnetic fields inside the plasma cavity extracted from particle-in-cell (PIC) simulations (see appendix D). The effective focusing force is the Lorentz force (equation (2.10)) which combines the transverse electric field $E_y(x = 0)$ shown in figure 2.6a and the azimuthal magnetic field $B_x(x = 0)$ shown in figure 2.6b. Even though E_y and B_x separately indicate that the bunch fields are stronger than the cavity fields, the Lorentz force on a test electron is uniform along ξ, as shown in figure 2.6c. The deformations of the transverse electric and magnetic field equally compensate each other. The cavity fields are prolonged at the

back due to the large injected charge of more than 120 pC. The prolongation of the cavity strongly indicates beam loading as discussed in section 2.6.

An explanation for the different behavior of E_y, B_x, and $F_\perp$ can be found by the relativistic energy of the electrons, as shown in the longitudinal phase space in figure 2.6d. The electron bunch has gained an energy of about 150 MeV and thus is highly relativistic. The Lorentz transformation of the bunch's Coulomb field into the cavity frame introduces a magnetic field from the bunch. In the relativistic limit ($\gamma \gg 1$), the magnetic and electric field of the bunch are of the same order and compensate each other, which can explain the observations in figure 2.6.

TEMPORAL EVOLUTION OF THE FOCUSING FORCE

In section 2.6, beam loading and its impact on the accelerating field was explained. The importance of the self-field of the injected charge on the focusing forces becomes more clear when different stages of the acceleration process are compared with different bunch energies. Here, two cases will be compared: a highly relativistic bunch after acceleration and a low energy bunch close to injection.

Figure 2.7 shows the case for a bunch near the end of the plasma channel with $z = 2.2$ mm. In this case, the electrons have gained significant energy and are highly relativistic. The focusing force F is presented by figure 2.7a and can be compared with figure 2.6. Along ξ, the focusing force extends further to the back of the cavity. Inside the plasma cavity, F is linear along y and independent of ξ, as depicted by the lineouts in figure 2.7b. The lineouts illustrate the focusing force at three different positions: Free cavity (green), front of the bunch (orange) and back (blue). The color of the lineouts corresponds to the lines in figure 2.7a. The lineouts agree with the theoretical value from equation (2.34) which is shown by the black dashed line. As seen by the phase space in figure 2.7c, the injection of electrons has completed. The injected electrons have gained significant energy of $\sim$250 MeV which is more than in the previous case shown by figure 2.6.

Figure 2.8 shows the focusing force close to injection. Similar to the previous case, the focusing force in figure 2.8a and 2.8b is independent of ξ and linear in y. But, the focusing force of the cavity is not prolonged at the back, which indicates that the cavity is more spherical than at later stages. As shown by figure 2.8c, electrons have only gained energies smaller than 70 MeV.

In conclusion, as shown by the figures 2.7 and 2.8, the focusing fields can be linear in y and independent of ξ inside the cavity at injection and at the end of acceleration. Thus, the Panofsky-Wenzel theorem can be applied and can indicate that the transverse beam quality is preserved by the focusing force. Furthermore, the same holds true for the part of the cavity extended by beam loading. The length of the prolongation can depend on the state of the injected electrons, e.g., at the injection or after the acceleration. Therefore, even with beam loading affecting the cavity's length, the cavity can maintain a linear focusing force for injected electrons.

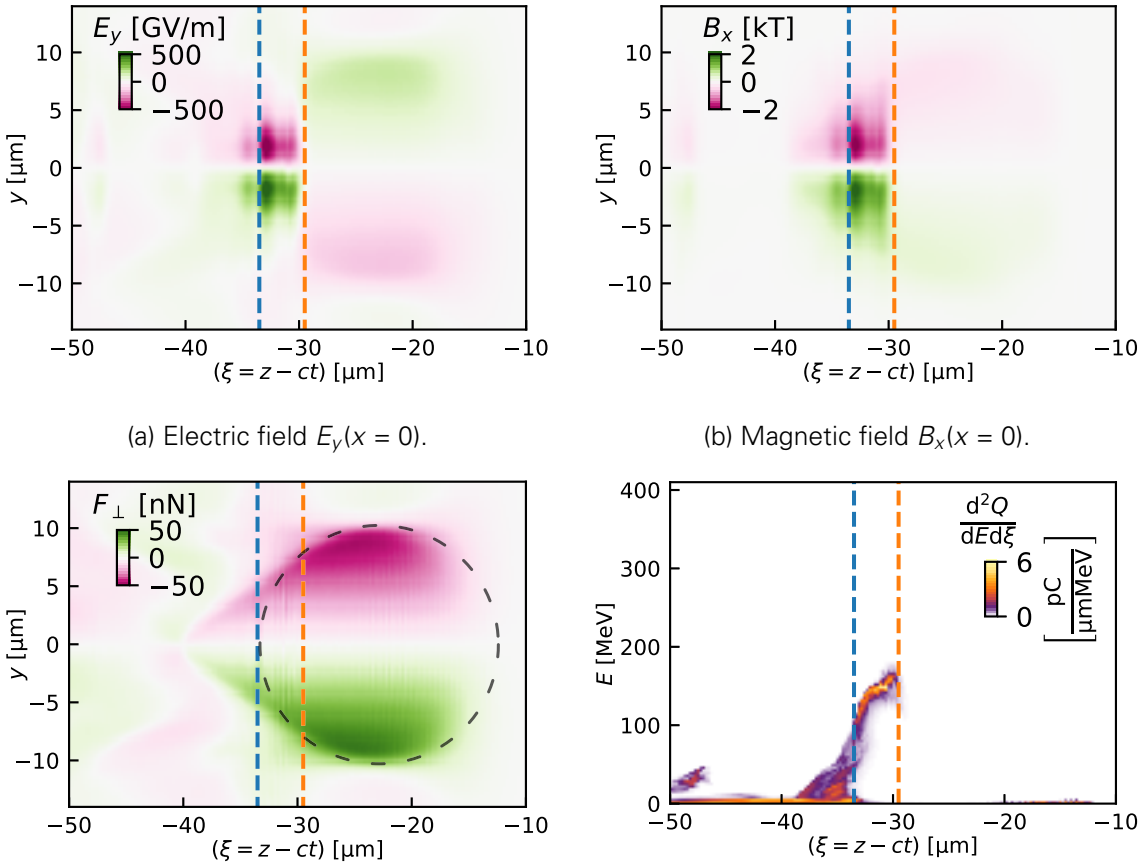

(a) Electric field $E_y(x = 0)$.

(b) Magnetic field $B_x(x = 0)$.

(c) Effective focusing force $F_\perp(x = 0) = e(E_y - cB_x)$.

(d) Longitudinal phase space.

Figure 2.6.: **Transverse fields inside the plasma cavity:** The data is extracted from particle-in-cell (PIC) simulations (see appendix D) at the plane perpendicular to the laser polarization at $z = 1.5\,\text{mm}$. The dashed lines (blue and orange) mark the head and tail of the bunch. The self-fields of the injected bunch deform the transverse electric field in (a) and magnetic field in (b). The Lorentz force $F_\perp = e(E_y - cB_x)$ in (c) shows no indication of the effect from the injected charge. The dashed black circle marks a perfect spherical cavity. The longitudinal phase space in (d) indicates a bunch energy of around 150 MeV.

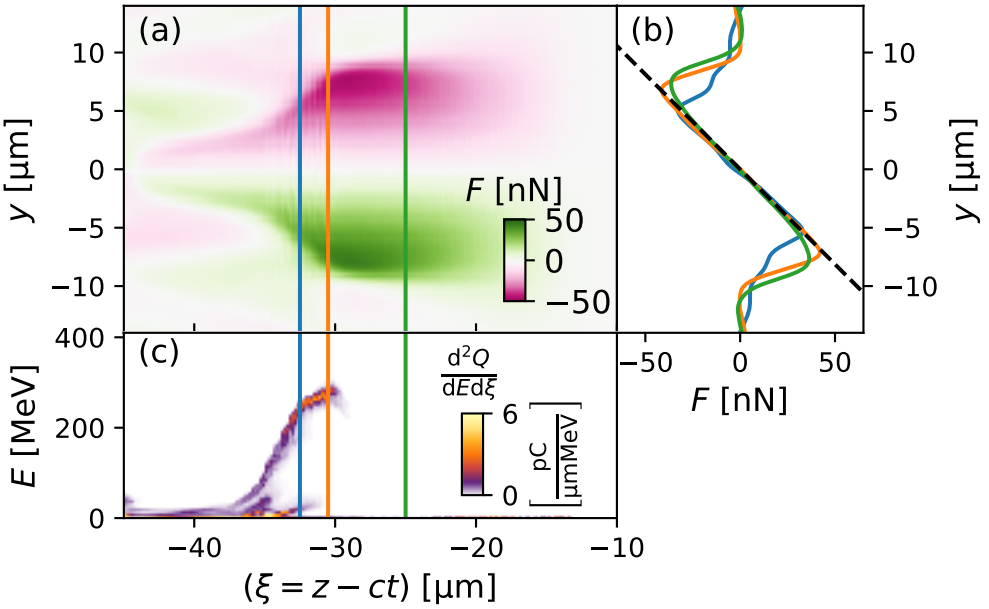

Figure 2.7.: **Focusing force on the accelerated electron bunch:** The focusing force F (a), lineouts of F (b) and the longitudinal phase space (c) are presented at $z = 2.2\,\mathrm{mm}$. The explanation is given in the text.

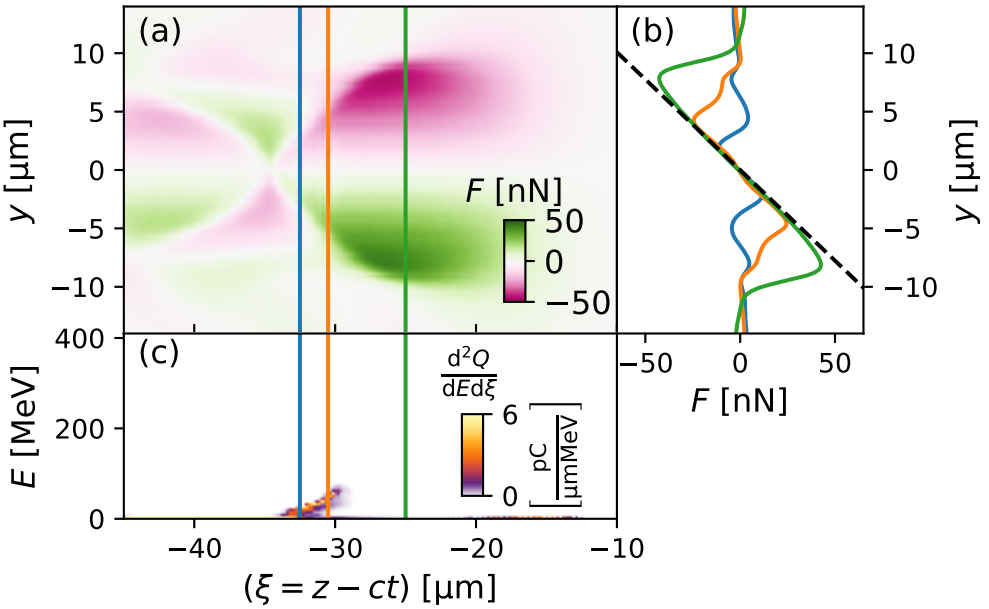

Figure 2.8.: **Focusing force at injection:** The focusing force F (a), lineouts of F (b) and the longitudinal phase space (c) are presented at $z = 1.1\,\mathrm{mm}$. The explanation is given in the text.

3. THEORETICAL CONSIDERATIONS FOR BETATRON RADIATION

Chapter 2 showed that a laser wakefield accelerator possesses both accelerating and focusing fields. The accelerating field helps electrons to gain relativistic energies. The transverse fields direct electrons toward the propagation axis of the plasma cavity. An electron with a transverse offset experiences a restoring force from the focusing fields toward the beam axis. It accelerates, overshoots the beam axis and eventually oscillates around the beam axis. First studied in a betatron [74], the transverse periodic motion is called betatron oscillation. The topic of this chapter is the radiation emanating from these oscillations, called betatron radiation.

The first section 3.1 starts with the analogy between magnetic wigglers and betatron radiation from LWFA. Section 3.2 discusses the details of radiation from a single electron inside a focusing channel. The following section 3.3 gives details about betatron radiation from an electron which is longitudinally accelerated while emitting betatron radiation. Section 3.4 shows simulated radiation from single electrons and electron bunches in LWFA. At last, section 3.5 discusses the electron dynamics in the transverse phase space.

3.1. ANALOGY TO MAGNETIC WIGGLER

Accelerated charged particles, such as electrons moving along a curved path, will emit radiation. At relativistic speeds, the radiation is boosted in a narrow cone oriented in the forward direction of the motion [75]. Typically, magnetic fields are utilized to force electrons on curved trajectories which can create synchrotron radiation. Synchrotron facilities systematically introduce insertion devices on an electron beamline to harvest the radiation for various experiments [76]. Three different types of commonly deployed insertion devices are presented in figure 3.1: bending magnet, undulator and wiggler [46].

Electrons traveling in a homogeneous magnetic field of a bending magnet perform a circular motion confined by the Lorentz force. The acceleration is directed to the center of the circle. The radiation caused by the acceleration is limited to a small

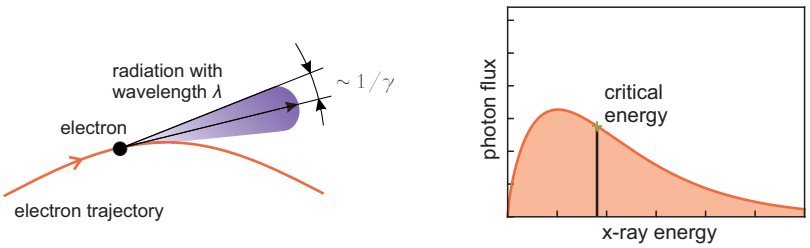

(a) Radiation from a bending magnet.

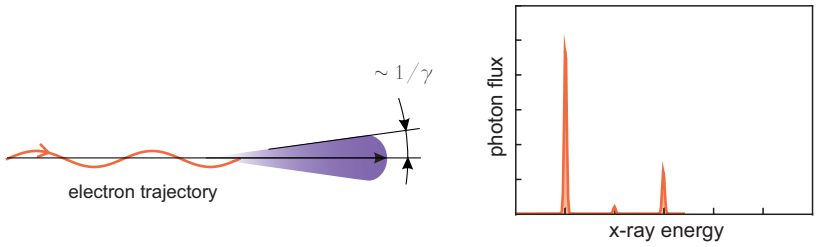

(b) Undulator radiation.

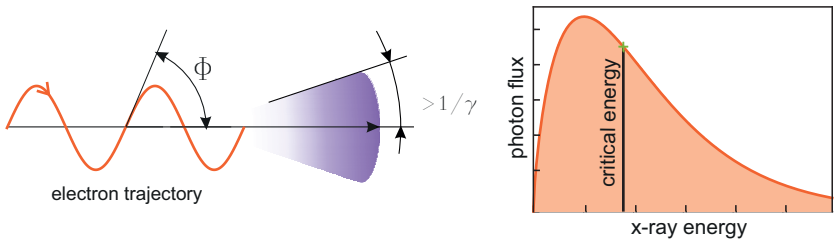

(c) Wiggler and synchrotron radiation.

Figure 3.1.: **Three types of radiation sources in a synchrotron facility.** The electron energy is denoted with γ.

radiation cone with a critical angle of $\sim 1/\gamma$ where γ is the Lorentz factor. The radiated spectrum from a bending magnet is typically as broad as "white light" from x-ray tubes and is characterized by the critical energy E_c. For photon energies much larger than E_c the synchrotron radiation is negligible and decreases exponentially. For a bending magnet, the critical energy is given by [46]:

$$E_c[\text{keV}] = 0.665 E_e^2[\text{GeV}] B[\text{T}], \tag{3.1}$$

where E_e is the electron bunch energy and B is the magnetic field strength. As an example, the 6 GeV electron beam of the European Synchrotron Radiation Facility (ESRF) in Grenoble is deflected by bending magnets with up to 0.85 T. Thus experiments with x-ray diffraction and spectroscopy can utilize synchrotron radiation with a critical energy of 20 keV.

In the case of undulators or wigglers, the number of photons and thus the flux is dramatically increased by a factor $\sim 2N$ for electrons that traverse an alternating set of magnets with N periods. Here, the electron trajectory $x(z)$ along the z-axis can be

described by a sinusoidal function:

$$x(z) = x_0 \sin(k_u z), \tag{3.2}$$

where x_0 is the maximal amplitude and $k_u = 2\pi/\lambda_u$ with λ_u the wavelength of one period. For each turn, radiation as in the case of the bending magnet is emitted. The superposition of the radiation cones leads to the $2N$-fold increase of flux.

Two regimes can be distinguished: Undulator and wiggler regime. In the first regime, the maximal angle ϕ of the trajectory to the z-axis is smaller than the typical emission angle of $1/\gamma$. In contrast to that, the wiggler regime has $\phi \gg 1/\gamma$. The wiggler strength parameter $K = \phi\gamma$ defines the transition from undulator to wiggler regime and is given by:

$$K = \frac{eB\lambda_u}{2\pi m_e c}, \tag{3.3}$$

where e is the elementary charge, m_e is the electron's rest mass and c is the speed of light.

The two regimes strongly differ in their radiated spectral characteristics. The spectrum of an undulator ($K \ll 1$) consists of one or more narrow lines with a fundamental wavelength of $\lambda \propto \lambda_u/(2\gamma^2)$. The emission is confined within a narrow cone with half-opening angle $1/(\gamma\sqrt{N})$. In the wiggler case ($K > 1$), the large deflection leads to an emission angle of K/γ and a broadband spectrum with a critical energy E_c:

$$E_c = \frac{3\pi c\hbar\gamma^2}{\lambda_u} K, \tag{3.4}$$

where $\hbar = h/(2\pi)$ with h as Planck constant.

TRAJECTORIES IN A PLASMA WIGGLER

The principle of a plasma wiggler is similar to the generation of short wavelength radiation at synchrotrons. In such a facility, highly relativistic electrons travel through insertion devices where magnetic fields bend the trajectories of the electrons. However, electrons in a wakefield gain energy while performing transverse oscillations at the same time. Focusing forces from the wakefield as discussed in section 2.7 restrain the electron trajectories and cause these oscillations. Consequently, similar parameters such as K and E_c can be used to describe the wiggler spectrum and the betatron spectrum.

As shown in section 2.7, the force experienced by an electron in a plasma cavity can be separated into two components. These are the accelerating force $\vec{F}_\parallel$ and the focusing force $\vec{F}_\perp$ [77]:

$$\frac{\mathrm{d}\vec{p}}{\mathrm{d}t} = \vec{F}_\parallel + \vec{F}_\perp \simeq -\frac{m_e\omega_P^2}{2}(\xi\vec{e}_z + r\vec{e}_r), \tag{3.5}$$

where $\vec{e}_z$ and $\vec{e}_r$ are the unit vectors along the acceleration axis and in the transverse plane, respectively. The plasma frequency ω_P is given by equation (2.1) and $\xi = z - ct$. Without any loss of generality, the electron orbit plane is (x, z) with $\vec{e}_r = \vec{e}_x$ and $r = x$.

Along the x-axis, equation (3.5) simplifies in the case with no acceleration (γ = const) to:

$$\frac{\mathrm{d}^2 x}{\mathrm{d}t^2} = -\frac{\omega_\mathrm{P}^2}{2\gamma} x. \tag{3.6}$$

This is the differential equation of a harmonic oscillator with the possible solution:

$$x = x_0 \cos(\omega_\beta t), \tag{3.7}$$

where x_0 is the maximal amplitude and $\omega_\beta = \omega_\mathrm{P}/\sqrt{2\gamma}$ is the betatron frequency.

In section 3.3, the expressions are expanded to the case with longitudinal acceleration. The next section will show the typical properties of a synchrotron radiation spectrum from electrons without energy gain.

3.2. BETATRON RADIATION WITH CONSTANT ELECTRON ENERGY

The most general description of the emitted radiation from an accelerated charged particle is derived from the Liénard-Wiechert potential. The radiated energy dI per unit solid angle dΩ and frequency dω of an electron moving along $\vec{r}$ is [78]:

$$\frac{\mathrm{d}^2 I}{\mathrm{d}\omega \mathrm{d}\Omega} = \frac{e^2}{4\pi^2 c} \left| \int \frac{\vec{n} \times [(\vec{n} - \vec{\beta}) \times \dot{\vec{\beta}}]}{(1 - \vec{\beta} \cdot \vec{n})^2} e^{i\omega(t - \vec{n} \cdot \frac{\vec{r}(t)}{c})} \mathrm{d}t \right|^2, \tag{3.8}$$

where $\vec{n}$ is the normalized direction to the detector. The trajectory of the electron defines the position $\vec{r}(t)$, the velocity $\vec{\beta}(t) = \dot{\vec{r}}/c$ and the acceleration $\dot{\vec{\beta}}(t)$. The dot denotes the temporal derivative. Equation (3.8) clearly indicates that the acceleration ($\dot{\vec{\beta}} \neq 0$) is essential for the emission of radiation.

For an electron on an orbit with curvature radius ρ, the spectrum can be expressed as [78]:

$$\frac{\mathrm{d}^2 I}{\mathrm{d}\omega \mathrm{d}\Omega} = \frac{e^2}{3\pi^2 c} \left(\frac{\omega\rho}{c}\right)^2 \left(\frac{1}{\gamma^2} + \theta^2\right)^2 \left[K_{2/3}^2(\xi) + \frac{\theta^2}{\gamma^{-2} + \theta^2} K_{1/3}^2(\xi)\right] \tag{3.9}$$

with

$$\xi = \frac{\omega\rho}{3c} \left(\frac{1}{\gamma^2} + \theta^2\right)^{3/2}, \tag{3.10}$$

where θ is the angle between detection point and z-axis. The spectral shape is described by the modified Bessel functions of the second kind $K_{2/3}(\xi)$ and $K_{1/3}(\xi)$. For on-axis radiation ($\theta = 0$), the critical frequency ω_c is defined with $\xi = 1/2$ as:[1]

$$\omega_\mathrm{c} = \frac{3}{2} \gamma^3 \frac{c}{\rho}. \tag{3.11}$$

[1] There are two definitions for the critical energy. One may find literature [78, 79] that uses $\xi = 1$. This thesis follows the original definition of $\xi = 1/2$ from Schwinger [80] that is also used in more recent literature [75].

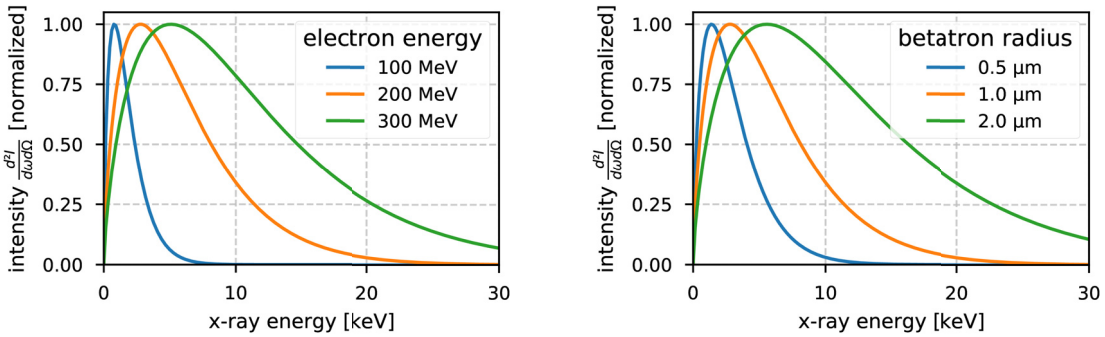

(a) Different electron energies.

(b) Different betatron radii.

Figure 3.2.: **Typical synchrotron radiation spectra for different parameters:** The shape of the synchrotron spectrum depends on the electron energy and the betatron radius. The plasma density is $5 \times 10^{18}\,\mathrm{cm}^{-3}$. For (a) is the betatron radius is 1 µm and for (b) the electron energy is 200 MeV.

Using the minimal curvature radius $\rho = 1/(k_\beta^2 r_\beta)$ of a sinusoidal function $r_\beta \sin k_\beta x$,the critical frequency can be written more conveniently as [79]:

$$\omega_\mathrm{c} \simeq \frac{3}{2}\gamma^2 \frac{\omega_\mathrm{P}^2}{c} r_\beta, \tag{3.12}$$

where r_β is the betatron radius. The strength of the oscillations is given by the wiggler strength parameter [79]:

$$K = \gamma k_\beta r_\beta. \tag{3.13}$$

Figure 3.2 illustrates typical betatron spectra for different betatron radii and electron energies according to equation (3.9). An increase in electron energy γ has the same effect on the spectrum as an increase in r_β. The critical frequency shifts to higher x-ray energies and the bandwidth increases. For frequencies higher than ω_c, the spectral flux decreases exponentially with $\propto \gamma^2 \omega/\omega_\mathrm{c} e^{-\omega/\omega_\mathrm{c}}$. For frequencies lower than ω_c, the flux can be approximated with $\propto \gamma^2 \left(\omega/\omega_\mathrm{c}\right)^{2/3}$.

The total emitted spectrum is given by the integration of equation (3.9) over the solid angle:

$$\frac{\mathrm{d}I}{\mathrm{d}\omega} = \sqrt{3}\frac{e^2}{c}\gamma\frac{\omega}{\omega_\mathrm{c}} \int_{\omega/\omega_\mathrm{c}}^{\infty} \mathrm{d}x K_{5/3}(x), \tag{3.14}$$

where $K_{5/3}(x)$ is a modified Bessel function of the second kind. The energy integration of equation (3.9) returns the total emitted energy at the observation angle θ:

$$\frac{\mathrm{d}I}{\mathrm{d}\Omega} = \frac{7e^2}{16\rho} \frac{1}{(\gamma^{-2} + \theta^2)^{5/2}} \left[1 + \frac{5}{7}\frac{\theta^2}{\gamma^{-2} + \theta^2}\right]. \tag{3.15}$$

NUMBER OF EMITTED PHOTONS

The relativistically correct Larmor formula for the radiated power P_{rad} from an electron is given by [75]:

$$P_{\mathrm{rad}} = \frac{2}{3}\frac{e^2 c}{(m_{\mathrm{e}}c^2)^2}\left[\left(\frac{\mathrm{d}\vec{p}}{\mathrm{d}\tau}\right)^2 - \frac{1}{c^2}\left(\frac{\mathrm{d}E}{\mathrm{d}\tau}\right)^2\right], \tag{3.16}$$

where $\vec{p} = \gamma\beta m_{\mathrm{e}}c$ is the electron momentum, $E = \gamma m_{\mathrm{e}}c^2$ is the electron energy and $\mathrm{d}\tau = \mathrm{d}t/\mathrm{d}\gamma$ is the Lorentz-invariant time. From equation (3.16) it follows that the radiated power of synchrotrons scales strongly with γ^4. The average radiated power $\langle P_{\mathrm{rad}}\rangle$ of an electron following a planar sinusoidal trajectory such as in equation (3.7) is [81]:

$$\langle P_{\mathrm{rad}}\rangle = \frac{4\pi^2 e^2 c}{3}\frac{\gamma^2 K^2}{\lambda_\beta^2}, \tag{3.17}$$

where $\lambda_\beta = 2\pi/k_\beta$ is the betatron wavelength. Integration of the average radiated power $\langle P_{\mathrm{rad}}\rangle$ over time returns the average photon energy E_{rad}:

$$E_{\mathrm{rad}} = \int \langle P_{\mathrm{rad}}\rangle \mathrm{d}t = \frac{4\pi^2 e^2}{3}\frac{\gamma^2 K^2}{\lambda_\beta}. \tag{3.18}$$

From equation (3.18), the average number of emitted photons N_{Ph} can be estimated by the average photon energy. For a synchrotron spectrum, the average photon energy is $8/(15\sqrt{3})\hbar\omega_{\mathrm{c}}$ [81] and thus the average photon number is:

$$N_{\mathrm{Ph}} \approx \frac{5\sqrt{3}\pi}{6}\alpha K, \tag{3.19}$$

where $\alpha = e^2/(\hbar c)$ is the fine structure constant.

3.3. RADIATION FROM ELECTRONS GAINING ENERGY

For an electron performing betatron oscillations and simultaneously gaining energy, equation (3.6) becomes [82]:

$$\ddot{x} + \frac{\dot{\gamma}}{\gamma}\dot{x} + \frac{\omega_{\mathrm{P}}^2}{2\gamma}x = 0. \tag{3.20}$$

A solution for the differential equation (3.20) can be found from the Wentzel-Kramers-Brillouin (WKB) approximation and the adiabaticity of the betatron oscillation ($\omega_\beta^{-2}\mathrm{d}\omega_\beta/\mathrm{d}t \ll 1$) [77, 81, 82]:

$$x = r_\beta(t)\cos(\phi_\beta(t)) \tag{3.21}$$

with

$$r_\beta(t) = r_{\beta 0}\left(\frac{\gamma(t)}{\gamma_0}\right)^{-1/4} \quad \text{and} \quad \phi_\beta(t) = \int_0^t \mathrm{d}t\omega_\beta(t)), \tag{3.22}$$

where amplitude $r_\beta(t)$ and phase $\phi_\beta(t)$ are now functions of the electron's energy γ at time t. The initial values are $\gamma_0 = \gamma(t = 0)$ and $r_{\beta 0} = r_\beta(t = 0)$.

Figure 3.3 illustrates three-dimensional electron trajectories obtained from equation (3.21) with differently chosen initial conditions. Depending on the angular momentum $L_z = xp_y - yp_x$[2], the electron trajectory can be flat ($L_z = 0$, 3.3a), elliptical ($0 < |L_z| < L_{z,max}$, 3.3b) or circular ($L_z = \pm L_{z,max}$). A measured angular profile can provide indications for an electron's trajectory and angular momentum [31]. The angular momentum $L_z = xp_y - yp_x$ can be conserved during the acceleration for symmetric plasma cavities with static fields [31]. For plasma cavities with asymmetric focusing fields, Thaury et al. [30] have shown that L_z can be not conserved.

Figure 3.4 illustrates an electron trajectory obtained by particle-in-cell (PIC) simulations. The betatron oscillations are visible and oriented along the x-axis that is identical with the laser polarization axis. Mangles et al. [83] has previously indicated for laser pulses longer than a plasma wavelength, that the electron bunch can be elliptically elongated along the driver laser polarization. This can be caused by the interaction of the electrons with the electric field of the laser pulse [83]. Other groups [32, 33, 84] have indicated that preferred electron orbits occur along the axis of the laser polarization for ionization-induced injection, supporting this hypothesis.

BETATRON RADIATION MODELS

The parameters of betatron oscillation, such as r_β and ω_β, are energy dependent as shown by equation (3.22). As a consequence of that, parameters such as ω_c and K become time dependent, where [25]:

$$\omega_c(t) = \frac{3}{2}\frac{\omega_P^2}{c} r_{\beta 0} \gamma_0^{1/4} \gamma(t)^{7/4} \tag{3.23}$$

and

$$K(t) = \frac{\omega_P}{\sqrt{2}c} r_{\beta 0} \gamma_0^{1/4} \gamma(t)^{1/4}, \tag{3.24}$$

where $r_{\beta 0}$ and γ_0 are the initial radius and electron energy. A typical recorded betatron spectrum is an integration of the complete LWFA, i.e., summing radiation spectra from the start to the end of the acceleration. Although, it is assumed by many groups [42, 85–88] that the betatron spectrum is comparable with a synchrotron spectrum given by equation (3.9). Here, models are described that consider the acceleration process. The models are tested with simulated radiation spectra in section 3.4.

A betatron radiation model based on linear acceleration is suggested by Glinec et al. [89]:

$$\gamma(t) = \gamma_0 + ut, \tag{3.25}$$

where $u = eE_z/(m_e c)$ and E_z is the accelerating field strength. The initial electron energy γ_0 is related to the wake's phase velocity v_ϕ. Ref. [89] used the electron pointing of continuously injected LWFA bunches to observe betatron oscillations in the recorded electron spectrum. The linear acceleration can hold for situations, when

[2] (x, y) and (p_x, p_y) are the transverse positions and momenta, respectively.

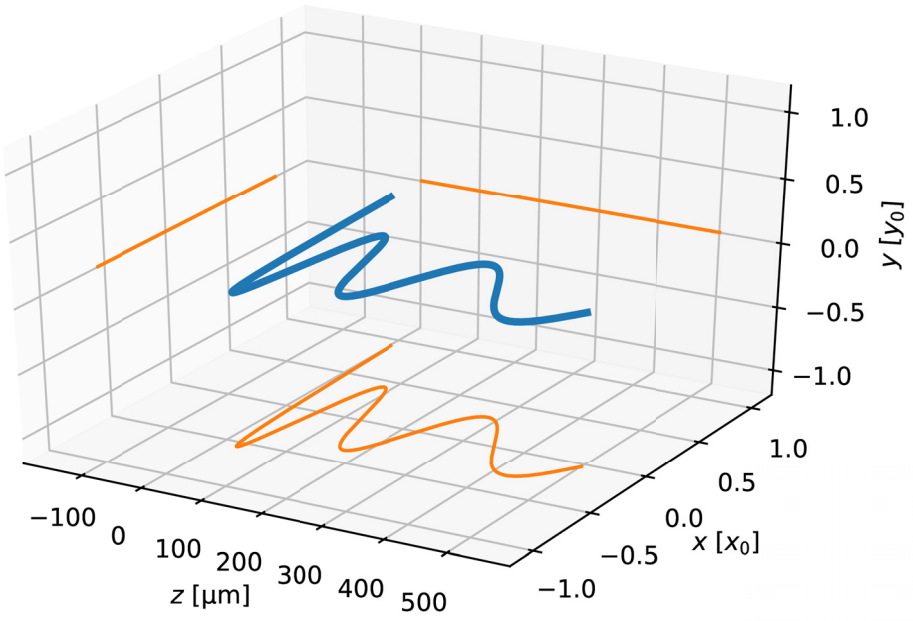

(a) Zero angular momentum.

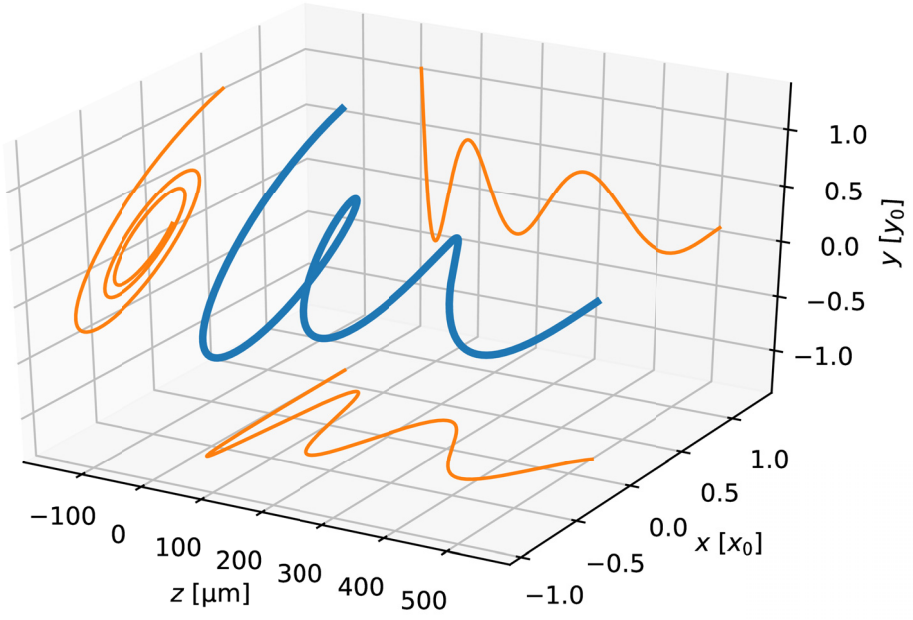

(b) Non-zero angular momentum.

Figure 3.3.: **Electron trajectory inside the plasma channel after trapping:** The thick blue line illustrates the trajectory in three dimensions. The orange lines show the projections onto the corresponding two-dimensional planes. The electron is accelerated along the z-axis (linear energy gain of 176 MeV). (a) shows an electron injected with zero angular momentum ($L_z = 0$). (b) illustrates the case for electrons with non-zero angular momentum ($0 < |L_z|$).

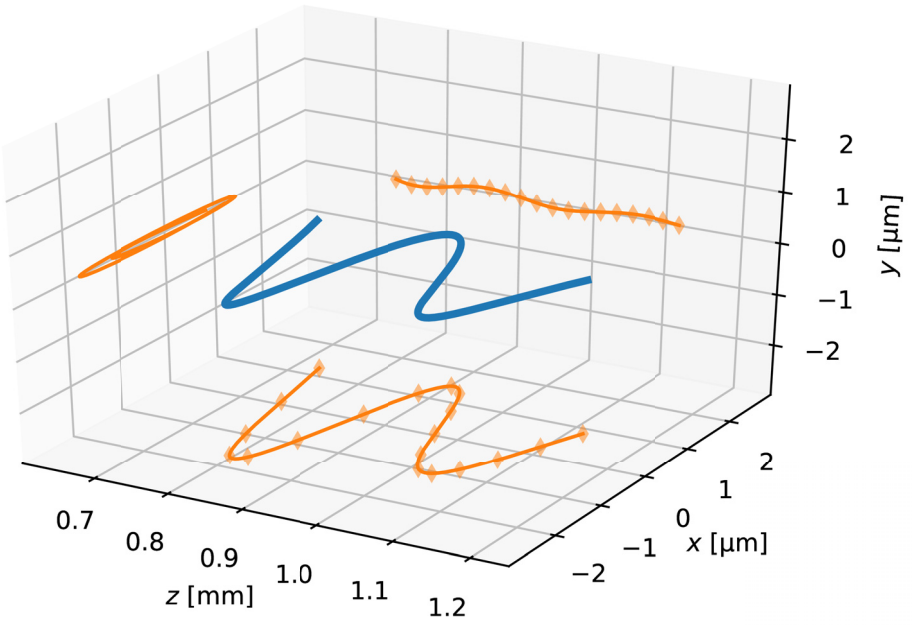

Figure 3.4.: **Example for electron trajectory from simulations:** The blue line indicates the trajectory in the (x, y, z) space. The orange lines are projections to the corresponding two-dimensional planes and the marker represents the data obtained by simulation. The details of the simulation can be found in appendix D.

the energy gain is smaller than the maximum possible energy gain and the dephasing length is not reached.

Equation (3.25) can be combined with the synchrotron equation (3.9) to obtain:

$$\frac{\mathrm{d}^2 I}{\mathrm{d}\omega \mathrm{d}\Omega}_{\mathrm{lin}}(\gamma_f, n_\mathrm{e}, r_\beta) = \sum_{\gamma=\gamma_0}^{\gamma_f} \frac{\mathrm{d}^2 I}{\mathrm{d}\omega \mathrm{d}\Omega}\left(\gamma, n_\mathrm{e}, r_\beta \to r_\beta \left(\frac{\gamma_f}{\gamma}\right)^{1/4}\right), \tag{3.26}$$

where γ_f is the final electron energy. The factor $\left(\gamma_f/\gamma\right)^{1/4}$ at r_β takes into account that betatron oscillations are damped when the electron gains energy.

An x-ray detector such as presented in section 4.4 can count single photons within a solid angle of $\Delta\Omega$. In this case, the energy-resolved photon spectrum $\mathrm{d}N/\mathrm{d}E$ is of interest. The integration of equation (3.26) yields the number of emitted photons N with the energy E:

$$\frac{\mathrm{d}N}{\mathrm{d}E}(\gamma_f, n_\mathrm{e}, r_\beta) = \frac{1}{\hbar^2 \omega} \int_{\Delta\Omega} \mathrm{d}\Omega \frac{\mathrm{d}^2 I}{\mathrm{d}\omega \mathrm{d}\Omega}_{\mathrm{lin}}(\gamma_f, n_\mathrm{e}, r_\beta). \tag{3.27}$$

Folding with a Gaussian bunch distribution then yields the spectrum of an electron bunch:

$$\frac{\mathrm{d}N}{\mathrm{d}E}_{\mathrm{bunch}}(\gamma_f, n_\mathrm{e}, r_\beta) = \int \mathrm{d}r \exp\left(-\frac{r^2}{2r_\beta^2}\right) \frac{\mathrm{d}N}{\mathrm{d}E}(\gamma_f, n_\mathrm{e}, r). \tag{3.28}$$

Equation (3.28) is used in section 5.2 to implement a model for the experiments shown in chapter 6.

BUBBLETRON RADIATION

Thomas et al. [90] provided calculations for the accumulated radiation from injection until dephasing. The produced radiation is named "bubbletron" radiation, in order to distinguish it from the synchrotron spectrum calculated by Esarey et al. [79], where only radiation is considered which is produced with the highest electron energies at the end of the plasma channel. Ref. [90] gives the following expression for the bubbletron spectrum on the cavity axis ($\theta = 0$):

$$\frac{\mathrm{d}^2 I}{\mathrm{d}\omega \mathrm{d}\Omega}_{\mathrm{Thomas}} = \frac{3e^2}{2\pi^3 \varepsilon_0 c} \gamma_{max}^2 A \left(\frac{\omega}{\omega_c^{\max}} \right) \tag{3.29}$$

with the spectral shape function $A(x)$:

$$A(x) = x^2 \int_{-1}^{1} \mathrm{d}\mu \frac{1}{(1-\mu^2)^{3/2}} K_{2/3}^2 \left(\frac{x}{(1-\mu^2)^{7/4}} \right), \tag{3.30}$$

where γ_{max} and $\omega_c^{\max}$ are the maximum values of the Lorentz-factor and the critical frequency, respectively.

A comparison between [90] and [89] has been made by Matsuoka et al. [91] that showed reasonably well agreement with the bubbletron model [90] within its constraints, i.e., electrons reaching the dephasing limit without significant laser depletion.

3.4. SIMULATION OF BETATRON RADIATION

As shown by equations (3.23) and (3.24), the properties of the betatron spectrum can depend on the acceleration process. Thus, it is possible, that the radiation regime changes from the undulator at the start with low electron energies to the wiggler at the end with high electron energies. However, simulated spectra can be used to gain insight.

CLARA (**Cla**ssical **Ra**diation program [92]) simulates the radiated energy per unit frequency and unit solid angle far away from the particle's orbit. The calculation of the spectrally resolved intensity requires the particle trajectory and velocity for the integration of the Liénard-Wiechert potential in equation (3.8). Contrary to previous implementations, the deployed version of CLARA [93] runs efficiently on large CPU clusters by exploiting their parallel architecture, e.g., the Hypnos cluster at the HZDR. This enables a computational speed-up that scales linearly with the number of CPU cores used.

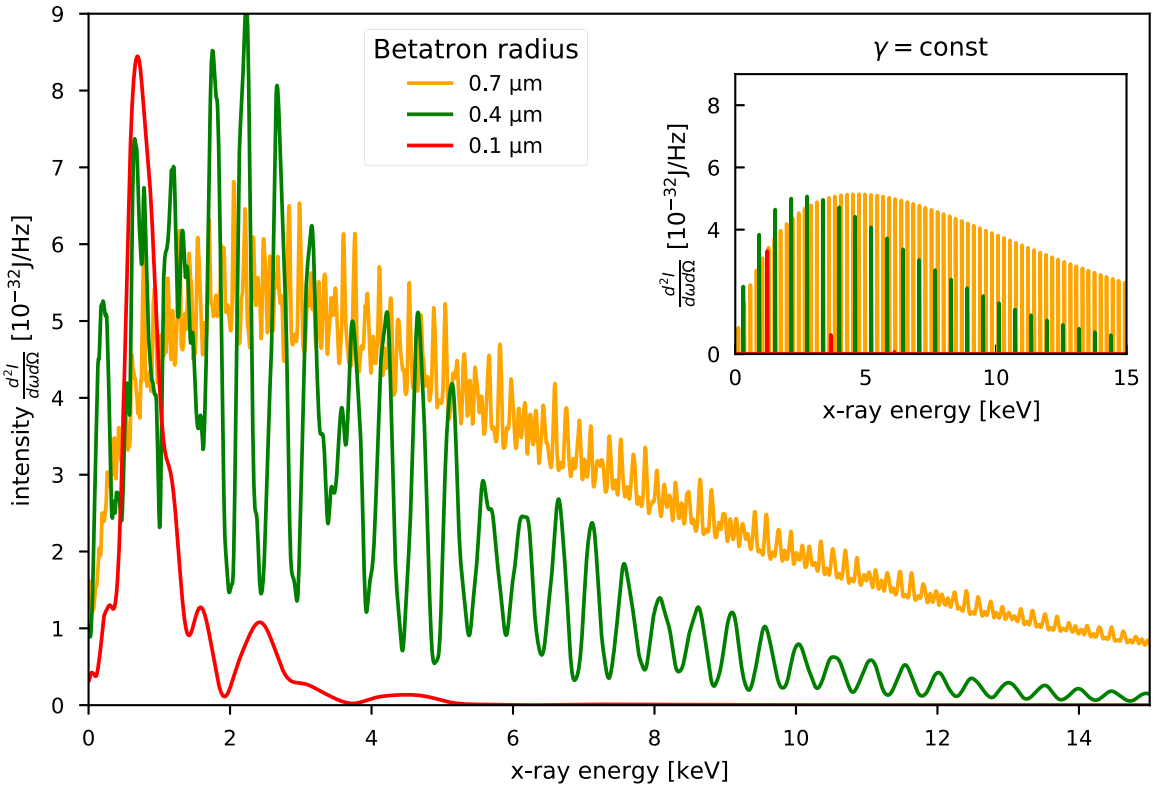

Figure 3.5.: **Betatron radiation from single electron:** The spectra are calculated for single electrons following equation (3.21) The parameters for the simulation are a plasma density of $5 \times 10^{18}\,\mathrm{cm}^{-3}$ and no initial transverse momentum. Electrons start with $\gamma_0 = 9$ and are linearly accelerated to 280 MeV.
The inset illustrates the case for electrons without acceleration, i.e. γ = const. The spectrum is integrated over one oscillation period and multiplied by 1/2. Same colors correspond to the same radii.

3.4.1. RADIATION FROM SINGLE ELECTRON

The simulated spectra are calculated using CLARA with the following assumptions: according to equation (3.21), the electron trajectory is obtained by using the energy dependence from equation (3.25). The initial electron energy $\gamma_0 = 9$ is in the order of the phase velocity of the wake. Furthermore, no initial transverse momentum is assumed.

Figure 3.5 presents the betatron spectrum from a single electron with different final betatron radii r_β. The initial betatron radius $r_{\beta 0}$ is calculated by equation (3.22). An electron with a very small betatron radius of 0.1 µm emits an undulator-like spectrum consisting of a broadened fundamental frequency. The wiggler strength obtained by averaging over equation (3.24) is $K \simeq 0.5$. An electron trajectory with a larger betatron radius (0.4 µm, $K \simeq 2$) emits radiation with a high number of closely spaced harmonics. The trajectory with the largest betatron radius in the plot (0.7 µm, $K \simeq 4$) leads to more harmonics and stronger overlapping in the spectrum. The result can

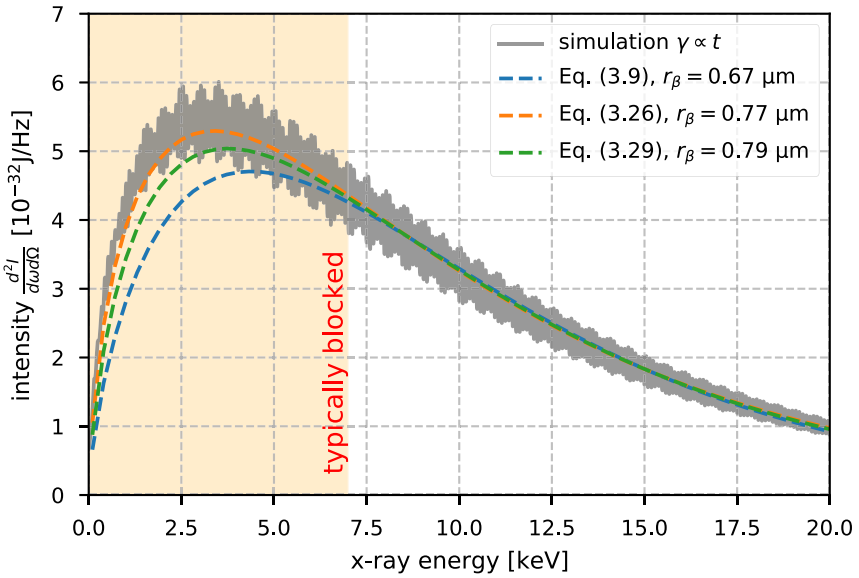

Figure 3.6.: **Comparison of bunch simulations and model spectra:** Betatron radiation from Gaussian bunches is shown for the case with linear acceleration and without acceleration. The simulated spectrum is calculated for electrons following equation (3.21) with $\gamma(t) = \gamma_f = 560$, $r(\gamma_f) = 1\,\mu\text{m}$, $n_e = 5 \times 10^{18}\,\text{cm}^{-3}$ and $\gamma(t = 0) = \gamma_0 = 9$.
The equations (3.9), (3.26) and (3.29) are fitted to the bunch spectrum with $\gamma \propto t$ using a least square algorithm. The orange area with x-ray energies smaller than 7 keV is excluded from the fit, because the energy range is not accessible in typical experiments.

be a typical synchrotron spectrum. The inset of figure 3.5 illustrates the case without acceleration for the same parameters. The width of the harmonics is smaller than in the case with acceleration. In order to compare the intensity, the spectrum with γ = const is scaled to $\lambda_\beta/2$. The height of spectra with the same radius is similar, which indicates that the last half-oscillation contributes the most to the spectrum.

Furthermore, the simulated spectra from CLARA can be used to gain insight into the radiation models that return a good description of the recorded spectra in the experiment. Figure 3.6 compares a simulated spectrum with the different models given by equations (3.9), (3.26) and (3.29). The synchrotron models are fitted to the simulated spectrum with a least-square algorithm. The fit was performed over the experimentally accessible range of 7 keV to 20 keV, as shown in section 5.2. All models show a good agreement with the simulated spectrum. For further calculation, equation (3.26) is preferred because it provides a good compromise between computational speed and physical modeling, i.e., energy gain during the acceleration process.

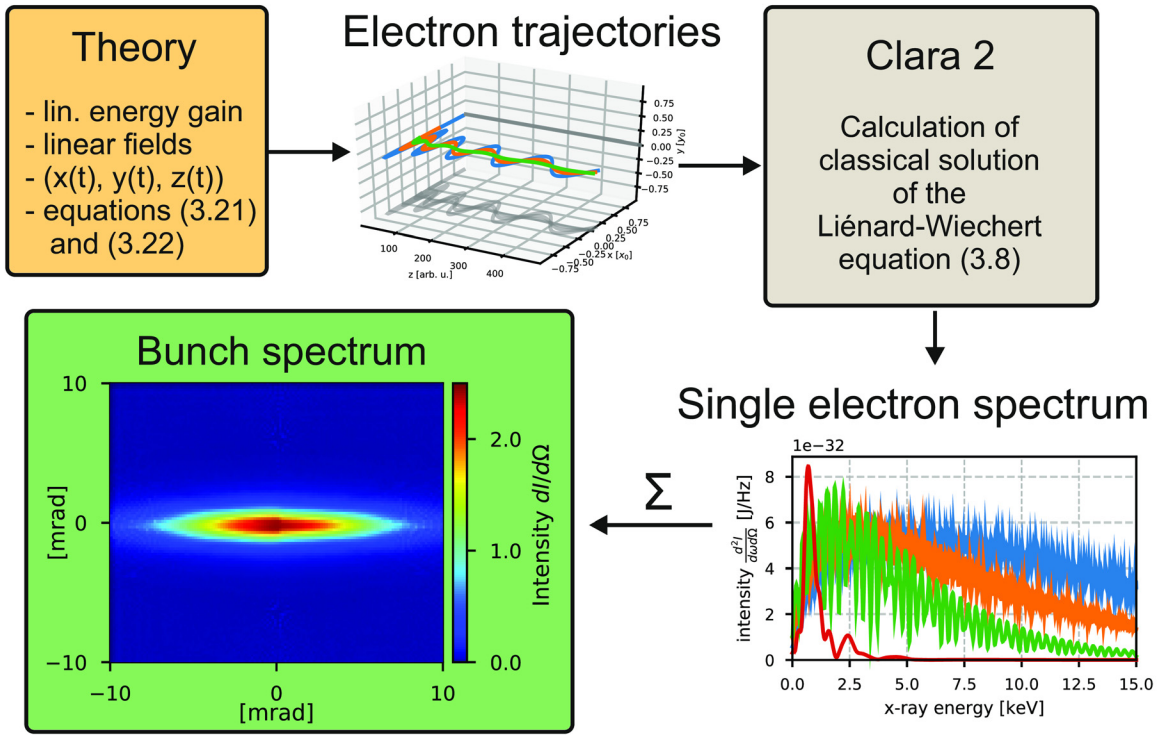

Figure 3.7.: **Simulation of betatron spectrum:** At first, trajectories of electrons according to equation (3.21) with different initial conditions (x_0) are compiled and sampled in time with sufficient fine steps in time. The classical radiation solver CLARA then calculates the radiated spectrum for each trace. Finally, the integration over the particle distribution inside a bunch returns the predicted betatron spectrum.

3.4.2. BETATRON RADIATION FROM AN ELECTRON BUNCH

Figure 3.7 illustrates how the x-ray spectrum is obtained for an electron bunch. A set of electron trajectories with different initial offsets r_0 is generated according to equation (3.21). Then, the trajectories are saved in separate trace files. The radiation solver CLARA uses this data to solve the radiation equations. Then, the radiation is binned in discrete bins and saved for every trajectory in a separate file. At last, a bunch spectrum can be compiled by assembling and weighting several electron traces. The last step illustrates a typical betatron profile for electron traces within the same plane.

Figure 3.8 shows the result for a Gaussian electron bunch. The single traces are weighted by a Gaussian function with a width equal to the betatron radius. The bunch can be accelerated by an LPA with plasma density of $5 \times 10^{18}\,\mathrm{cm}^{-3}$ to an energy of 280 MeV. Energy gain and plasma density are typical for the experiments discussed in chapter 6. To demonstrate the different angular extent, the bunch's electrons oscillate only along the x-axis as shown in figure 3.3a. A bunch with betatron size of 0.1 µm radiates at very low photon energies that are not accessible in the experimental setup shown in chapter 4. Larger bunches with betatron radii of 0.4 µm and 0.7 µm radiate x-ray energies which can be observed in the experiment.

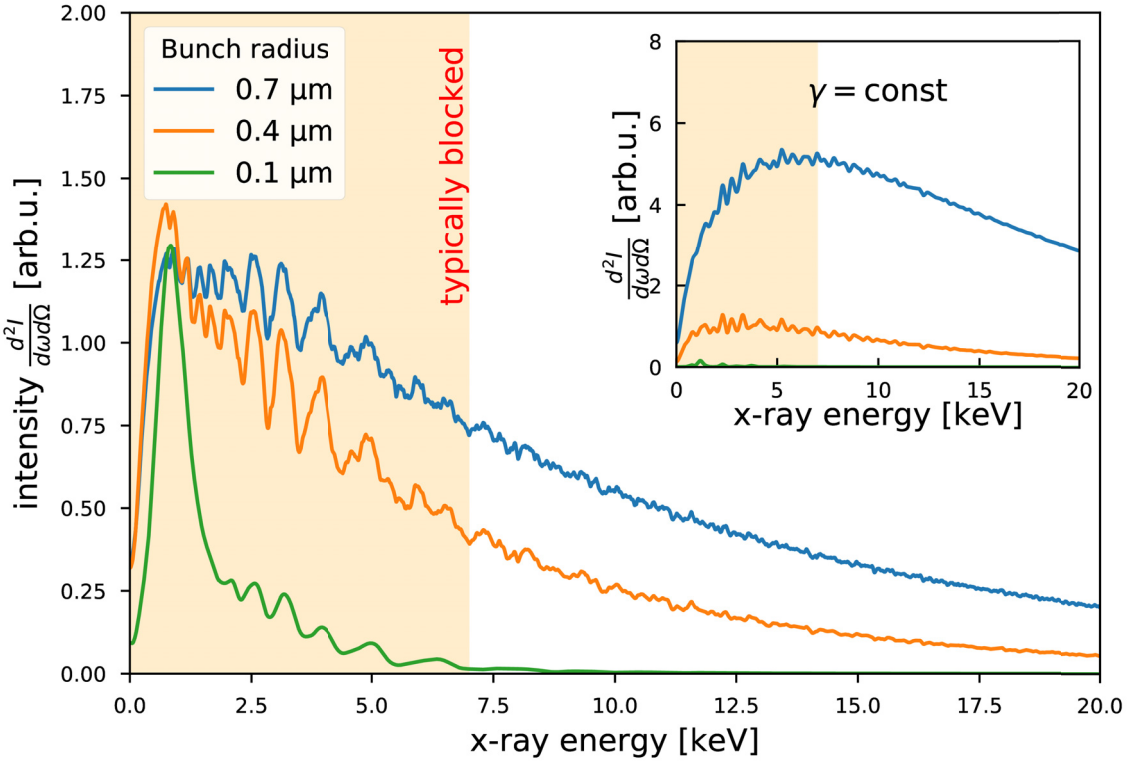

Figure 3.8.: **Betatron spectrum of an electron bunch:** The figure shows the betatron spectrum from a Gaussian electron bunch with different bunch radii. The bunch is accelerated to 280 MeV in an LPA with plasma density of $n_e = 5 \times 10^{18}\,\mathrm{cm}^{-3}$. The inset illustrates the same case but without energy gain (γ = const).

The inset of figure 3.8 illustrates the case without acceleration. A bunch without energy gain radiates more energy at higher photon energies than a bunch gaining energy in an LPA. For linear acceleration, the spectrum seems to be dominated by harmonics at x-ray energies of ∼1 keV. Without acceleration, the spectrum is more similar to the smooth synchrotron spectrum shown in figure 3.2. Experiments such as shown in chapter 6 record only x-ray energies above several keV and thus in the high energy synchrotron part of the spectrum. As a result, synchrotron equations such as (3.9), (3.26) and (3.29) can describe the betatron spectrum instead of more complex calculations including higher harmonics [94].

3.5. TRANSVERSE BEAM DYNAMICS IN THE PHASE SPACE

The previous section concentrated on the transverse spatial extent of the beam described by betatron oscillations. A description of the transverse dynamics of LWFA electrons can be expanded with the transverse momentum $p_x = \gamma m_e \dot{x}$ which enables a description of the dynamics in the transverse phase space (x, p_x).[3] This space is

[3]The remaining transverse phase space (y, p_y) can be treated equally with (x, p_x).

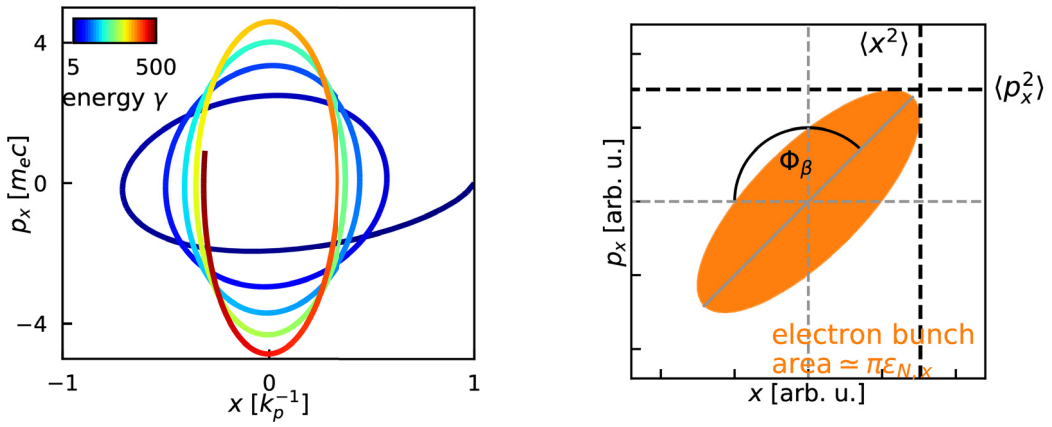

(a) Electron orbit.

(b) Bunch and emittance.

Figure 3.9.: **Transverse phase space:** The electron orbit shown in (a) is calculated from equation (3.21) and $p_x = \gamma m_e \dot{x}$ with a linear acceleration from $\gamma_0 = 5$ to $\gamma = 500$. The phase space of an electron bunch and the definition of the emittance is shown by (b).

only a subspace of the six-dimensional phase space which contains the full information about the three-dimensional position and momentum [95].

Figure 3.9a illustrates an orbit in (x, p_x) of an electron that linearly gains energy in LWFA. The particle experiences focusing forces inside the plasma cavity which lead to oscillations around the propagation axis in x and p_x. As long as the electron is gaining energy, the transverse extent of the oscillation is damped $\propto \gamma^{-1/4}$ and the transverse momentum increases $\propto \gamma^{1/4}$, as shown in section 3.3.

3.5.1. TRANSVERSE BEAM EMITTANCE

The transverse emittance is a figure of merit that can be considered as the area of the electron bunch in (x, p_x) as shown in figure 3.9b. This parameter is crucial for applications of the electron beam. It limits the minimal spot size in colliders, the minimal wavelength of free electron lasers and in general the beamline apertures for beam transport [95].

The normalized transverse emittance is given by [95]:

$$\varepsilon_{N,x} = \frac{1}{m_e c}\sqrt{\langle x^2 \rangle \langle p_x^2 \rangle - \langle x p_x \rangle^2}, \tag{3.31}$$

where $\langle \cdot \rangle$ is the average over all electrons of the bunch. x and p_x are the transverse position and momentum of an electron, respectively.

From equation (3.31) follows that the emittance provides a lower limit for the transverse properties of the bunch:

$$\langle x^2 \rangle \langle p_x^2 \rangle \geq \varepsilon_{N,x}^2 m_e^2 c^2. \tag{3.32}$$

A monoenergetic bunch implies $\langle p_x^2 \rangle / (m_e c)^2 = \gamma^2 \langle \theta_x^2 \rangle$ with θ_x as the geometric divergence. As shown in chapter 6, θ_x can be deduced by experiments.

In laser-wakefield acceleration, the emittance can remain constant when two conditions are fulfilled during the acceleration: Linear focusing forces and a monoenergetic bunch. The first can be true for the bubble regime as mentioned in chapter 2. The latter is challenging for typical LWFA generated bunches.

Some causes of emittance degradation can be as follows [96, 97]:

Phase mixing by finite energy spread: Electrons rotate in (x, p_x) with the energy dependent betatron frequency $\omega_\beta(\gamma)$. The frequency can vary along the bunch since high-energy electrons rotate slower than low-energy electrons. Defined by equation (3.22), the betatron phase ϕ_β is the angle between the initial position in phase space and the position at time t. An energy spread result in a spread in the phase and thus the area occupied in the phase space becomes larger. This phenomenon is called betatron-demixing or decoherence [98].

Longitudinally varying focusing force: Decoherence can also occur when the focusing force $F_\perp$ depends on the longitudinal position ξ along the bunch. Even if the focusing force is still linear along x, it depends on the longitudinal variable ξ. So, the front of the bunch can rotate with a different frequency than the back. This is the case for LWFA in the linear regime [99]. However, for a thin slice of the bunch at a given ξ, the slice emittance can be conserved.

Nonlinear focusing forces: Focusing forces with a non-linear dependence on the transverse variables do not conserve the emittance. For particles encountering non-linear focusing forces, the rotation frequency in (x, p_x) depends on their transverse coordinate. Typically, this is not the case for the bubble regime with linear focusing forces.

Direct interaction with laser pulse: Electrons interacting with the transverse electric field of the laser can gain energy as shown recently in experiment [100, 101]. This case requires an overlap between laser pulse and accelerated electrons, and thus a laser pulse extending the length of the bubble. The superposition of the focusing fields of the wake and the laser can lead to non-linear focusing forces. Thus, it can be seen as a particular case of non-linear focusing.

Space charge forces of the beam can be an important source of non-linearities. For typical Gaussian beams, these forces are non-linear in x, while for a uniform beam they become linear. Wangler et al. [102] calculated the associated emittance growth due to space charge forces:

$$\frac{\mathrm{d}\epsilon^2}{\mathrm{d}t} = -\frac{\langle x^2 \rangle}{4\gamma} \frac{I}{I_A} \frac{\mathrm{d}U}{\mathrm{d}t}, \tag{3.33}$$

where $I_A = ec/r_e$ is the Alfvén current, I the beam current and U is a dimensionless parameter that depends on the bunch's transverse distribution. U is zero for a uniform beam and $U = 0.154$ for a Gaussian bunch. Equation (3.33) indicates that emittance growth induced by space charges can become important for low energy

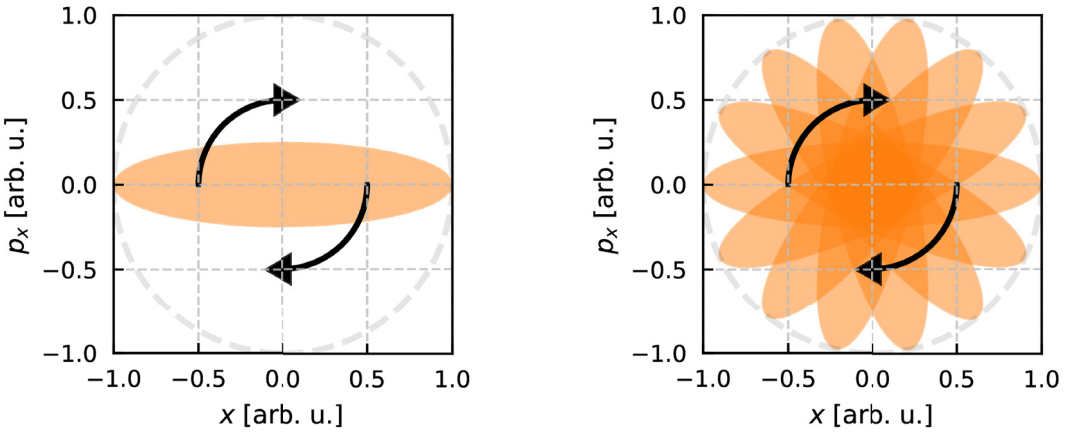

(a) Short injection.

(b) Continuous injection.

Figure 3.10.: **Transverse phase space during injection:** A short injection in (a) fills an ellipse that can rotate in (x, p_x). A continuous injection in (b) gradually fills the transverse phase space. In this case, the bunch still rotates in (x, p_x) but the covered area stays the same, i.e., the phase space is saturated.

bunches with a large current. For very narrow LWFA bunches with ∼1 µm, the emittance degradation caused by space charge effects can be neglected. As an example, a typical LWFA bunch can have an energy of 150 MeV, I = 30 kA and $\sqrt{\langle x^2 \rangle}$ = 1 µm. The evolution from a Gaussian profile to a uniform bunch profile with the same $\langle x^2 \rangle$ will increase the emittance by 0.015 mm mrad. This is below the typical emittance of ∼1 mm mrad [94, 103, 104] and thus can be neglected.

3.5.2. EVOLUTION OF THE TRANSVERSE PHASE SPACE

The transverse electron dynamics start once the electrons are injected in the wakefield, as shown in figure 3.10a. Hence, the evolution of the transverse phase space depends on the duration of the injection [105]. Two cases are possible:

Continuous or long injection If the injection continues for more than π/ω_P, then electrons injected at the beginning have already performed a rotation of more than 180° in the transverse phase space. Figure 3.10b illustrates this case. Thus, the phase space saturates after π/ω_P during the injection. Saturation of the phase space means that the emittance has reached a stable value. The same can be applied to $\langle x^2 \rangle$ and $\langle p_x^2 \rangle$.

Short injection When the injection persists shorter than π/ω_P then the first injected electrons have not completed a rotation of 180°, as shown in figure 3.10a. The phase space is not saturated. Thus, $\langle x^2 \rangle$ and $\langle p_x^2 \rangle$ can oscillate in the focusing channel. The further evolution depends on the length of injection and the energy spread.

The fast saturation of the first case makes it less complex than the second case. The transverse beam parameters can be considered as given by:

$$\epsilon_{\text{sat}} = \frac{1}{m_e c}\sqrt{\langle x^2\rangle\langle p_x^2\rangle}, \tag{3.34}$$

with a saturated emittance ϵ_{sat} [105]. A value for the saturated emittance in ionization-induced injections can be given by [105]:

$$\epsilon_{\text{sat}} = \frac{k_{\text{P}}}{2\sqrt{2}}\sigma_r^2, \tag{3.35}$$

where $k_{\text{P}} = 2\pi/\lambda_{\text{P}}$ is the plasma wavenumber and σ_r the beam radius.

In the case of a short injection, the saturation of the phase space can occur during the acceleration process. Michel et al. [98] and Mehrling et al. [99] provide an expression of the required propagation length of electrons for full decoherence:

$$L_{\text{dc}} = \frac{\pi c}{\omega_\beta}\left(\frac{\sigma_\gamma}{\langle\gamma\rangle}\right)^{-1}. \tag{3.36}$$

where $\sigma_\gamma/\langle\gamma\rangle$ is the relative energy spread of the injected bunch. However, L_{dc} can only provide a rough scaling for decoherence. Xu et al. [105] provided formulas to estimate the phase difference of electron slices injected at two different times. Ref. [105] used the following electron trajectories:

$$x(t) = x_0\left(\frac{\bar\gamma(t)}{\gamma_0}\right)^{-1/4}\cos\phi_\beta(t) \quad \text{and} \quad p(t) \approx \frac{x_0}{\sqrt{2}}(\gamma_0\bar\gamma(t))^{1/4}\sin\phi_\beta(t), \tag{3.37}$$

where $\bar\gamma = \langle\gamma\rangle$ is the average energy at the given time and $p(t)$ is approximated by the temporal derivation of $x(t)$. The emittance can be obtained from equation (3.31) by calculating $\langle x^2\rangle$, $\langle xp_x\rangle$ and $\langle p_x^2\rangle$ [105]:

$$\langle x^2\rangle(t) = \frac{\sigma_{x0}^2}{2}\left(\frac{\bar\gamma(t)}{\gamma_0}\right)^{-1/2}\left[1 + \frac{\sin 2\phi_M(t) - \sin 2\phi_m(t)}{2\phi_M(t) - 2\phi_m(t)}\right] \tag{3.38}$$

$$\langle p_x^2\rangle(t) = \frac{\sigma_{x0}^2}{4}\left(\bar\gamma(t)\gamma_0\right)^{1/2}\left[1 - \frac{\sin 2\phi_M(t) - \sin 2\phi_m(t)}{2\phi_M(t) - 2\phi_m(t)}\right] \tag{3.39}$$

$$\langle xp_x\rangle(t) = \frac{\sigma_{x0}^2}{4\sqrt{2}}\gamma_0^{1/2}\frac{\cos 2\phi_M(t) - \cos 2\phi_m(t)}{\phi_M(t) - \phi_m(t)}, \tag{3.40}$$

where $\sigma_{x0}^2 = \langle x_0^2\rangle$. ϕ_m and ϕ_M are the minimal and maximal betatron phase, respectively. The emittance from equation (3.31) can be rewritten as [105]:

$$\epsilon_{N,x}(\Delta\phi_\beta) = \epsilon_{\text{sat}}\sqrt{1 - \left(\frac{\sin\Delta\phi_\beta}{\Delta\phi_\beta}\right)^2}. \tag{3.41}$$

Thus, the emittance only depends on the phase difference $\Delta\phi_\beta = \phi_M - \phi_m$ between

the first and last injected electrons. Xu et al. provided a formula to calculate $\Delta\phi_\beta$:

$$\Delta\phi_\beta \approx \frac{\sqrt{2}}{E_{z,m}}\sqrt{E_{z,m}k_\mathrm{P}z_M + 1} - \frac{\sqrt{2}}{E_{z,M}}\sqrt{E_{z,M}k_\mathrm{P}z_m + 1}, \tag{3.42}$$

where z_m and z_M are the longitudinal coordinates of the ionization and $E_{z,m}$ and $E_{z,M}$ corresponds to the accelerating field E_z/E_0 inside the plasma cavity from chapter 2. From equations (3.36) and (3.42) one can deduce that a large energy spread or long injection can cause a large phase difference. A large difference in phase can lead to a faster saturation of the transverse phase space. In this case, the correlation term $\langle xp_x\rangle$ becomes negligible and equation (3.32) approaches:

$$\varepsilon_{N,x} \simeq \gamma\sigma_x\sigma_\Theta, \tag{3.43}$$

where $\sigma_x = \sqrt{\langle x^2\rangle}$ and $\sigma_\Theta = \sqrt{\langle\theta_x^2\rangle}$ are the beam radius and the geometric divergence, respectively.

The geometric divergence outside the LWFA is experimentally accessible by the non-dispersive plane of the electron spectrometer, as explained in section 4.3. The beam size can be deduced from the betatron radiation, as shown in section 5.2. Together, the two diagnostics can be used to study the dynamic of the transverse phase space as shown in section 6.1.

4. EXPERIMENTAL SETUP

This chapter concisely outlines technical details of the setup used for the experiments in chapters 5 and 6. Section 4.1 describes the experimental site at the ELBE center. The next section 4.2 gives a comprehensive overview of the DRACO high power laser system. Section 4.3 presents in detail the experimental setup for laser wakefield experiments. Finally, section 4.4 explains the utilized diagnostics for betatron radiation.

4.1. EXPERIMENTAL AREA

The experiments took place in a dedicated experimental area for high power lasers and relativistic electrons at the ELBE center. The ELBE center for High-Power Radiation Sources is a unique facility operating the conventional radio-frequency accelerator ELBE (**E**lectron **L**inac for beams with high **B**rilliance and low **E**mittance [106]), the dual beam high-power Ti:Sapphire laser DRACO (**Dr**esden l**a**ser a**c**celeration s**o**urce, see section 4.2) and the diode-pumped petawatt laser PEnELOPE (**P**etawatt, **En**ergy-**E**fficient **L**aser for **O**ptical **P**lasma **E**xperiments [107]). Figure 4.1 illustrates the layout of the building after it was commissioned in 2013. The zoomed-in figure presents the newly constructed part of the building with the experimental target area and the DRACO laser system.

The unique infrastructure of the electron target chamber enables operation with the electron beam from the ELBE accelerator, the DRACO 150 TW laser beam or a combination of both. Consequently, the vacuum chamber hosts two separate scientific setups: Thomson backscattering and LWFA. The setup and operation of the first is based on the previously developed x-ray source PHOENIX (**Pho**ton-**E**lectron collider for **N**arrow bandwidth **I**ntense **X**-rays [108, 109]) and was part of the Ph.D. thesis of Jakob Krämer [110]. The diagnostics for the LWFA setup were part of three theses. The broadband single-shot spectrometer for coherent transition radiation (CTR) for measuring the longitudinal bunch characteristics is part of the thesis of Omid Zarini [111]. The construction of the electron spectrometer was part of the thesis of Jurjen Couperus [43]. The betatron diagnostics for the transverse beam dynamics inside the plasma accelerator are part of this thesis and are described in section 4.4.

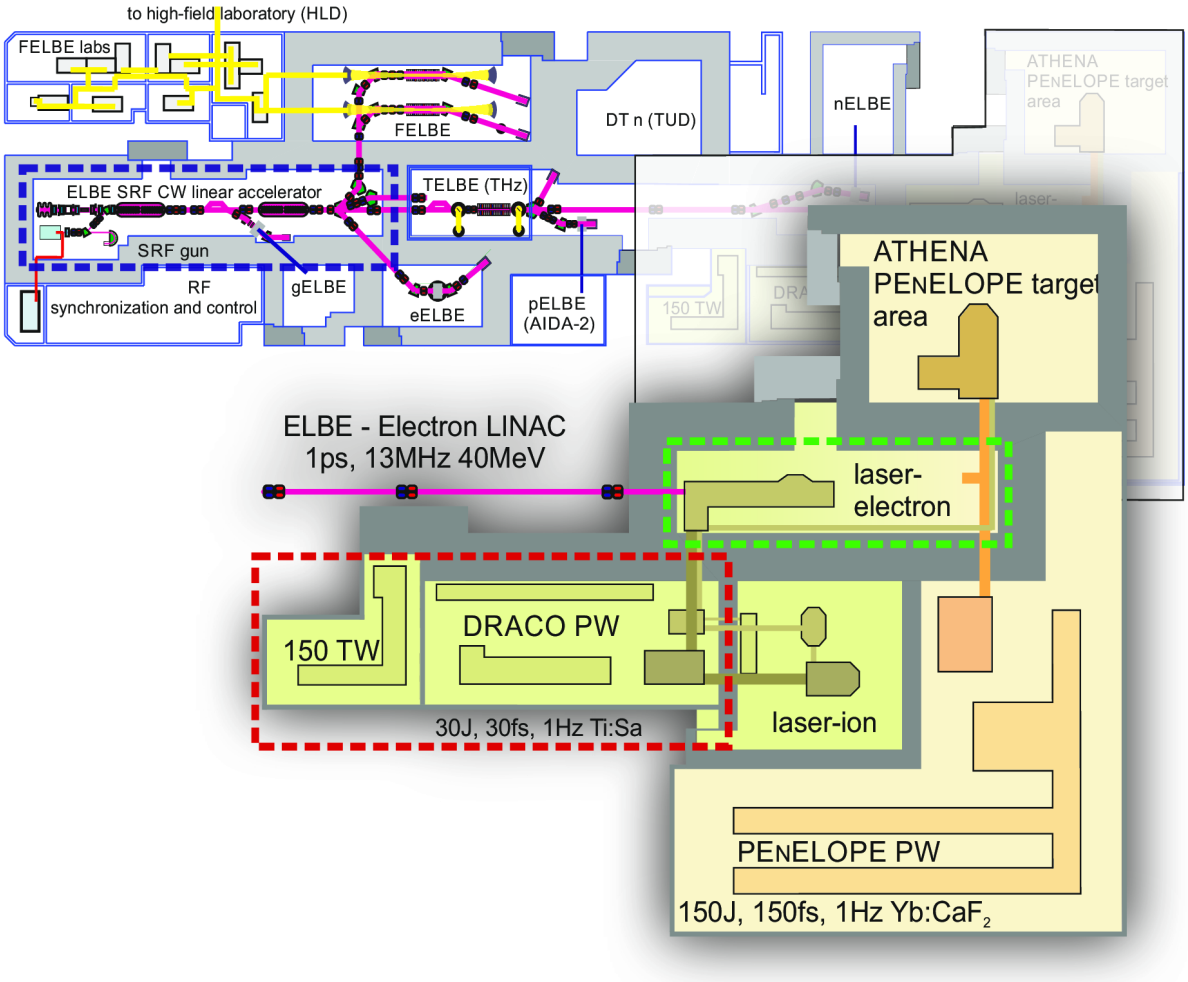

Figure 4.1.: **ELBE center for High-Power Radiation Sources:** The zoomed-in figure shows the part of the ELBE center with the experimental laser caves. The green and red dashed boxes indicate the target area for LWFA experiments and the DRACO laser system, respectively. In the background footprint, the blue dashed box indicates the conventional electron accelerator ELBE.

4.2. THE DRACO HIGH POWER LASER SYSTEM

Figure 4.2 schematically presents the DRACO laser system [11] used in this thesis. The requirements considering pulse energy and duration as described in chapter 2 are readily fulfilled by the 150 TW arm.

The DRACO laser system utilizes double-chirped pulse amplification (CPA) [112] to reach high power laser pulses with high temporal contrast. CPA enables amplification of laser pulses by temporally stretching them before amplification. Thus, the peak power is reduced below the damage threshold of the optical components and amplifying crystals while maintaining a compact setup size of the laser. In the final step of the laser chain, the pulse is temporally compressed to reach the desired short pulse duration.

The DRACO laser system was recently upgraded to a dual beam system with a Petawatt arm and a 150 TW arm that can provide 30 fs-short pulses with 30 J and 4.5 J on target, respectively. The pulses possess an optimized temporal contrast and high beam quality [11]. Titanium-doped sapphire (Ti:Sa) crystals are used as the gain medium with a central wavelength of 800 nm and up to 80 nm pulse bandwidth.

At the starting stage of the laser chain is a commercial Femtolasers oscillator delivering 10 fs to 15 fs pulses at 800 nm with a spectral width above 190 nm (FWHM) and a few nanojoules of energy. The 78 MHz repetition rate of the oscillator is reduced to 10 Hz by a Pockels cell (PC) pulse picker. The laser pulse energy is amplified to the microjoule level by the booster amplifier and is then fed to the first CPA stage. There, the pulses are stretched to 500 ps by a reflective stretcher, their spectral phase is fine-tuned by an acousto-optic programmable dispersive filter (Dazzler-Fastlite) and their energy is amplified in a regenerative amplifier (0.5 mJ) and a multipass amplifier (25 mJ). In the regenerative amplifier, fine control of the spectral gain is achieved by an acousto-optic programmable gain filter (Mazzler-Fastlite) which can reduce the transmission of spectral regions with high-gain.

After amplification, an air compressor compresses the pulse to 30 fs in order to reach a proper intensity to optimize the temporal contrast by cross-polarized wave (XPW) pulse cleaning. The cleaning process reduces the pulse energy to 0.3 mJ. Similar to the first CPA stage, the second CPA stage stretches and amplifies the laser pulse. Additionally, two more multipass amplifiers boost the pulse energy to 1.5 J which is the output of the laser front end. At this point, the pulses can be split into the petawatt and the 150 TW arm which can operate in parallel, inherently synchronized or individually.

Only seeded on demand by a PC pulse picker, the last multipass amplifier of the 150 TW arm reaches a pulse energy of up to 6 J. The crystal of the last amplifier is cryogenically cooled to avoid thermal lensing caused by the thermal load. After the last multipass amplifier, the beam is expanded to the final beam size of 100 mm and coupled into the vacuum compressor where the pulse is compressed to a length of 30 fs. From this point, the beam has to be transported in a vacuum, because the laser field after the compression becomes high enough to cause ionization in air and filamentation [113]. A closed feedback loop consisting of a deformable mirror and a wavefront sensor (Phasics SID4) in the LWFA target area allows wavefront optimization to obtain the diffraction limited focal spot at the plasma target. The DRACO laser beam can be directed either to the electron target area or the ion acceleration area, as shown in figure 4.1.

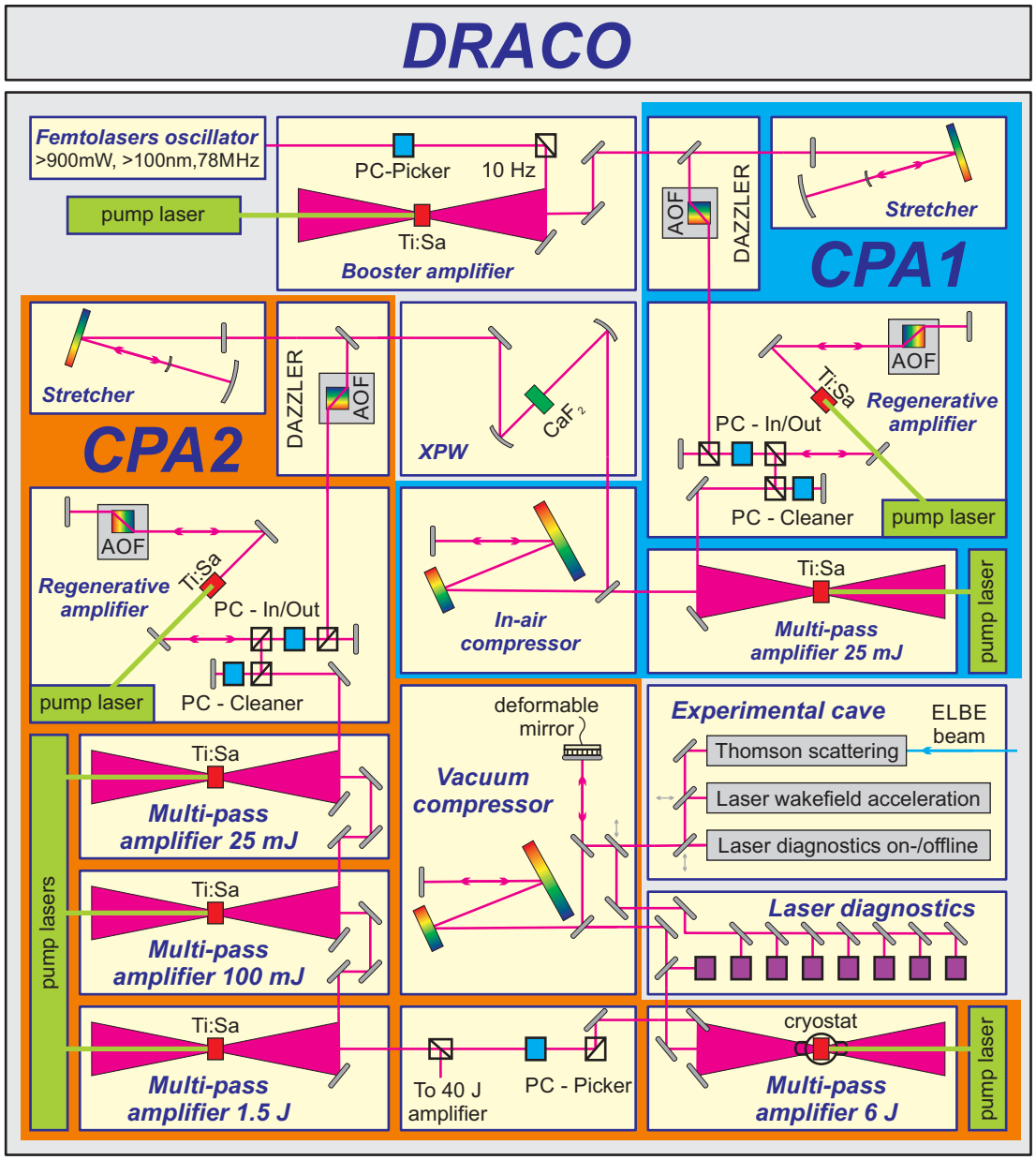

Figure 4.2.: Schematic layout of the DRACO (Dresden laser acceleration source) front-end and the 150 TW arm.

4.3. EXPERIMENTAL SETUP

A vacuum beam transport line connects the DRACO compressor chamber of the 150 TW arm and the 5.6 m long experimental chamber. Three turbomolecular pumps maintain a vacuum condition of $\sim 1 \times 10^{-6}$ mbar during the experiments. The optical breadboard for the experimental equipment is decoupled from the frame of the chamber in order to avoid pump vibrations and deformations from pressure differences.

Figure 4.3 schematically presents the setup for LWFA experiments. The setup for Thomson backscattering experiments is not shown. A look inside the vacuum chamber on the LWFA target area is illustrated by figure 4.4. An f/20 off-axis parabola (OAP) focuses the DRACO laser beam about 1.5 mm above the gas-jet target. The laser profile and the density profile of the gas-jet are discussed in the following subsections. The leakage through the folding mirror after the OAP is used for online single-shot diagnostics.

Experiments are prepared by driving a mirror into the beam path and reflecting the laser pulse to offline diagnostics. Reflection over several uncoated, high surface quality wedges attenuates the laser intensity to avoid damages to sensitive equipment, i.e., cameras. The focal spot of the OAP is imaged by a high-quality objective (TSO apochromat f77) onto a wavefront sensor (PHASICS SID4). The objective with an aperture of 50 mm has a 24× magnification. The resolution specified by the manufacturer is 1.6 µm. A closed loop with the deformable mirror in the DRACO compressor chamber then optimizes the wavefront and corrects distortions. Additionally, the focus can be imaged on a CCD (charge coupled device) camera and can be manually optimized.

Further offline diagnostics, such as a self-referenced spectral interferometer (WIZZLER-Fastlite) and a spectral-phase interferometer (SPIDER-A.P.E.), can be switched on by moving in a mirror in front of the objective. The stability of the laser pulse length can be observed offline as well as online by a single shot second order vacuum autocorrelator. A movable pick-up mirror enables the autocorrelator to be used during the LPA experiments. Additionally, the stability of the near- and far-field is monitored by using the low transmission ($\leq 1\%$) of the laser pulse through the folding mirror after the OAP.

For transverse probing, the plasma channel is exposed with the probe beam and is imaged to a 12 bit CCD camera (AVT GT 1600) by a microscope objective (TSO apochromat f100). The objective has a 20× magnification with an aperture of 50 mm and the resolution specified by the manufacturer is 2.3 µm. The probe beam is picked off from the main laser beam and a delay line is used to adjust the delay between the probe and main beam. This provides the possibility to tune the probed time. The temporal resolution is limited by the pulse length of the main laser pulse which is typically 30 fs.

The laser beam after the focus is monitored by the exit mode diagnostics, which uses high-quality wedges for intensity attenuation. It allows positioning of the focus onto the LWFA target in the experiment preparation phase. During the experimental runs, the transmitted laser light and the laser mode at the plasma exit can be identified.

The electron spectrometer behind the gas-jet target diagnoses the charge, energy

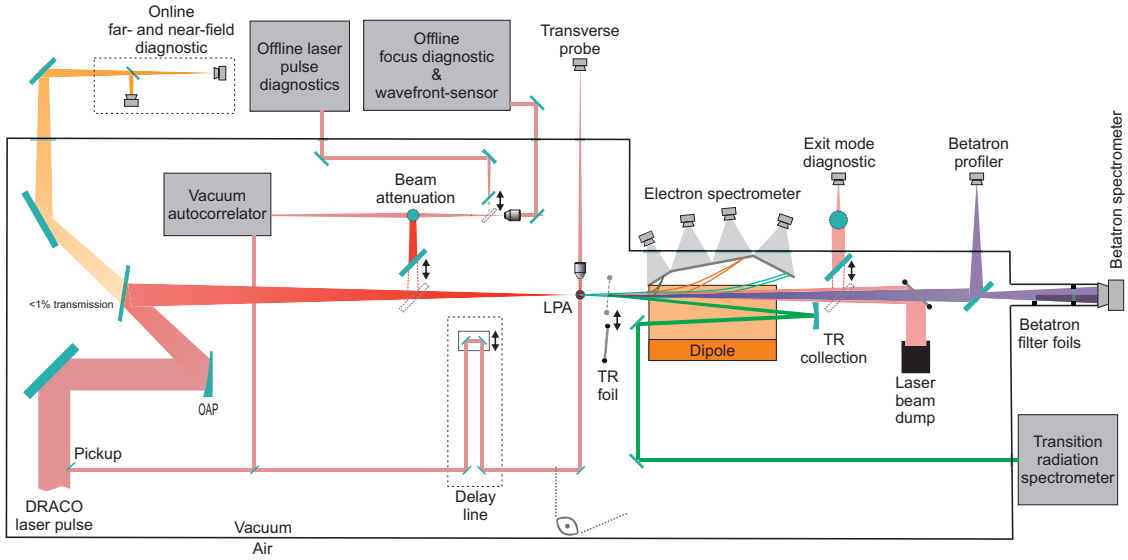

Figure 4.3.: **LWFA setup:** The setup used for the LWFA experiments and betatron radiation. The eye symbol points to the field of view in figure 4.4.

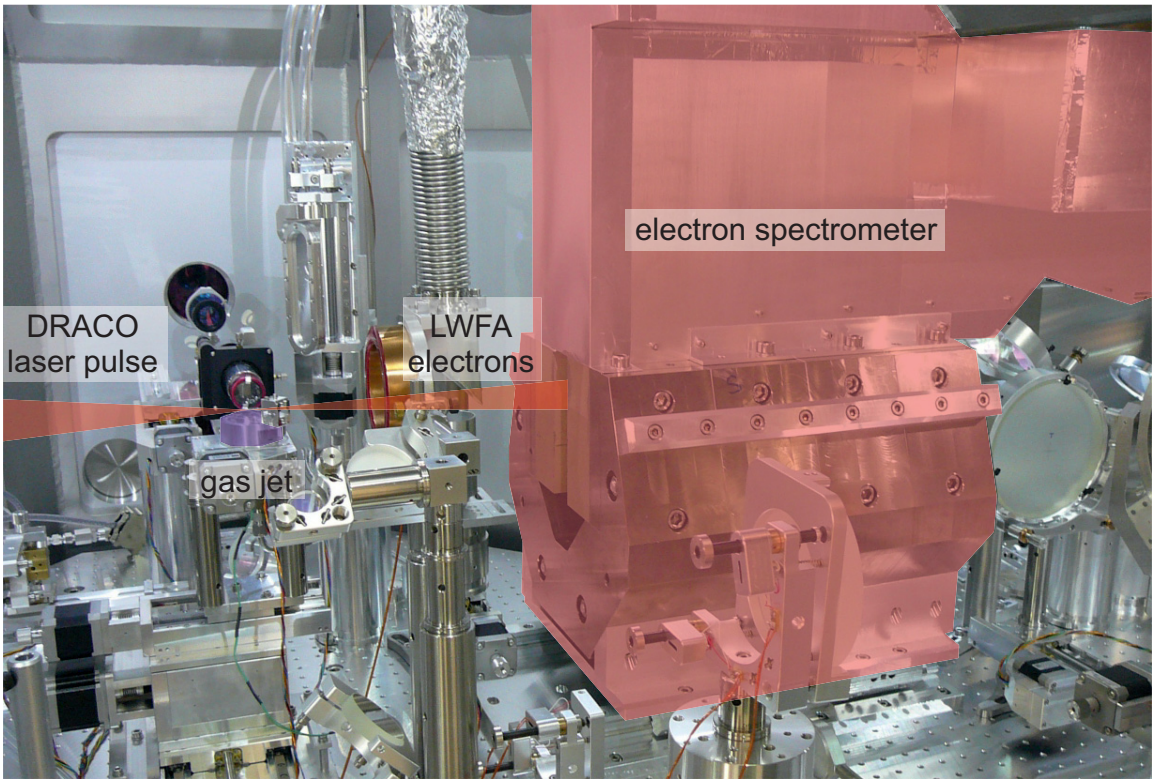

Figure 4.4.: **Look inside the vacuum chamber onto the target:** The field of view is marked by the eye symbol in figure 4.3.

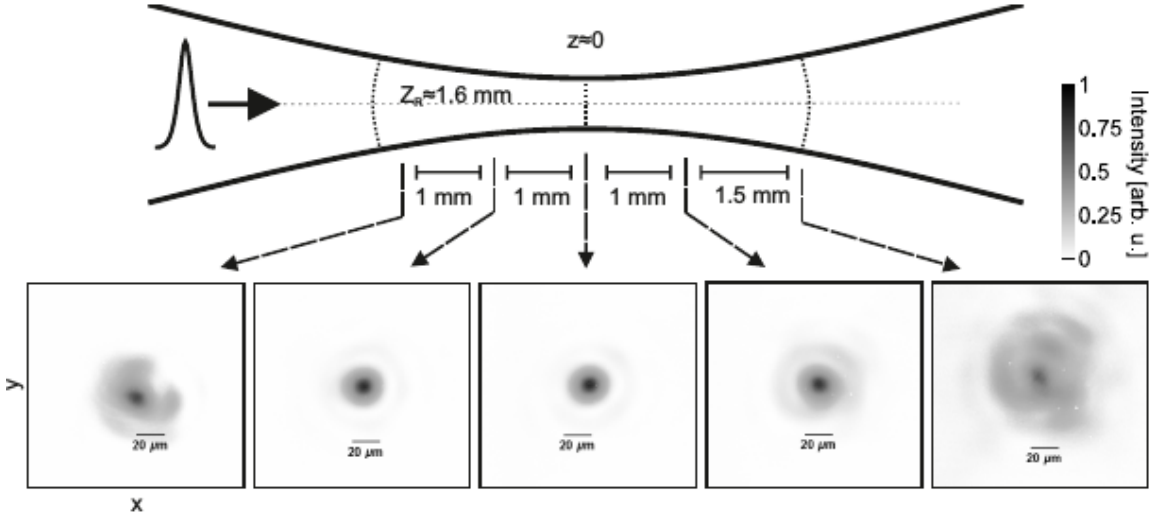

Figure 4.5.: **Laser profile near the focus:** A spot size of 20 µm (FWHM) is reached at the focus (z = 0). The beam waist (at e^{-2} of peak intensity) contains ∼76 % of the laser energy, which corresponds to a Strehl-ratio of 0.9. The laser profiles were acquired after phase optimization by utilizing an acousto-optic programmable dispersive filter (DAZZLER-Fastlite) in closed-loop and while running the laser system under experimental conditions (all amplifiers fully pumped). From Couperus [43].

and divergence in the nondispersive plane of the magnetic field. The permanent magnetic dipole of the spectrometer disperses electrons with an energy up to 550 MeV and is discussed in more details below.

Removing the exit mode diagnostics from the beamline enables two other LPA diagnostics: The transition radiation diagnostic and betatron diagnostic. The first investigates the electron beam parameters after the plasma-vacuum transition and is further discussed in section 4.3.4. The latter utilizes the x-ray radiation from the electrons at the end of the acceleration to access the transverse dynamic inside the plasma. The x-ray diagnostic is part of this thesis and explained in detail in section 4.4.

4.3.1. LASER BEAM PROFILE

Since the successful operation requires the interaction of the laser pulse with the target to start before the focus, a high-quality laser beam profile is essential for the experiments. The far-field and the intermediate field before the focus should have a well-defined beam profile which is preferably symmetric around the beam axis and contains as much energy as possible near the center. With the previously shown setup, a scan of the far and intermediate field is possible with the laser system operating at full power. Figure 4.5 presents the evolution of the laser profile in vacuum. The wavefront is optimized using a wavefront sensor (PHASICS SID4) running in closed-loop with a deformable mirror. A focal spot size of 20 µm (FWHM) is reached by the OAP in vacuum. About 76 % of the laser energy is contained within the beam waist (e^{-2} of peak intensity). The focal spot has a Strehl-ratio of 0.9. At the beam center, a Gaussian profile is maintained over the scanned range while the energy fraction

(a) Used nozzle mounted on Parker 9-series valve.

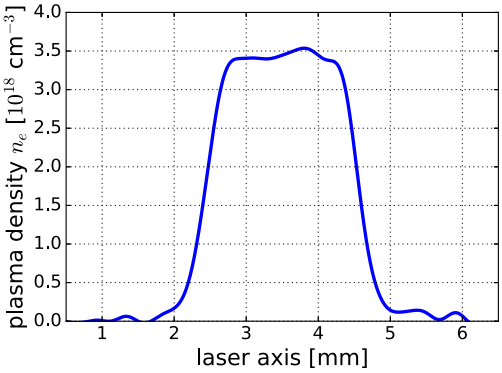

(b) Density profile along the laser axis.

Figure 4.6.: **LPA target:** (a) shows a photo of the used nozzle after the experiment. (b) represents the profile provided by a 3 mm supersonic nozzle with a de Laval shaped nozzle waist.

decreases below 60 %. The missing fraction of beam energy can be attributed to the outer fringes visible in the figure. The fringes can have a significant effect on the focus evolution in the plasma, as shown in section 6.2.1.

4.3.2. GAS JET TARGET

Besides a high power laser, the essential ingredient of an LPA is the medium which provides the plasma for the acceleration. The density profile of the plasma medium together with the laser pulse define the possible LPA setups and ability to obtain accelerated electrons. Different types of targets have been developed so far for this reason [114].

Gas cells, discharge capillaries and gas jets are the main targets used for LWFA [16]. Well-established targets that are turbulence-free in operation are gas cells. In the most simple design, a cell with two gas exits aligned along the beam axis is homogeneously filled with gas. The exits can act as little apertures for the laser pulse and typically restrict in many cases the possible laser settings, such as focus position and spot size. More advanced targets are discharge capillaries, where the gas-filled volume is restricted to a narrow capillary. Applying a voltage of tens of kilovolts at the capillary exits creates an electrical discharge. The discharge can be utilized to form a parabolic plasma channel profile before the laser arrives. When transverse plasma profile and laser beam size are matched, then the laser pulse is guided over several centimeters [50] as explained in section 2.3.

The main disadvantage of a gas cell or capillary is the closed design. Transverse probing is challenging because it requires surfaces of high optical quality. Laser ablation at the surface material and discharge contamination degrade the quality over several shots. Additionally, the gas exits are apertures and are sensitive to pointing

fluctuations and misalignment of the laser. When the laser pulse is not guided but hits the gas cell or capillary body, then the high pulse energy can damage the target. Gas jets offer a more open design and a lot more diagnostic possibilities. They grant full access from almost all sides except from the nozzle outlet. The open design comes at the expense of active guiding. Nevertheless, relativistic self-focusing can guide a high intensity laser pulse in gas jets as discussed in section 2.3.

The laser-wakefield target used for the experiments presented here was a gas jet made up of a supersonic de Laval nozzle [115] with Mach 10.4. The density profile was characterized before the experiments with a dedicated interferometry setup [116]. A tomographic method reconstructed the density profile [12, 16] of the gas jet. The nozzle and the density profile along the laser axis are presented in figure 4.6. During the LWFA experiments, the nozzle was operated with different He-N_2 gas mixtures with 0.2 vol – % to 1.5 vol – % of N_2. The mixtures deployed from premixed bottles had less than 2 % relative error.

4.3.3. ELECTRON SPECTROMETER

An integral part of LWFA diagnostics is the electron spectrometer, which enables measurement of the beam quality of the accelerated electrons, charge, electron energy, energy spread and divergence with pointing on the non-dispersive axis. The electron spectrometer used during the experiments and explained here was implemented by Jurjen Couperus as part of his Ph.D. thesis [43].

MAGNETIC FIELD MAP

The basic structure of the electron spectrometer is made up of four 10 cm × 15 cm dipole magnet sections. Each section includes six permanent magnets (VACODYM 754TP [117]) which are fixed on an iron yoke. The free pole gap measures 40 mm in width and is designed for a field strength of ∼1 T.

Deviations from the design field strength due to imperfections in construction alter the accuracy of the electron spectrometer. In order to consider this, the field was mapped in a three-dimensional, 2 mm grid using a Hall probe (Lakeshore MMTB-6J04-VG). Figure 4.7 presents the result. The maximum field strength of 0.9 T is reached inside the magnet, which is in good agreement with the design value. Fringe fields outside the physical borders of the magnetic dipole are visible. The field is not entirely uniform between the poles but varies periodically. The variation can be attributed to single magnets from different dipole sections.

The basic principle of the operation of an electron spectrometer is the deflection of electrons by the Lorentz force. A moving electron inside a magnetic field B experiences the Lorentz force to be perpendicular to its momentum p and the field. The electron's path follows an orbit with radius ρ, which is given by the cyclotron equation:

$$\rho[\mathrm{m}] = \frac{p[\mathrm{GeV/c}]}{0.2998 B[\mathrm{T}]}, \tag{4.1}$$

where ρ is also known as the cyclotron or Larmor radius. The momentum and thus energy dependency of the radius disperses electrons perpendicular to the magnetic

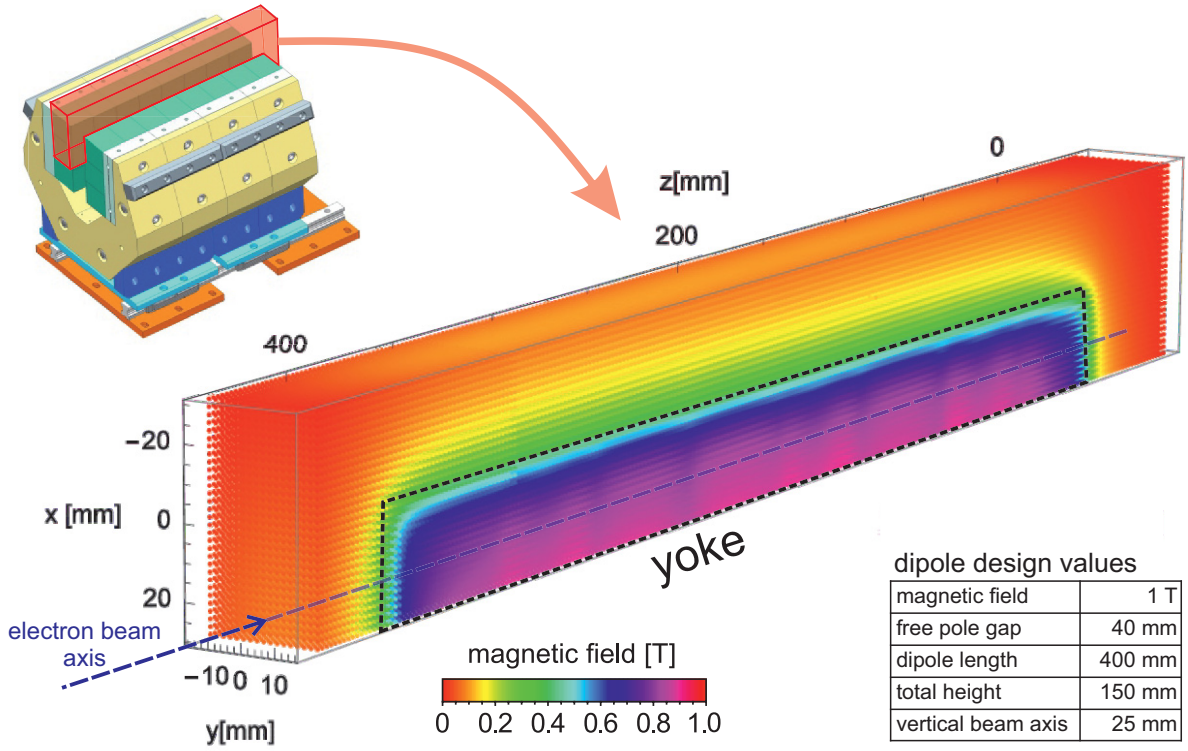

(a) 3D field map of the upper half of the magnetic dipole.

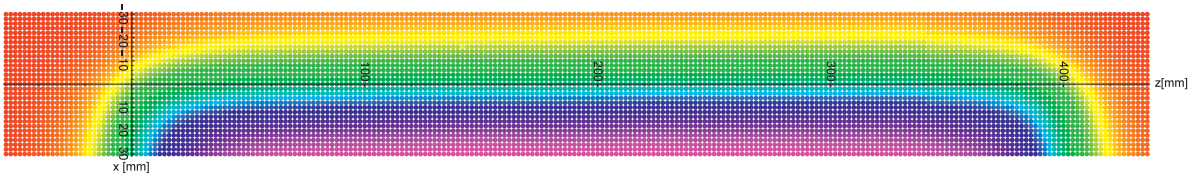

(b) Two-dimensional field map in the *x*-*z* plane through the middle ($y = 0$ mm).

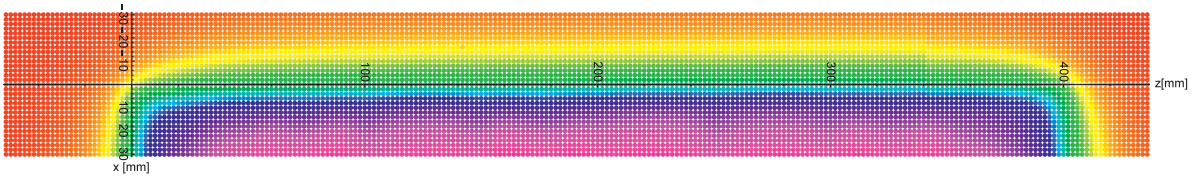

(c) Two-dimensional field map in the *x*-*z* plane at $y = 14$ mm.

Figure 4.7.: **Electron spectrometer:** A three-dimensional representation of the magnetic dipole and the measured magnetic field is shown in (a). The measured field strength is sampled on a grid with a resolution of 2 mm. The black dashed line marks the area of the yoke. The top edge of the dipole starts at $x = 0$ mm and the sides are at $z = 0$ mm and $z = 400$ mm. The pole gap is 40 mm wide. The electron beam axis is at $x = 25$ mm and $y = 0$ mm. A slice of the magnetic field in the *x*-*z* plane through the middle of the gap and close to the pole at $y = 14$ mm is presented in (b) and (c), respectively.

field of the dipole. For example, an electron with a momentum of 10 MeV/c is following an orbit with a radius of 3.3 cm in a magnetic field of 1 T while an electron with 500 MeV/c has a larger radius of 1.7 m.

PARTICLE TRACING AND ENERGY CALIBRATION

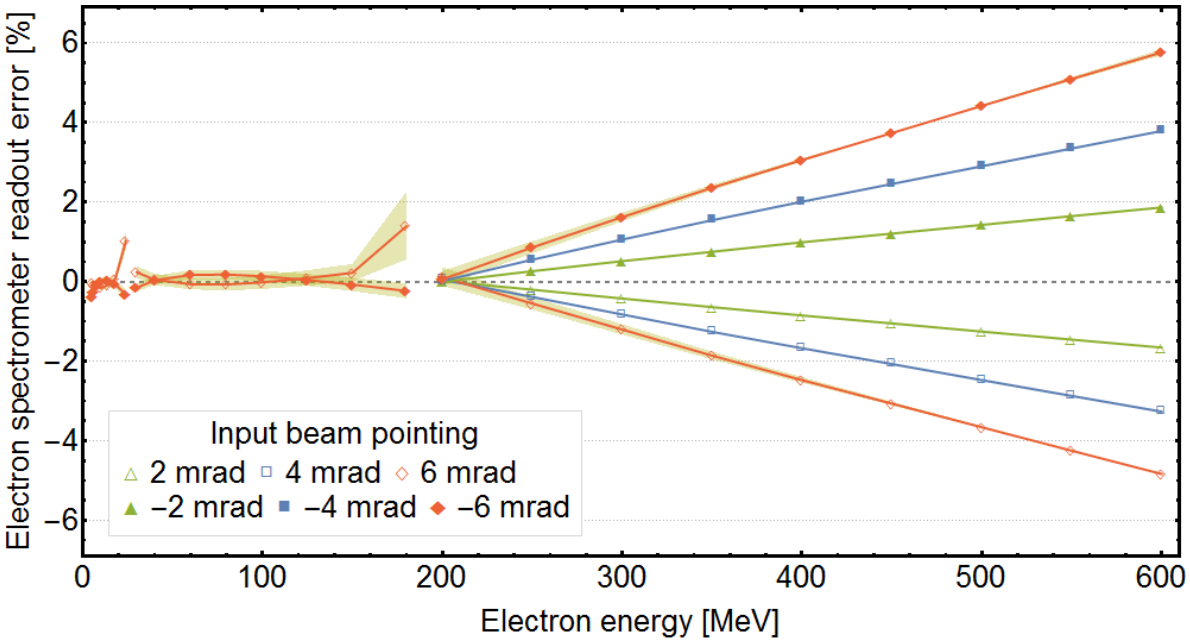

Figure 4.8.: **Readout error of the electron spectrometer:** Different pointings of the input beam result in readout errors. The values indicate a divergence or pointing of the beam in the bending plane. The impact of vertical positioning errors (±0.2 mm) is illustrated by the shaded areas.
Figure from [11].

The cyclotron equation is only a very rough scaling for the electron trajectories inside the electron spectrometer. A more accurate method utilizes the measured field map and a particle tracing program to predict the electron trajectories. For this purpose, simulations with the General Particle Tracer (GPT) code [118] were set up. Test particles with different initial momentum from a virtual particle accelerator were introduced. For each momentum, three particles were created with three different pointings. One particle with zero pointing followed the reference trajectory. The two other particles represented a beam divergence of ±6 mrad. That allowed us studying the focusing effect from the fringe fields of the dipole.

Same electron energies with different pointings are focused at the same position behind the dipole. At the focus points, scintillator screens are positioned to record the energy spectrum. Two separate screens were mounted to cover an energy range from 5 MeV to 200 MeV. This provides proper one-to-one imaging of the electron beam and avoids bending of the scintillator screens. The third screen which covers energies from 200 MeV to 600 MeV cannot be placed directly at the optimum position because of the size of the vacuum chamber. Therefore, it is placed in front of the

electron focus point while introducing a maximum relative error of 6 % on the energy readout.

Bending of the flat screens has to be avoided in order to maintain the scintillation ability. The straight scintillator screens introduce a small error of less than 2 % for energies lower than 200 MeV. An error of ±0.2 mm in the vertical position of the LWFA causes the electrons to travel different distances inside the magnetic field. The absolute angle of the orbit changes and consequently the position on the screen. Fluctuation in vertical position is the dominant error on the two low energy screens. The angular pointing error dominates for energies above 200 MeV. Figure 4.8 summarizes the resulting errors in the energy resolution. The error in the horizontal position was investigated and found to be negligible for offsets smaller than 1 mm due to the large imaging distances.

SCREEN IMAGING AND CHARGE CALIBRATION

The three scintillator screens together measure more than 650 mm in length and are mounted at three different angles. This requires four CCD cameras (Basler acA-1300-30gm) to image the entire range. The next paragraph describes how a relative charge calibration of the electron spectrometer is obtained.

Perspective distortions caused by the large imaging angle are compensated by transforming the camera images. The realigned and corrected images are then stitched together to a single virtual screen. Since the electrons hit the screens at an angle $\phi \neq 0$, the interaction length and thus the energy deposition in the scintillator is different. The influence of the non-perpendicular interaction is corrected by applying a correction factor $1/\cos(\phi)$ with angles recovered from the GPT simulations. A second correction factor rectifies the influence of different viewing angles from the cameras. As the last step, the screen is translated into the energy, where the correlation found by GPT particle tracing is utilized.

The relative charge calibration can be extended to an absolute charge calibration. Buck et al. [119] published an absolute charge calibration of several commercial screens. However, the conditions for this calibration were different from typical LPA experiments as discussed by Kurz et al. [8]. For this work, the calibration results obtained from ref. [8] were used.

4.3.4. TRANSITION RADIATION DIAGNOSTIC

Measurement of the ultrashort bunch duration from LWFA is a challenging task [120]. One promising technique is measuring the coherent transition radiation (CTR) spectra and extracting the bunch length and the longitudinal bunch profile [5, 121]. Transition radiation (TR) is generated when relativistic electrons traverse the interface between two different dielectric mediums due to the rapid change in the phase velocity of electromagnetic waves. Radiation wavelengths that are longer than the bunch length are emitted coherently, where the emitted power is proportional to the square of the number of electrons. For shorter wavelengths, the emission is incoherent and the power is proportional to the number of electrons.

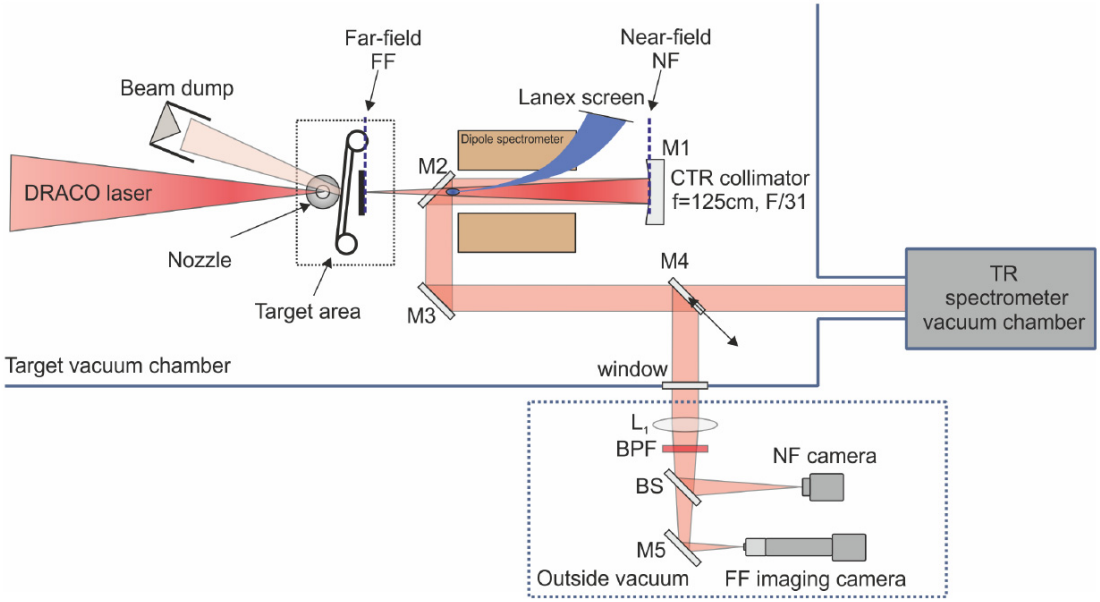

Figure 4.9.: **Schematic of the transition radiation setup:** The electron bunch (blue) originating from the plasma target passes a set of foils and enters the electron spectrometer. The first foil reflects the transmitted laser light to a beam dump. The CTR light from the back of the last foil is collected by an f/31 parabola and collimated into the TR spectrometer.
Figure from Zarini [111].

For measuring TR, a broadband single shot spectrometer was implemented by Omid Zarini for his Ph.D. project [111, 122]. The spectrometer covers a broad range of wavelengths from 200 nm to 12 µm. The CTR diagnostic is connected to the LWFA setup as shown in figure 4.9.

TR is generated in the setup by inserting a set of foils ∼20 mm close to the plasma exit. The first two foils are on a tape drive and are moved with every shot. The first foil reflects the transmitted laser light to a beam dump. The second tape foil acts as a debris shield for the third foil which is used for generating TR. The TR foil is placed perpendicular to the beam axis and (26 ± 1) mm from the plasma exit. The transition radiation from the surface of the foil is collected by the spherical mirror M1 with a focal length of 1.25 m.

M1 collimates the TR beam as required by the spectrometer setup. Several aluminum-coated folding mirrors (simplified by M2 and M3) direct the beam to the CTR spectrometer. For studying the transverse TR profile, the motorized mirror M4 can be moved into the TR beamline and reflect the beam to the profile diagnostics in air. Different wavelengths can be selected by several bandpass filters (BPF) that are mounted on a motorized filter wheel. Finally, the beam splitter BS divides the beam for simultaneously imaging the near- and far-field of the TR profile.

For prealignment of the TR beamline, the target chamber and the CTR vacuum chamber can be separated by a vacuum valve with an embedded window, which allows independent evacuation of both chambers. The precise alignment of the spectrometer is crucial for accurate CTR measurements [111]. The pumping down shifts

the chambers relative to each other and typically introduces a deviation from the pre-alignment performed in air.

4.4. X-RAY DIAGNOSTICS

X-ray photons with energies from 1 keV to 100 keV can interact in different ways with electrons in solid matter. As an example, figure 4.10 shows the cross sections for different scattering processes in silicon. The cross section is defined by the probability for a scattering process to take place. Silicon is a possible bulk material for CCD cameras.

The figure 4.10 indicates the typical trends for the interaction of x-ray photons with matter. The total cross section decreases exponentially with increasing energy. Thus, the detector material for energy deposition have to be thicker for higher energies in order to maintain an adequate detection of the photons. The photoelectric effect is dominating in the lower energy range, while Compton scattering is more pronounced for higher x-ray energies above hundreds of keV. Elastic scattering of photons with free and unbound electrons provides a background signal.

The broadband nature of betatron radiation results in the emission of x-rays and gamma rays, as shown in chapter 3. While betatron diagnostics typically record photons with an energy less than 100 keV, gamma photons with energies of ∼1 MeV have also been observed [123]. As mentioned before, the typical cross section for photons with energies in the MeV range is small and dominated by Compton scattering. Thus, calorimetric detectors [124] or spectrometers utilizing Compton scattered electrons [125] can be deployed. In recent years, detector development has evolved with considerable success and can enhance the betatron diagnostics in the near future. However, most of the betatron photons typically have an energy ∼10 keV and silicon-based pixel detectors can cover photon energies up to 30 keV. Hence, they are deployed in the following to acquire the betatron spectrum.

4.4.1. BETATRON SPECTROMETER

Two directly illuminated x-ray CCD cameras were used for the experiments presented in this work. Standard CCDs are illuminated from the front. In this case, the photons have to pass through an inactive layer of electrical connections, which absorbs photons of short wavelengths. The deployed CCDs are illuminated on the backside of the chip in order to increase the sensitivity for shorter wavelengths. Both cameras were attached to vacuum chambers that supported a pressure below 1×10^{-6} mbar. The vacuum enabled the CCDs to be cooled down in order to reduce the thermal noise during the experiments. Figure 4.11 shows the two cameras without attached instrumentation.

The first used detector was an Andor DO 934N-DN. The CCD chip had 1024×1024 pixels and a total size of 13.3 mm × 13.3 mm. The small pixel size of 13 µm × 13 µm facilitates imaging of objects with x-ray radiation, where a high spatial resolution is required. The camera was installed at 5.7 m from the target and placed in a separate lead shielded area. It was connected to a dedicated vacuum chamber. The x-ray

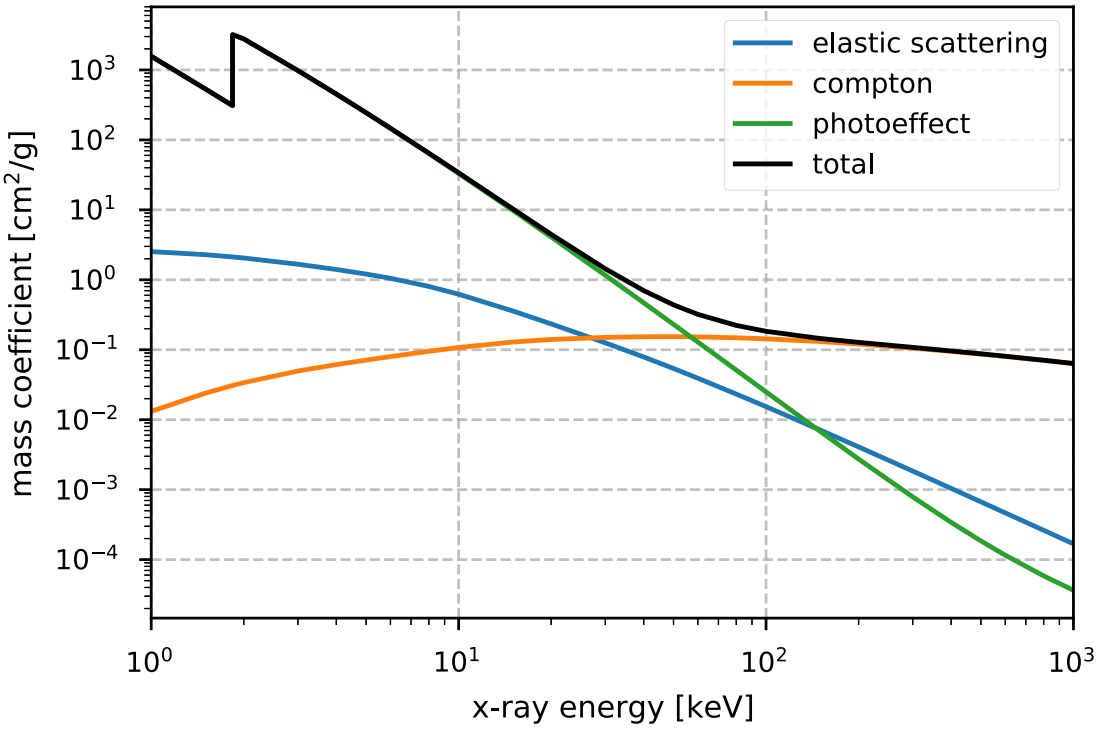

Figure 4.10.: **Cross sections for different photon energies in silicon:** Photons in the keV-range interact with solid matter in different ways. The different cross sections of x-ray photons in silicon are presented as an example.

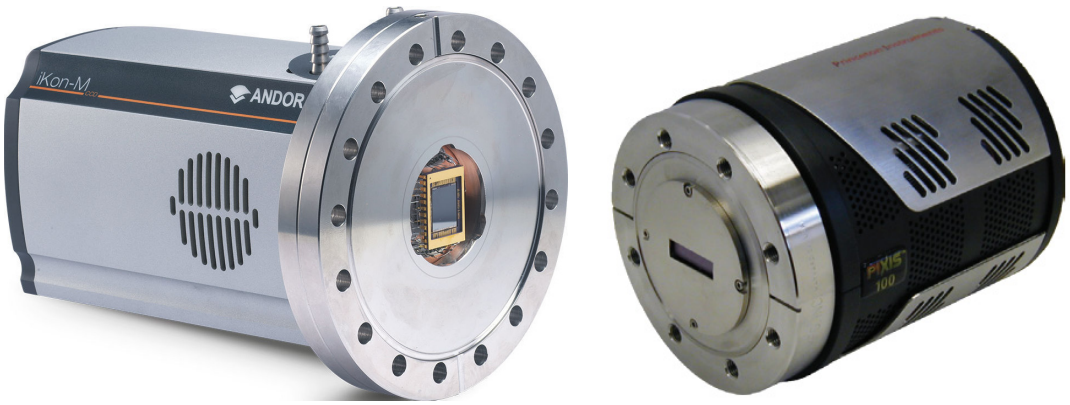

(a) Andor DO 934N-DN. (b) Pixis-XO 400BR.

Figure 4.11.: **The deployed x-ray CCD cameras:** (a) is the Andor-DO and (b) is the Pixis-XO. Both x-ray cameras use silicon CCD chips which are illuminated from the back.

(a) Lead shielding of Pixis camera. (b) Betatron beamline.

Figure 4.12.: **Betatron spectrometer and beamline:** The Pixis is placed in a separate radiation shielded area as shown in (a).
As shown in (b), the 12 m betatron beamline (yellow) connects the main vacuum chamber and the Pixis chamber.

window of the Andor camera consisted of a 75 µm Kapton foil to sustain the pressure difference between air and vacuum and a 14 µm Pokalon foil for light absorption. The x-ray window of the target chamber was a 125 µm thick Kapton foil. A 2.5 m long evacuated tube with 75 µm Kapton windows was inserted between both chambers in order to minimize transmission losses in air. The air gaps between the tube and the vacuum chambers were in total 200 mm.

In order to increase the sensitivity of the x-ray diagnostic and facilitate single photon counting techniques [7, 13, 108], a Pixis-XO 400BR from Princeton Instruments was deployed. The pixel size of 20 µm × 20 µm was larger than for the Andor. Additionally, the chip was deep-depleted, which increased the sensitivity at higher x-ray energies. The 1340×400 pixel occupied an area of 26.8 mm × 8.0 mm. The detector was placed at 5.7 m and 11.7 m distance from the source.

The target chamber and the x-ray CCD chamber were mechanically connected by a beamline. Both vacuums were isolated by a 76 µm thick high purity beryllium window (Materion IF-1 [126]) with a free aperture of 12.7 mm. Figure 4.12 presents the radiation housing of the Pixis and the up to 12 m long beamline between the target chamber and x-ray camera.

SINGLE PHOTON ABSORPTION

The two x-ray cameras deploy silicon as the detection material. In silicon, photons with energies up to 60 keV are predominantly absorbed via the photoelectric effect, as shown in figure 4.10. In this case, a photon ionizes an atom, when the photon energy exceeds the binding energy of an electron. Photo-ionization of inner shells, e.g., K-shell, is typically more likely than for outer shells [46]. When the photon is absorbed, an energetic photoelectron and an excited ion with a core vacancy are created. The excited ion deexcites by fluorescent radiation as a higher-lying electron falls into the vacancy with the emission of an x-ray of characteristic energy. Alterna-

tively, the energy freed by the transition is converted to an Auger electron. An Auger electron is an outer shell electron which carries the transition energy away from the ion. The energetic photoelectron can ionize other atoms. The thermalization of the ejected electrons shifts electrons to the conduction band of the semiconductor and forms a microscopic charge cloud around the initially hit atom [29, 46]. The number of electrons N_{cc} in the charge cloud is proportional to the absorbed x-ray energy E_x, i.e., $N_{cc} = E_x/E_g$ with $E_g = 3.6\,\text{eV}$. E_g is the required energy for the creation of an electron-hole pair in silicon [29].

An applied voltage causes electrons in the potential well of each pixel on a CCD chip to be collected. Subsequently, the read-out, amplification and digitization into analog-to-digital-units return a value N_{ADU} proportional to the collected charge in the potential well. When all electrons related to the x-ray absorption are contained within one pixel, then N_{ADU} is proportional to the energy of the absorbed photon. Although diffusion can cause the charge cloud to be larger than the potential well, resulting in an incomplete collection of charge. This can be countered with larger pixel sizes.

A CCD with millions of pixels can be considered as millions of simultaneously operating x-ray detectors. A simple histogram of the pixels can reconstruct an energy-resolved spectrum, when the flux is low enough that every pixel is either hit or not by exactly one photon. In this case, the detectors are fully independent and number of pixels hit by a photon is equal to the number of detected absorption events. In reality, the charge can also be split over two or more adjacent pixels or two photons can hit the same pixel or adjacent pixels and distribute charge over several pixels. In this case, the detectors are not independent. To take this into account, an algorithm was implemented which selects only isolated absorption events and corrects for the spectral pile-up (see appendix A).

DETECTION EFFICIENCY FOR DIFFERENT FLUXES

The typical high flux of betatron sources can cause a degradation of the detection algorithm. For example, on a CCD with all pixels hit by one or more photon, a single photon may not be detected. The impact of different high fluxes on the detection efficiency is represented in figure 4.13. The detection efficiency is defined as the number of detected events divided by the total pixel number. The algorithm distinguishes two detectable events: A single-pixel (SP) event is precisely one pixel with charge and all eight adjacent pixels have no charge. The second event allows the adjacent eight pixels to have charge in a multi pixel (MP) event, only if all sixteen neighboring pixels do not have charge.

The highest detection efficiency is visible for SP, MP and SP+MP events. The detection algorithm saturates at this rate and deteriorates toward higher fluxes. The saturation means that the same number of events is detected even when more photons are absorbed by the detector material. The deterioration occurs when the detection algorithm fails because more adjacent pixels are hit by photons. In this case, SP and MP events become less frequent. SP events occupy only one pixel while an MP event occupies at least two pixels. Thus, the maximum detection rate for MP is already at $\sim$6 % of illuminated pixels than for SP which is at $\sim$15 %.

The maximum detected events including SP and MP events is reached when $\approx$8 %

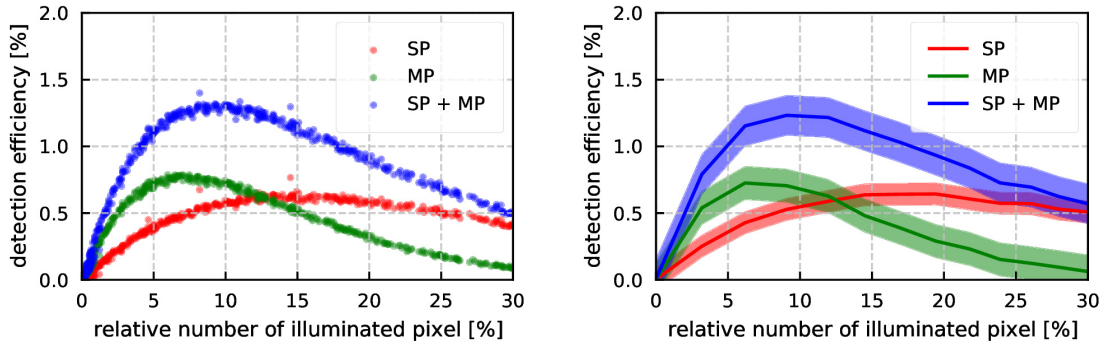

(a) Measured detection response.

(b) Simulated detection response.

Figure 4.13.: **Detection efficiency in experiment and simulation:** (a) shows the response of the algorithm for more than 1000 different shots with different photon flux and different experimental settings. The highest detection rate of events is visible for SP and MP events. (b) shows the simulated detector response using Monte Carlo simulations of the photon absorption patterns on the CCD. The shaded areas indicate a confidence interval of 1σ from 4 simulations. Simulation and measurement are in good agreement with each other.

of the pixels carry a charge. Higher fluxes will result in less detectable events although more photons are absorbed. Additional non-linear effects can cause further degradation of the spectrum, i.e., the energy-dependent probability for the detected type of event [127]. Nevertheless, the effect of spectral pile-up starts already at lower fluxes but can be compensated for the first leading order [7]. Thus, in order to obtain good conditions for the detection algorithm, less than 8 % of the pixel should be allowed to absorb photons.

The betatron experiments presented in chapter 6 were performed with a relative number of illuminated pixels of less than 8 %. The flux was tuned for the experiments. First, the detector was shifted away from the betatron source as far as permitted by spatial restrictions in the target area. Secondly, aluminum filter foils were placed at an angle of 45° on the beam axis. While shifting the detector was straightforward, using filter foils required more considerations. The foils had thicknesses of 100 µm, 200 µm and 300 µm. The surface of a foil was probed with a scanning electron microscope Hitachi S-4800 SEM. No mechanical deformation was found which could cause a spatially varying absorption. The chemical composition was determined by measuring the x-ray fluorescence with an energy-dispersive x-ray spectroscopy (EDXS) detector (Si(Li) detector with S-UTW-window from INCA, Oxford Instruments). The calculation of the transmission function is based on this result.

ENERGY CALIBRATION

The spectrum obtained from a single photon detector is a histogram $\mathrm{d}N_{\mathrm{event}}/\mathrm{d}N_{\mathrm{ADU}}$ of the events binned to Analog-to-Digital-Units (ADUs). The betatron spectrum $\mathrm{d}N/\mathrm{d}E$

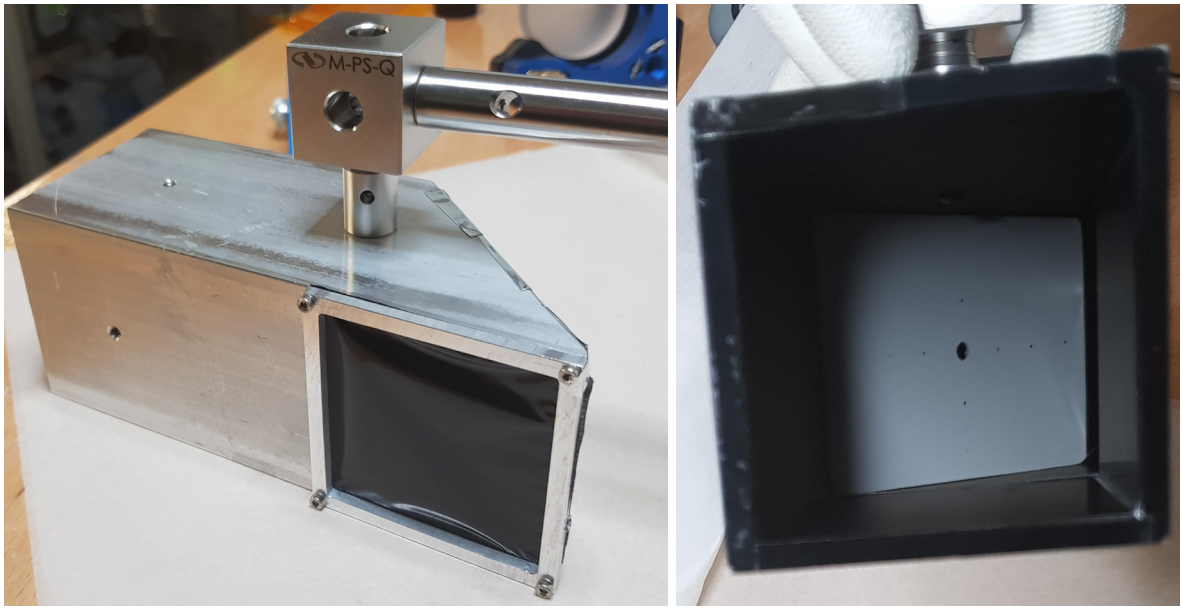

(a) Outside view. (b) Scintillator screen.

Figure 4.14.: **The betatron beam profiler:** (a) shows the beam profiler outside the vacuum chamber. The black, 14 µm thick Pokalon foil absorbs scattered laser light while allowing a high transmission for betatron radiation. The mounting frame enables a quick remove and installation of the foil for alignment issues.
(b) shows the scintillator screen inside the beam profiler.

is reconstructed by [88]:

$$\frac{\mathrm{d}N}{\mathrm{d}E} = \frac{\alpha}{QE(E)T(E)} \frac{\mathrm{d}N_{\mathrm{event}}}{\mathrm{d}N_{\mathrm{ADU}}}, \tag{4.2}$$

where E is the photon energy, $\alpha = 15.7\,\mathrm{eV/ADU}$ is the conversion factor obtained by calibration, $QE(E)$ is the quantum efficiency [128] and $T(E)$ is the transmission of all filters [129]. The calibration was performed for the Pixis camera with an americium-241 source (see appendix A, figure A.2). An energy resolution of ∼150 eV for the SP events was estimated from an iron-55 source. The theoretical Fano limited resolution [130] for single pixel events at Fe $K\alpha$ (5.9 keV) is $\Delta E_{\mathrm{FWHM}} = 100\,\mathrm{eV}$. Thus, the estimated and theoretical resolution limit are in good agreement.

4.4.2. BETATRON PROFILER

The divergent nature of betatron radiation requires a large area to detect the angular profile and pointing of the betatron radiation. This can be overcome with the use of scintillator screens such as for the electron spectrometer. The deployed screen is a Konica Minolta OG 400, commonly known as LANEX. The phosphor is based on gadolinium oxysulphide (Gd_2O_2S:Tb) which emits 545 nm light within 0.6 ms after excitation [131] by ionizing radiation, i.e., x-rays. Several other scintillators were examined by irradiating with an 8 keV Cu $K\alpha$ x-ray tube. The deployed screen delivered the highest light output and was for this reason selected for the setup.

Alternatively, image plates are commonly used [84]. They also offer a spatially resolved dose diagnostic of radiation [132]. However, a slow readout process is required, rendering theses detectors only useful for single shots.

Figure 4.14 shows the betatron beam profiler outside the vacuum chamber. It is placed after the electron spectrometer in order to protect it from the relativistic electrons. The intense laser light is reflected with a 14 µm thick aluminum foil to the laser beam dump. On the front and back side, 14 µm thick Pokalon foils absorb straying light.

The screen is placed at an angle of 45° with respect to the beam axis. The front side is imaged with a camera objective (Pentax zoom lens 12.5-75mm) onto a CCD camera (Basler acA640-120gm). The scintillator front side has vertical and horizontal scales with 10 mm spacing to enable spatial calibration. A 25 µm thick titanium foil protects the back of the scintillator from background radiation. A 3.5 mm on-axis hole in the scintillator and titanium foil allows transmission of betatron radiation to downstream x-ray detectors, i.e., x-ray camera. Additionally, it introduces a high absorption contrast in order to identify the relative position of the profiler with respect to the x-ray camera.

The low intensity of the scintillator light requires a dark environment. Internal reflections can introduce a higher background level and can increase the recorded light. Background light can interfere on the screen and can result in a distorted acquisition of the betatron profile. For this reason, the inner walls of the beam profiler are covered with light absorbent foil (Acktar Metal Velvet [133]). The foil effectively suppresses stray light in a wide band with a spectral absorptance of 99.9 %.

5. CHARACTERISTICS OF BETATRON RADIATION

In a laser wakefield accelerator, injected electrons experience strong accelerating fields as well as transverse fields of the plasma cavity, as shown in section 2.7. The focusing force induces the transverse oscillating motion of electrons around the propagation axis during the acceleration process. It results in the emission of betatron radiation with characteristics directly connected to the dynamics of the accelerated electrons, as shown in chapter 3. Hence, this radiation can be utilized as a powerful diagnostic for the transverse extent of the accelerated electrons inside the plasma.

The coherence properties of betatron radiation can be utilized for observing Fresnel diffraction [134, 135]. In this case, constructive and destructive interference causes fringes at the detection plane which depend on the source size. In this chapter, an implementation of the method is shown by backlighting the edge of a tantalum foil. The specific resolution limit is discussed including measured data and theoretical models.

In addition to utilizing the coherence properties, the shape of the betatron spectrum can be used for extracting the betatron radius. The betatron radius is the maximum elongation of the transverse electron distribution at the end of the acceleration process, as shown in section 3.3. Here, the betatron radiation is recorded by detecting the absorption of single photons and the spectrum is constructed by binning these events to an energy-resolved histogram [13, 108, 130]. Other techniques for measuring the betatron spectrum include Bragg diffraction by crystals [86], spectral filtering by Ross pair filters [136] or filter cakes [42]. However, they are limited to either the covered energy range or the energy resolution. Single photon detection typically accesses a broad energy range with a high resolution of $\sim$0.2 keV [130]. In order to estimate the sensitivity of the method, the experimental background radiation and effects from measurement uncertainties are investigated.

The angular profile of the far-field of the betatron radiation is determined by the average angular momentum [30, 31] of electrons in the bunch. The pointing of the betatron radiation is identical with the acceleration axis of the plasma cavity. The electron pointing is measured after the down-ramp and a drift space in vacuum. Combination of these two methods can provide valuable information of the electron dynamics in

the transition region from plasma to vacuum.

As an x-ray source, betatron radiation possesses unique properties, i.e., high flux with a broadband spectrum and a femtosecond short pulse duration. Many experiments require such a high number of photons per shot in a bandwidth of ∼1 keV, as will be shown in chapter 7. In order to estimate the available photon flux from the betatron source, the reconstructed betatron spectrum is extrapolated to the energy range from 1 keV to 25 keV.

First, section 5.1 describes the detection of betatron radiation and a model to deduce the source size by Fresnel diffraction. This is improved in section 5.2 by using a more advanced model based on the spectral shape of the detected spectrum. The angular profile is shown in section 5.3. Section 5.4 shows the photon flux of the betatron source for different injection schemes. Finally, section 5.5 summarizes the chapter.

5.1. SHADOW-BASED SOURCE CHARACTERIZATION

Figure 5.1a illustrates the basic setup for radiography. It consists of an x-ray source, a detector and an opaque obstacle between them. In general, the data recorded by the detector is called a radiograph. It can exhibit interference pattern caused by Fresnel diffraction [134, 135]. The formation of interference patterns requires spatial coherence, i.e., a well-defined phase and amplitude variation. This section will explain how Fresnel diffraction from a betatron source can be used for deducing the size of the source.

5.1.1. ILLUMINATED MICROSCOPIC OBJECTS

The important first step for betatron detection is to ensure that the detected radiation is originating from the studied source and not from undesired background radiation, such as Bremsstrahlung from relativistic electrons hitting parts of the setup. For this purpose, a mesh of tungsten wires with different diameters was placed on the axis between the interaction point and the x-ray CCD detector as shown in figure 5.1a. The detector was an Andor DO 934N-DN, as described in section 4.4. Installed at 5.7 m from the target, the camera was connected to a dedicated vacuum chamber and was placed in a separate lead shielded area. In order to reach the x-ray camera, betatron radiation from the LPA passed through 125 µm thick Kapton foil, 100 mm air, two 75 µm Kapton foils on an evacuated tube, 100 mm air and 75 µm Kapton foil with 14 µm Pokalon foil.

The radiographs in figure 5.1b and 5.1c illustrate the projections of the wires and the Fresnel target on the CCD chip of the cameras. The Fresnel target is addressed below in figure 5.2. A source larger than the backlit objects or an isotropic radiation background would cause a low contrast in the radiographs and multiple sources would cast multiple shadows. The absence in the radiographs of both, low contrast and multiple shadows, indicates a low radiation background and a source of micrometer size. Data recorded with no charge detected in the electron spectrometer provided no detected x-rays which indicates that the x-ray signal is linked to LWFA.

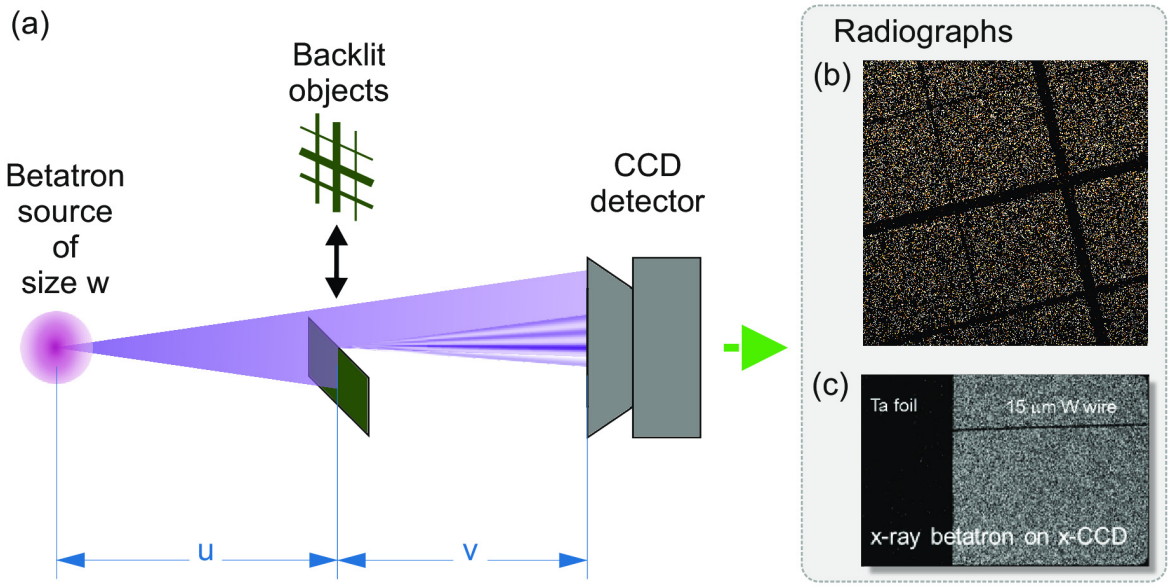

Figure 5.1.: **Schematic setup for radiography and Fresnel diffraction:** The setup used for radiography and Fresnel diffraction consists of the betatron source, the backlit object and the x-ray CCD are shown in (a). Accelerated electrons from the LPA (not shown) are deflected by the electron spectrometer before the inserted objects for imaging. The right side illustrates radiographs from a mesh of tungsten wires with diameters 15 µm, 50 µm and 100 µm in (b) and the Fresnel target in (c) as shown in figure 5.2.

5.1.2. FRESNEL DIFFRACTION

The radiographs provide the first step to deduce an upper limit for the source size. The next step in this thesis uses Fresnel diffraction, which describes diffraction in the near field. Since the method is applicable in the experimental setup, the data acquisition remained unchanged.

COHERENCE

To date, the smallest betatron source size found in an LPA is 0.1 µm [94]. Typically, such a source is spatially and temporally incoherent. The spatial incoherence is caused by the source size, which is larger than the emitted wavelength of <1 nm (>1 keV). The temporal incoherence originates from the acceleration process, where the spectrum varies with the electron energy, as shown in chapter 3.

However, a degree of coherent illumination can arise when only a fraction of the radiation is selected by spatial or angular filtering. The van-Cittert Zernike theorem states that radiation from uncorrelated emitters is spatially coherent to the complex degree of coherence µ. For a Gaussian distributed source, the theorem gives [137]:

$$\mu = |e^{-\frac{1}{2}(kw\theta)^2}|, \tag{5.1}$$

where k is the wavenumber of the radiated waves, w is the standard deviation of

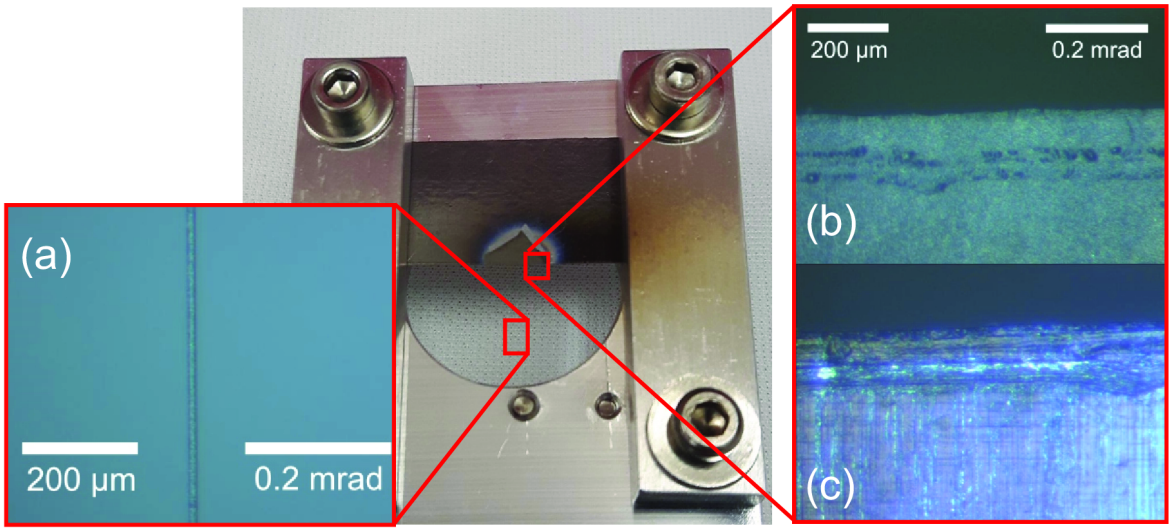

Figure 5.2.: **Fresnel target:** The Fresnel target (center) used for backlighting with x-rays consists of (a) a tungsten wire with 15 µm diameter and (b) an edge of the tantalum foil with 100 µm thickness after 1000s of laser shots. (c) displays the edge before the laser shots.

the transverse extent of the source and θ is the maximum angle of two points in the source. The angle can be approximated by $\theta \simeq A/u$ for a source with characteristic size A. A degree of high coherence with $\mu \rightarrow 1$ denotes a coherent source and allows for fringes with high contrast.

The degree of coherence $\mu = e^{-1/2}$ defines the spatial coherence length with $L_{\text{tran}} = u/(kw)$. Assuming a 1 µm large source and photons with an average energy of 5 keV yields $L_{\text{tran}} = 45\,\mu\text{m}$ for the Fresnel target at $u = 1.125\,\text{m}$. The spatial coherence length is approximately ten times larger than in the setup of Kneip et al. [135]. The temporal coherence length is given by [137] $L_{\text{long}} = \lambda^2/(2\Delta\lambda)$. For betatron radiation with a bandwidth of $\Delta\lambda = \lambda$, L_{long} is smaller than nanometers. Thus, the radiation is not temporally coherent.

For the experimental conditions, the degree of coherence is typically sufficient for a single Fresnel fringe (see appendix B). Further oscillations and fringes are damped (see appendix B, figure B.4). The fringe has a width of 20 µm, which defines the minimum spatial resolution required by the analysis.

SETUP FOR FRESNEL DIFFRACTION

In order to increase the sensitivity of the x-ray diagnostic for high x-ray energies, the Andor x-ray camera was replaced by the Pixis-XO 400BR, which is described in section 4.4. The overall transmission function from the source to the CCD chip remained unchanged. Figure 5.2 shows the used Fresnel target. The target is at 1.125 m and the CCD at 5.7 m distance to the source. The setup had a magnification of 5×. An aluminum foil reflected the intense laser light to the laser beam dump and protected the target from intense laser light. This foil had an on-axis 5 mm hole for optimal transmission of the x-rays. The spot on the tantalum foil marks the imprint from the

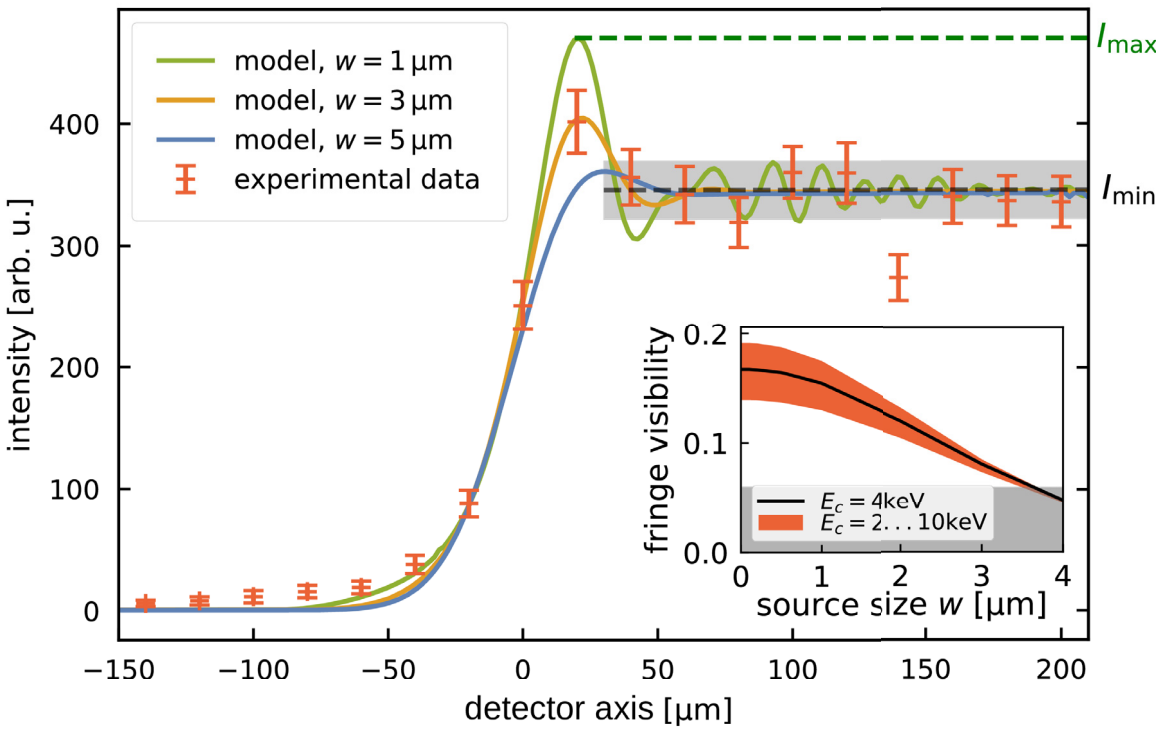

Figure 5.3.: **Measured intensity profile and various model data:** Model data from three different source sizes w are fitted to the experimental data. The sampling of the first fringe in the experimental data indicates the resolution limit of the technique. The gray area illustrates the noise level in the main plot and inset. On the bottom right, the inset illustrates the detection limit of the technique. The resolution depends on the visibility of the first fringe which is defined by the fringe contrast $(I_{max} - I_{min})/(I_{max} + I_{min})$. The contrast increases for smaller source sizes. The red area shows the variation of the contrast for critical energies from 2 keV to 10 keV. The black line depicts a spectrum with a critical energy of 4 keV.

residual laser light. The recorded intensity on the CCD is shown in figure 5.1c.

Fresnel diffraction occurs when an electromagnetic wave with a wavelength λ passes an obstacle, i.e., aperture or knife edge and diffracts in the near-field. For diffraction in the near-field, the Fresnel number $F = A^2/(v\lambda)$ must be larger than one. With a characteristic aperture size $A = 10\,mm$, an image distance $v = 4.6\,m$ and an x-ray wavelength $\lambda < 1\,nm$, the setup has a Fresnel number of 2×10^4 which is larger than one, requiring treatment in the Fresnel regime. Therefore the solution of the Kirchhoff integral for a backlit half-plane can be used to build a model of the intensity distribution (see appendix B).

COMPARISON WITH EXPERIMENTAL DATA

Figure 5.2 illustrates the target which was backlit with the betatron x-ray beam for Fresnel diffraction. It consisted of a 100 µm thick tantalum foil and a 15 µm thick

tungsten wire. The edge of the foil was cut with standard precision shears to sustain a suitable edge and aligned vertically to the x-ray detector. The transmission through the tantalum foil was less than 4×10^{-5} for x-ray energies below 20 keV, resulting in a step-like transmission function. The target was placed behind the electron spectrometer at 1.125 m distance, reaching a high flux and large magnification while minimizing target deterioration.

For the data shown in this chapter, 50 % to 80 % of the pixels carried an x-ray signal in the illuminated area on the CCD. The vertical pointing error indicated by the wire was negligible. The fluctuation in horizontal pointing of the betatron radiation was found to be ∼1 pixel. Thus, an accumulation of several shots would result in an intensity distribution that is dominated by the horizontal pointing of the betatron radiation and not by Fresnel diffraction. In order to obtain a reasonable signal-to-noise ratio, the single shot data was integrated along the edge (see appendix B).

Figure 5.3 compares measured data and the Fresnel model for different source sizes. The first Fresnel fringe is about 1 pixel in width, which is below the Nyquist rate from the Nyquist-Shannon sampling theorem [138]. Thus, it cannot be adequately resolved by the setup. Only an upper limit of 3 µm for the source size can be estimated by fitting on the rising slope. Increasing the magnification would improve the fringe width. However, shifting the target upstream would cause it to deteriorate faster. The alternative would be to shift the detector further downstream but that would also decrease the x-ray intensity on the detector. Thus, the noise on the detector would increase and become larger than the fringe. Shown in gray, the noise level of the x-ray intensity is given by the average error of the recorded x-ray intensity.

The inset of figure 5.3 shows the visibility of the fringe calculated as $(I_{max} - I_{min})/(I_{max} + I_{min})$, where I_{max} is the maximum intensity at the peak of the fringe and I_{min} is the minimum intensity of the recorded x-rays. The x-ray noise level is marked in gray and denotes the upper limit for a detectable source size with 3.5 µm. The lower limit for the detection of the source size can be 1.5 µm. Smaller source sizes have the same fringe visibility within the uncertainty range of the spectrum.

5.1.3. ADVANTAGES AND DISADVANTAGES

Fresnel-based reconstruction of the betatron source size has the advantage of using a single shot diagnostic that only relies on the recorded x-ray intensity. No further beam parameters from different diagnostics, i.e., electron spectrometer or plasma density interferometry, are required. The high photon flux can provide a reasonable signal-to-noise ratio for single shot measurements.

The limited coherence properties of betatron radiation are in most experiments [87, 134, 135] restricting the visibility of the interference pattern to the first fringe. As shown above, high magnification is crucial for resolving the diffraction fringe. This can lead to a compact setup, where the distance between the target and source is minimized in order to obtain a high magnification and a reasonable signal-to-noise ratio. However, some unfavorable effects can be:

Fresnel target deterioration The intense laser light can deteriorate the Fresnel target as shown in figure 5.2b and 5.2c. The decreased quality of the edge leads to

a degraded signal. A laser blocker made of a thin foil would degrade the coherence properties and decrease the x-ray flux. Thus, the target material requires a high melting point.

Bremsstrahlung background Relativistic electrons can hit parts of the Fresnel target and can produce an undesired background of Bremsstrahlung. In order to have a high absorption contrast and a high melting point, high-Z materials are typically used, which lead to more Bremsstrahlung. To avoid Bremsstrahlung, a magnetic field can deflect electrons from LWFA, as it was done by the electron spectrometer discussed in section 4.3.3. However, the length of the magnetic field can be the biggest restriction in the setup and for the magnification.

5.2. SOURCE SIZE RECONSTRUCTION BASED ON SPECTRAL SHAPE

As described in chapter 3, the transverse electron dynamics strongly correlate with the spectral shape of the emitted x-rays from betatron oscillation. This characteristic behavior can be utilized to explore the transverse electron beam dynamics during the acceleration. In order to record the betatron spectrum, the experimental setup described in section 4.3 was used and the x-ray diagnostics presented in section 4.4 acquired the betatron radiation.

5.2.1. BETATRON SPECTROSCOPY SETUP

In order to record the x-ray photons from the betatron radiation, the Pixis-XO 400BR was connected by a beamline to the main vacuum chamber, shown in section 4.4. A beryllium window in the beamline protected the CCD from scattered laser light. The camera operated in the single photon detection mode (see appendix A).

A careful single-shot analysis of the betatron spectrum requires a simultaneous measurement of betatron spectrum and background spectrum. For that reason, the area on the x-ray CCD was divided into three different regions of interest (ROI) as shown in the inset of figure 5.4:

Unfiltered ROI (A): The direct acquisition of the betatron spectrum which was only filtered by the beryllium window resulted in too many hits. A single pixel analysis was not possible. However, the ROI can indicate the total energy of the spectrum.

Filtered spectrum (B): The betatron spectrum required attenuation because of the high flux of betatron photons. This was achieved with a 200 µm aluminum filter foil which was placed at an angle of 45° to the laser axis. The foil reduced the betatron flux to a proper level for single photon detection, as described in section 4.4. The surface of the foil was probed with a scanning electron microscope Hitachi S-4800 SEM. The chemical composition was determined by measuring the x-ray fluorescence with an energy-dispersive X-ray spectroscopy (EDXS) detector (Si(Li) detector with S-UTW-window from INCA, Oxford Instruments).

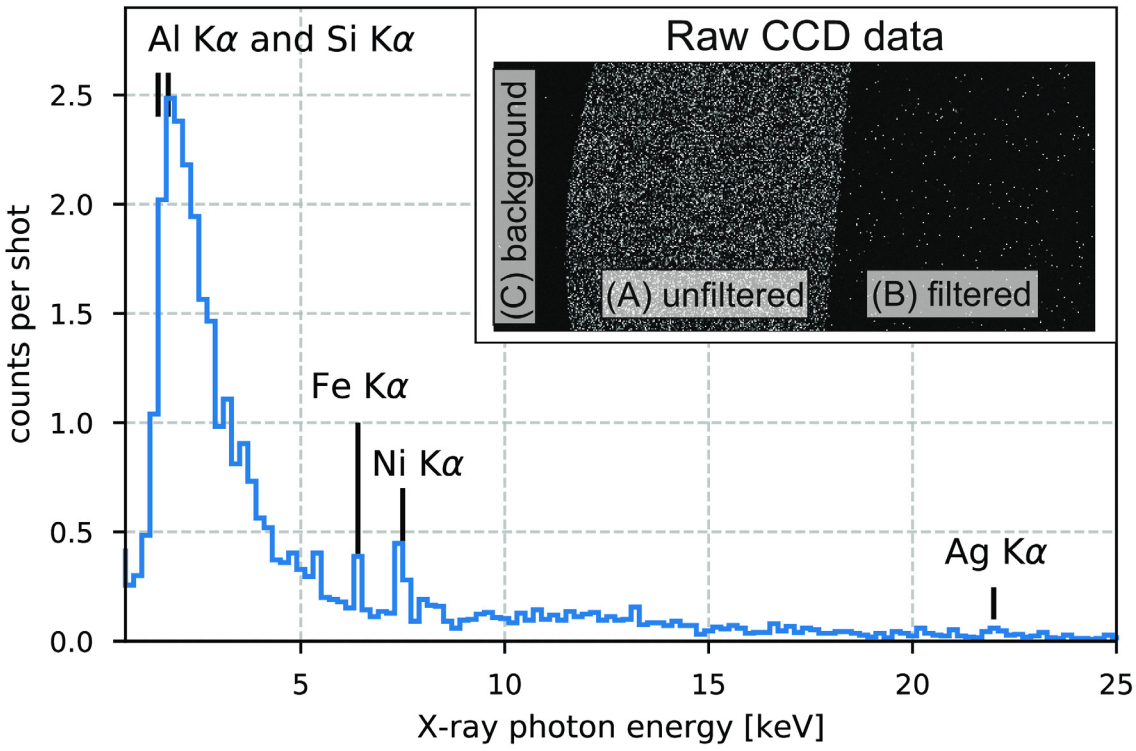

Figure 5.4.: **ROIs and background spectrum:** The inset depicts the different regions of interest on the x-ray CCD. The background spectrum is obtained from the background ROI (C) by averaging over 250 shots. The *Kα* x-ray fluorescence lines from iron, nickel and silver are marked at 6.4 keV, 7.4 keV and 22.99 keV. *Kα* lines from aluminum (1.5 keV) and silicon (1.7 keV) are merged in one peak which is broadened by the nonlinear quantum efficiency and elastic scattering on beamline elements.

Background spectrum (C): The third ROI was blocked by the 12.7 mm thick steel frame of the beryllium window. Events in this ROI typically originate from background radiation of the experimental setup, e.g., scattered photons, x-ray fluorescence, Bremsstrahlung from a beam dump.

Figure 5.4 presents the background spectrum averaged over 250 shots with LWFA. The continuous background can be produced by elastic x-ray scattering in the setup. The betatron radiation has a typical incoming angle of ≈0.1° at the beryllium window. For example, x-rays with an energy of ≈2 keV require an angle smaller than ∼0.5° for reflection [46]. Although the surface quality is far away from optical quality, a fraction of the x-ray photons can be reflected on the surface of the iron frame of the window. Additionally, x-ray fluorescence of beamline elements can contribute to the background. The fluorescence *Kα* lines from aluminum (Al), silicon (Si), iron (Fe), nickel (Ni) and silver (Ag) are marked with black lines. Parts of the main vacuum chamber and x-ray beamline consisted of iron, nickel and aluminum. The very weak silver peak can be caused by the coating of the dipole magnets of the electron spectrometer. Synchrotron radiation from deflected electrons in the electron spectrometer can

be excluded by the critical energy given by equation (3.1) that is less than 0.2 keV.

5.2.2. BACKGROUND RADIATION FROM LWFA

Several processes other than betatron oscillation can produce radiation in LWFA: Plasma electrons scattered by other electrons and ions produce Bremsstrahlung. The wiggling of electrons in the electric field of the laser pulse generates Larmor radiation. Electrons caught by ions produce recombination photons and transition photons. The flux of these sources needs to be estimated for quantitative analysis.

BREMSSTRAHLUNG WITH LWFA

Bremsstrahlung is produced when a charged particle is accelerated in the Coulomb field of another charged particle. The spectrum is typically continuous up to the maximum energy of the decelerated particle. Inside a plasma, electron-electron, ion-ion and electron-ion collisions are possible, but only the last type contributes significantly to the background radiation [139, 140].

In the case of electron-ion collisions, two types of Bremsstrahlung can be distinguished: Thermal and relativistic Bremsstrahlung [140]. After the laser pulse has propagated through the plasma, the hot plasma radiates thermal Bremsstrahlung as a result from the high plasma temperature. Although the number of electrons can be huge, the radiation is isotropically radiated and thus the number of photons emitted within a solid angle is small. For example, a typical solid angle of $\sim 1\,\mathrm{mrad}^2$ collects less than one millionth of all photons from thermal Bremsstrahlung.

In contrast to thermal Bremsstrahlung, relativistic Bremsstrahlung is produced by electrons oscillating in the electromagnetic field of the laser pulse. Here, electrons become relativistic because of the high intensity and the radiation is collimated on the laser axis. Ueshima et al. [141] have found a formula for the radiation power by numerical calculations. The radiated power per electron averaged over the laser period is given by [141]:

$$P[\mathrm{W}] \simeq 3.24 \times 10^{-8} a_0 \left(0.6 a_0^{3/2} + 1\right) \left(\frac{1\,\mu\mathrm{m}}{\lambda_0}\right)^2 \left(\frac{Z}{10}\right)^2 \left(\frac{n_i}{10^{20}\,\mathrm{cm}^{-3}}\right), \qquad (5.2)$$

where Z and n_i are the proton number of the ions and the ion background density, respectively. For a helium plasma with density $n_i = 5 \times 10^{18}\,\mathrm{cm}^{-3}$, $a_0 = 3$ and a wavelength $\lambda_0 = 0.8\,\mu\mathrm{m}$, the radiated power per electron is $\sim 1\,\mathrm{nW}$. Assuming further 30 fs pulse duration and that all energy is emitted at 1 keV, then 10^{-7} photons per electrons can be emitted. For typical experimental conditions, the number of betatron photons per electron and betatron period, that is given by equation (3.19), is larger than 2×10^{-2}. Thus, the number of photons from relativistic Bremsstrahlung is more than five orders of magnitude smaller than from betatron photons and thus negligible.

OTHER RADIATIVE PROCESSES

Electrons emit Larmor radiation during the figure-eight oscillation in the relativistic electromagnetic field of the laser. However, this radiation is mainly emitted at a longer

Table 5.1.: **Typical background radiation in LWFA:** Number of photons from background processes are estimated for LWFA experiments with plasma densities from $1 \times 10^{18}\,\mathrm{cm}^{-3}$ to $5 \times 10^{19}\,\mathrm{cm}^{-3}$, normalized laser intensity $a_0 = 4.6$, laser peak intensity $I_0 = 44 \times 10^{18}\,\mathrm{Wcm}^{-2}$ and laser spot size $w_0 = 6\,\mu\mathrm{m}$. Values from K. Phuoc [140].

Radiative process	Maximum spectral energy	Angular distribution	Number of photons
Relativistic Bremsstrahlung	MeV	collimated	10^5
Thermal Bremsstrahlung	keV	isotropic	10^{10}
Larmor radiation	keV, peak at 190 eV	collimated	10^{11}
High harmonic generation	~100 eV	laser cone	10^8/harmonic
Recombination	keV	isotropic	10^{11}
Transitions	Vis-UV	isotropic	10^{11}

wavelength and lower intensities than detectable in the setup [140].

In plasma, the recombination of an electron with an ion can produce an excited atom and can cause emission of characteristic radiation. While relaxing into lower states, the excited atom emits visible and ultraviolet photons. The recombinations and transitions radiate in the full solid angle. The maximum photon energy is the ionization energy and thus smaller than 1 keV for the used gases, as shown in section 2.1, table 2.1.

Electrons in the rising edge of the laser pulse experience an oscillating electric field. If this field is stronger than the Coulomb potential of their atom, they can be ionized as described in section 2.1. When the electron returns to the parent ion with significant kinetic energy, its energy can be converted to high harmonic photons. This radiation is collimated on the laser axis and reaches a maximum energy E_m [46]:

$$E_m = 3.17\,U_p + E_{\mathrm{ion}}, \tag{5.3}$$

where E_{ion} denotes the ionization energy and $U_p(I)$ is the ponderomotive energy from equation (2.9). An optimal laser intensity I for high harmonic generation is $\sim 10^{15}\,\mathrm{W/cm}^2$ [140] which can ionize helium or the first two electrons from a nitrogen atom ($E_{\mathrm{ion}} \lesssim 30\,\mathrm{eV}$, see table 2.1). A laser pulse with $\lambda_0 = 0.8\,\mu\mathrm{m}$ and a ponderomotive energy of 60 eV can theoretically generate high harmonics with the maximum energy of 220 eV.

Table 5.1 shows a summary of the discussed radiation processes possible in laser-plasma accelerators. As discussed above, the radiated photons are typically below the detection range, less frequent than betatron photons or isotropically distributed.

5.2.3. BETATRON RADIATION MODEL

The model spectrum to deduce the betatron source size r_β is based on equation (3.28). The equation assumes a Gaussian distribution in space for the electron bunch and considers a linear energy gain without nonlinear effects, i.e., dephasing of the electrons or interaction of electrons with the laser pulse. The angle integration is

Table 5.2.: **Measurement uncertainties used for sensitivity analysis:** Measurement uncertainties implemented for the sensitivity analysis.

Measured quantity	Relative error (RMS)
Plasma density	1 %
Electron energy	3 %
Charge	0.5 %
x-ray counts	$\sqrt{N}$ for N counted photons
Background radiation	energy dependent, see figure 5.4

numerically performed over the solid angle covered by the x-ray CCD camera. The plasma density n_e is assumed to be constant along the acceleration and the plateau density is taken from measurements as described in ref. [12].

The measured electron spectrum provides the final electron charge density $\mathrm{d}Q/\mathrm{d}E(\gamma_f)$ of the bunch. The minimum electron energy of 100 MeV is considered to radiate above 1 keV. Folding $\mathrm{d}N/\mathrm{d}E_{\mathrm{bunch}}$ from equation (3.28) with $\mathrm{d}Q/\mathrm{d}E(\gamma_f)$ returns the spectrum $\mathrm{d}N/\mathrm{d}E_{\mathrm{ideal}}$. It depends on the photon energy E and the betatron radius r_β at the end of the acceleration. In order to include the detection efficiency, the spectrum is multiplied by the quantum efficiency $QE(E)$ of the CCD chip [128] and the transmission function $T(E)$ [129]. Then, the background radiation $N_{\mathrm{BG}}(E)$ is added:

$$\frac{\mathrm{d}N}{\mathrm{d}E}_{\mathrm{mod}}(E, r_\beta) = QE(E)T(E)\frac{\mathrm{d}N}{\mathrm{d}E}_{\mathrm{ideal}}(E, r_\beta) + N_{\mathrm{BG}}(E). \tag{5.4}$$

The background $N_{\mathrm{BG}}(E)$ can be deduced from the spectrum shown in figure 5.4. The spectrum is divided by the total number of photons $\nu = \sum_E \frac{\mathrm{d}N}{\mathrm{d}E}_{\mathrm{mod}}(E, r_\beta)$. Then, multiplying by the number of detected photons ν_{Ph} returns a model that can be fitted to the experimental data:

$$n_{\mathrm{mod}}(E, r_\beta, \nu_{\mathrm{Ph}}) = \frac{\nu_{\mathrm{Ph}}}{\nu}\frac{\mathrm{d}N}{\mathrm{d}E}_{\mathrm{mod}}(E, r_\beta). \tag{5.5}$$

The model can be optimized to the experimental spectrum $\mathrm{d}N/\mathrm{d}E_{\mathrm{exp}}$ by defining the cost function f with the free fit parameters ν_{Ph} and r_β:

$$f(r_\beta, \nu_{\mathrm{Ph}}) = \sum_E w_E \left(\frac{\mathrm{d}N}{\mathrm{d}E}_{\mathrm{exp}}(E) - n_{\mathrm{mod}}(E, r_\beta, \nu_{\mathrm{Ph}})\right)^2, \tag{5.6}$$

where w_E is the weighting. The weighting is inversely proportional to the Gaussian error sum of transmission uncertainties and Poisson statistic of the recorded spectrum. The cost function becomes minimal for the best fit parameters $(r_\beta^{\mathrm{best}}, \nu_{\mathrm{Ph}}^{\mathrm{best}})$ which are obtained with an algorithm based on differential evolution [142].

5.2.4. SENSITIVITY OF BETATRON SOURCE SIZE RECONSTRUCTION

The measured parameters, i.e., plasma density, electron spectrum and betatron spectrum, have uncertainties: The plasma density is measured by interferometry [12], the

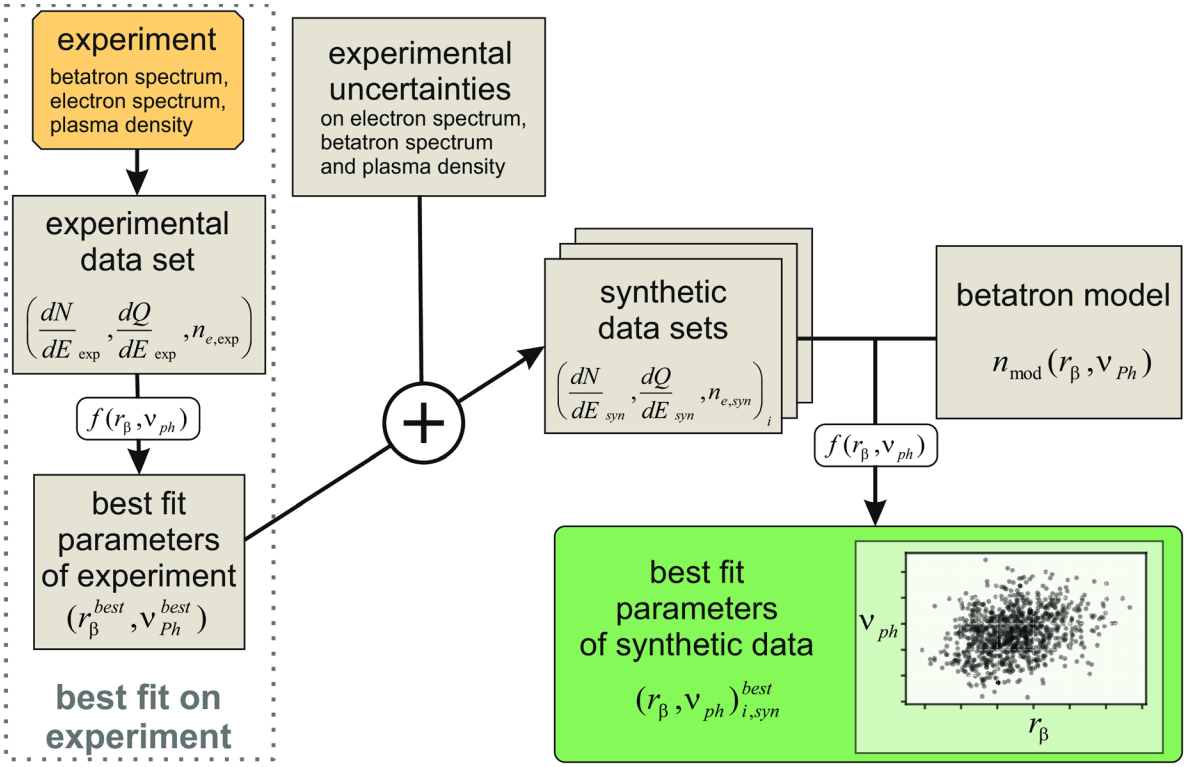

Figure 5.5.: **Sensitivity analysis workflow:** Workflow for generation and processing synthetic data to estimate uncertainties.

electron energy spectrum is measured by the electron spectrometer and the accelerated charge is recorded by an extensively charge calibrated lanex, as described in section 4.3. Table 5.2 shows the uncertainties of the measured parameters for the betatron model. In general, calculating the exact influence of measurement uncertainties requires exorbitant computational resources. Therefore, a Monte Carlo based approach is used to speed up computational time.

5.2.5. ERROR ANALYSIS WITH MONTE CARLO BASED SYNTHETIC DATA

A sensitivity analysis estimates how sensitive the output of a mathematical model is to the uncertainty of input parameters, taking into account possible sources of uncertainty from the experiment. Here, a Monte Carlo based approach is used, as shown schematically in figure 5.5.

First, the best fit parameters (r_β^{best}, $\nu_{\mathrm{Ph}}^{\mathrm{best}}$) are obtained from an experimental data set, when equation (5.6) becomes minimal. An experimental data set contains the betatron spectrum $\mathrm{d}N/\mathrm{d}E_{\mathrm{exp}}$, the electron spectrum $\mathrm{d}Q/\mathrm{d}E_{\mathrm{exp}}$ and the plasma density $n_{\mathrm{e,exp}}$. Then, multiple synthetic data sets are generated from one experimental data set. A synthetic data set consists of $\mathrm{d}N/\mathrm{d}E_{\mathrm{syn}}$, $\mathrm{d}Q/\mathrm{d}E_{\mathrm{syn}}$ and $n_{\mathrm{e,syn}}$. The synthetic data is obtained by varying the experimental data within the measurement uncertainties given by table 5.2. Adding Gaussian distributed random values to $\mathrm{d}Q/\mathrm{d}E_{\mathrm{exp}}$ and $n_{\mathrm{e,exp}}$ generates $\mathrm{d}Q/\mathrm{d}E_{\mathrm{syn}}$ and $n_{\mathrm{e,syn}}$. For $\mathrm{d}N/\mathrm{d}E_{\mathrm{syn}}$, a Poisson statistic based count noise is applied to the spectrum n_{mod} (r_β^{best}, $\nu_{\mathrm{Ph}}^{\mathrm{best}}$). At last, the best fit parameters $(r_\beta, \nu_{\mathrm{Ph}})_{i,\mathrm{syn}}^{\mathrm{best}}$

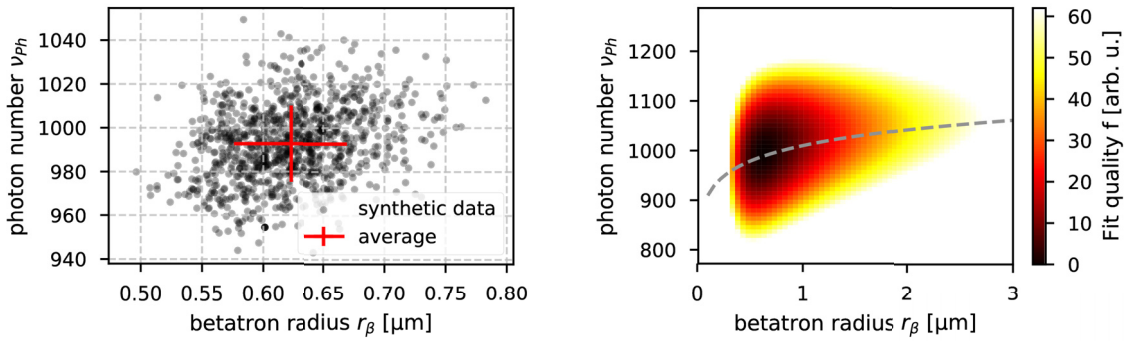

(a) Best fit parameters of synthetic data.

(b) The fit quality.

Figure 5.6.: **Results of the sensitivity analysis:** (a) shows the result of the Monte Carlo based sensitivity analysis. The gray data points represent best fits on a synthetic data set. The average of the population is denoted with the red cross and the error bar represents one standard deviation.
(b) shows the fit quality calculated by equation (5.6). A smaller value means a better agreement between model and experiment. The gray dashed line follows the minimum in ν_{Ph} for a given r_β.

are compiled by equation (5.6) for all synthetic data sets.

In total, 1024 synthetic data sets are generated per experimental data set. Figure 5.6a shows a typical result of the sensitivity analysis. The black points denote best fit parameters from a single synthetic data set. The red cross denotes the average of the population with the error bars corresponding to one sigma. By eye, there is no correlation visible between r_β and ν_{Ph} as it is the case for an orthogonal set of fit parameters. The orthogonality allows applying the Gaussian error law for further error analysis. A proper quantification is gained by directly calculating the fit quality with equation (5.6). Figure 5.6b shows the fit quality $f(r_\beta, \nu_{\mathrm{Ph}})$ for the experimental data set from figure 5.6a. It shows no correlation for both fit parameters r_β and ν_{Ph}.

5.2.6. BETATRON RADIATION FOR DIFFERENT INJECTION SCHEMES

The sensitivity analysis provides a measure of the error on the deduced betatron radius. The power of the implemented betatron model with the sensitivity analysis will be discussed with two different injection schemes: wave-breaking and self-truncated ionization-injection.

Experiments with the wave-breaking injection are in the nonlinear regime of interaction, as shown in section 2. This causes a moderate shot-to-shot reproducibility of the accelerated electrons which was visible in the experiments. Figure 5.7 illustrates a typical shot with wave-breaking. The quasi-monoenergetic bunch contains $\leq$10 pC (FWHM) with an electron energy of 345 MeV. The plasma density was $5.0 \times 10^{18}\,\mathrm{cm}^{-3}$. The distance from LWFA target to x-ray camera was 5.7 m. The betatron radius was deduced with the betatron radiation model and the sensitivity analysis described above to $r_\beta = (0.6 \pm 0.1)\,\mu\mathrm{m}$.

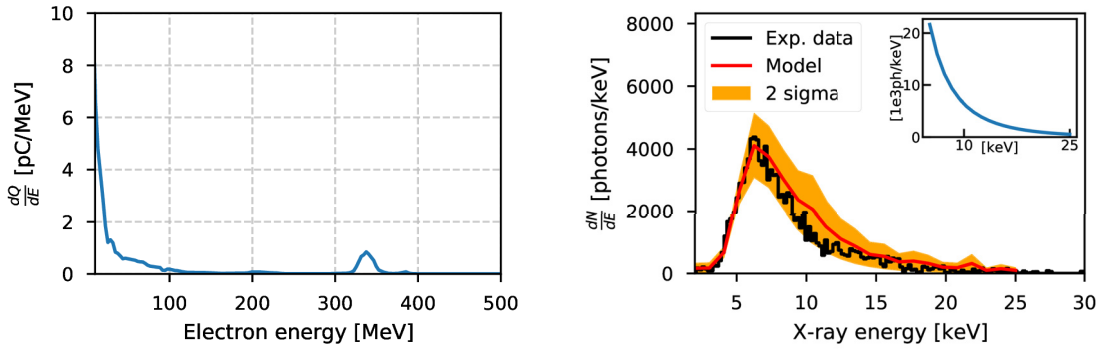

(a) Electron spectrum.

(b) Betatron spectrum.

Figure 5.7.: **Shot with wave-breaking injection:** (a) shows the electron spectrum of a shot with pure helium as plasma medium. The injected charge within the 35 MeV energy spread (FWHM) is 15 pC at 345 MeV mean energy. The plasma density was $5.0 \times 10^{18}\,\mathrm{cm}^{-3}$. (b) shows the betatron spectrum and the inset shows the reconstructed spectrum. The collection angle of the x-ray radiation was $4.2\,\mathrm{mrad}^2$ at 6 m distance from the source. More than 2×10^5 photons above 4.8 keV were detected. The betatron radius is $(0.6 \pm 0.1)\,\mu\mathrm{m}$.

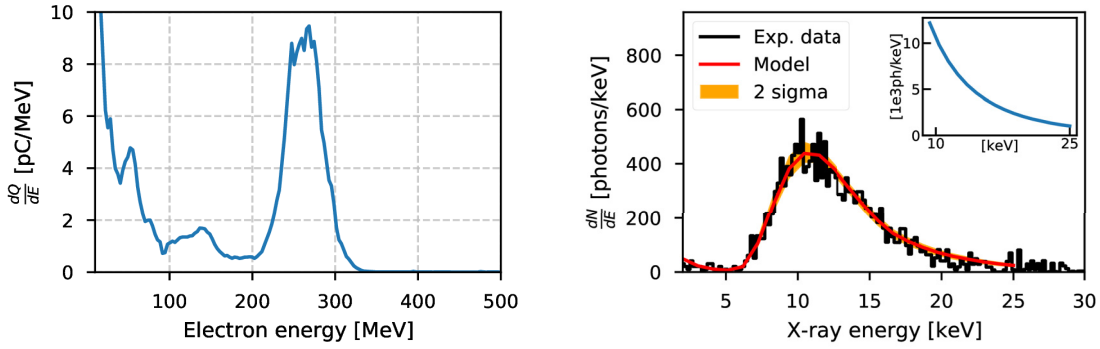

(a) Electron spectrum.

(b) Betatron spectrum.

Figure 5.8.: **Example of ionization-induced injection with high charge:** (a) shows the electron spectrum with an N_2 doping of 1 vol – %. A charge of 393 pC within an energy spread (FWHM) of 50 MeV gained a mean energy of 261 MeV. The plasma density was $5.0 \times 10^{18}\,\mathrm{cm}^{-3}$. (b) shows the betatron spectrum and the inset shows the reconstructed spectrum. The collection angle of the x-ray radiation was $1.1\,\mathrm{mrad}^2$ at 11.7 m distance from the source. More than 3200 x-ray photons above 7 keV were detected. The betatron source size is $(0.9 \pm 0.1)\,\mu\mathrm{m}$.

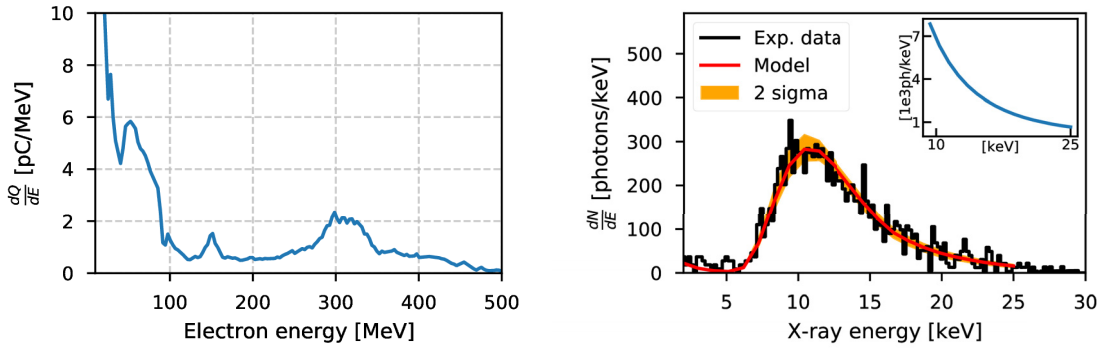

(a) Electron spectrum.

(b) Betatron spectrum.

Figure 5.9.: **Example of ionization-induced injection with low charge:** (a) shows the electron spectrum for a shot with an N_2 doping of 0.2 vol – %. The injected charge within the 66 MeV energy spread (FWHM) is 120 pC at 475 MeV mean energy. The plasma density was $5.0 \times 10^{18}\,\mathrm{cm}^{-3}$. (b) shows the betatron spectrum and the inset shows the reconstructed spectrum. The collection angle of the x-ray radiation was 1.1 mrad^2 at 11.7 m distance from the source. More than 2×10^3 x-ray photons above 7 keV were detected. The betatron source size is (0.7 ± 0.1) µm.

The disadvantages of wave-breaking injection, i.e., low amount of injected charge and reduced shot-to-shot stability, can be overcome without heavy setup modifications by deploying ionization-induced injection. A scheme with ionization-injection can typically inject more charge. In order to compensate higher betatron flux expected from the higher bunch charge, the x-ray camera was moved to 11.7 m. For systematic studies on the influence of the loading to the wake, ionization-induced injection is used to trap different number of electrons [9]. Figure 5.8 and 5.9 show shots with two different injected charges tuned by differently chosen dopings of N_2 (0.2 % and 1 %). For both cases, the plasma density was $5.0 \times 10^{18}\,\mathrm{cm}^{-3}$. The betatron spectrometer collected >2000 x-ray photons over a solid angle of 1.1 mrad^2.

Betatron radiation can be reliably used to deduce the betatron radius, as shown in chapter 6. However, systematic studies are challenged by the shot-to-shot reproducibility and the beam pointing stability. Therefore, the knowledge of the betatron beam pointing is a crucial prerequisite for analysis. The next section examines the correlation between electron and betatron pointing.

5.3. ANGULAR DISTRIBUTION

As described in chapter 3, the emitted frequency of betatron radiation is angle dependent. Pointing of the accelerated electrons leads to a pointing of the betatron beam. A systematic analysis of betatron radiation requires the knowledge of the emission angle. Therefore, the correlation between the horizontal pointing of electrons and betatron radiation is important.

The spatial resolution of the x-ray camera enables the recording of betatron radiation in a limited angular range. For the shots shown in section 5.2, the covered solid

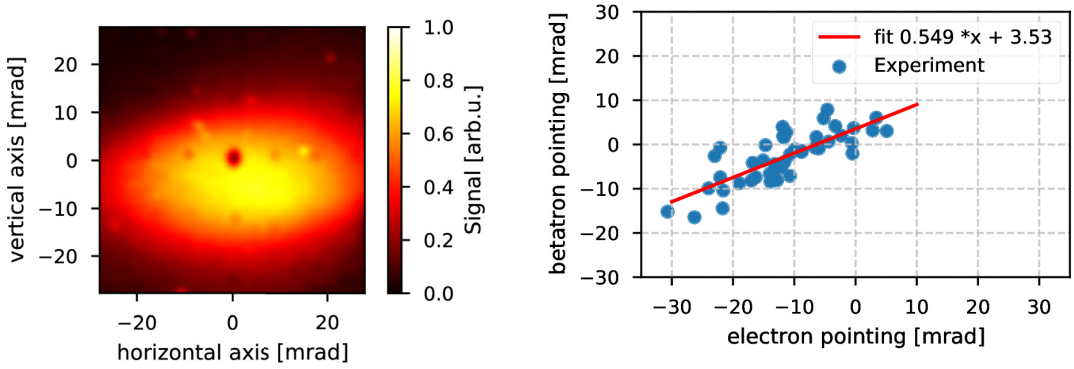

(a) Measured betatron profile.

(b) Correlation of horizontal pointing of electrons and betatron radiation.

Figure 5.10.: **Measured betatron profile and pointing:** (a) shows a typically measured profile of the betatron radiation. The laser polarization is along the horizontal axis. (b) represents the correlation of the horizontal pointing of the electron beam and the betatron beam.

angles were 4 mrad^2 and 1 mrad^2 for wave-breaking and STII, respectively. No angular dependence of the recorded radiation was visible within the recorded solid angle.

Figure 5.10a shows a betatron beam profile from ionization injected electrons. It shows that the preferred oscillation plane for higher energy electrons is typically parallel to the laser polarization [33]. Ta Phuoc et al. [31] studied the profile of the x-ray far-field in experiment and simulation. His results show that the dynamics of the oscillations (i.e., distribution of oscillation planes and angular momentum) affect the spatial profile of the betatron radiation. Randomly distributed oscillation planes result in circular profiles. If all oscillations are in a single plane, then the x-ray profile resembles an ellipse elongated along this plane.

Combining this data with the electron pointing in the electron spectrometer yields the correlation between electron and betatron beam pointing shown in figure 5.10b. This correlation enables the selection of shots with the same pointing, i.e., the same betatron emission cone, which helps to perform accurate analysis.

Besides for a diagnostic, the shown betatron spectra indicate the potential of betatron radiation as a powerful radiation source [143]. A more detailed overview of possible applications is given in chapter 7. One of the critical properties for a light source is the preferred high spectral flux which will be described in the next section.

5.4. BETATRON FLUX

Figure 5.11 illustrates the number of x-ray photons per shot within 1 eV bandwidth and a typical emission cone of 47 mrad × 23 mrad, as shown in figure 5.10a. The experimental data represents the betatron spectrum from figures 5.7, 5.8 and 5.9 which is unfolded with the transmission functions and the quantum efficiency. The simulated data is obtained from radiation simulations as described in section 3.4. Interpolated electron spectra were used for the simulation of spectra with large electron energy

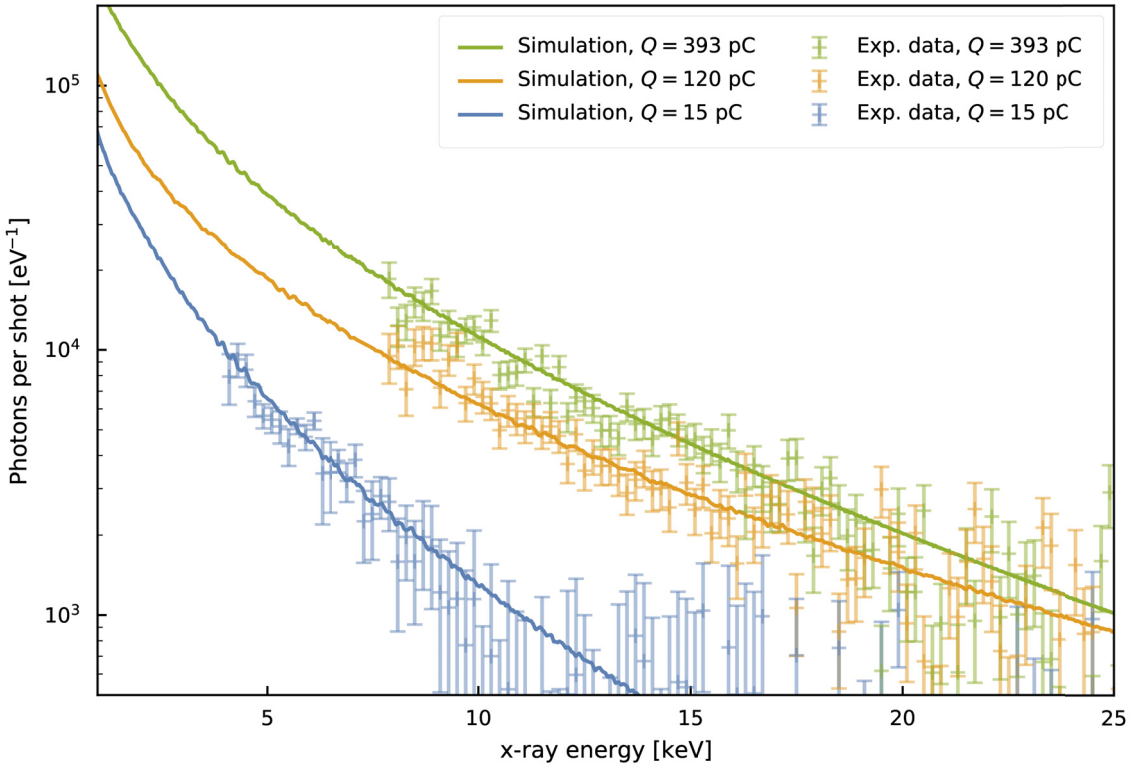

Figure 5.11.: **X-ray photons per shot:** Photons per shot within 1 eV in the full emission cone for the shots shown in figures 5.7, 5.8 and 5.9. The total number of photons is extrapolated by taking a typical emission cone of 47 mrad × 23 mrad (FWHM) as shown in figure 5.10. The highest charge Q = 393 pC provides the highest number of photons within the plotted range. This is caused by the higher number of injected electrons in comparison to the other shots. Although the electron spectrum for the two other shots indicates higher maximum electron energies, the number of photons at higher energies is still dominated by the number of emitters, i.e., injected charge.

spread as figure 5.9. The highest charge of ∼400 pC provided the highest number of photons because of the highest number of electrons that performed betatron oscillations. Although the electron spectrum for the two other shots indicates higher maximum electron energies, the photon flux for higher photon energies is still charge dominated.

The cross section for elastic x-ray scattering is higher than the absorption in low-Z elements common in biological tissues [144]. In this case, phase contrast is easier to achieve than absorption contrast. Phase contrast imaging (PCI) is not limited to a small bandwidth source but requires a certain amount of spatial coherence. The tiny spot size, that yields a certain degree of spatial coherence, in combination with the intrinsic short pulse duration (≈30 fs) and high photon flux enables measurements of shock compression [144] with a higher temporal resolution than possible at synchrotron facilities with a pulse duration of several 10s picoseconds. For PCI a broad

energy range from figure 5.11 comparable to energies of 3 keV to 10 keV is useful and contains more than 4×10^8 photons.

Besides using the x-ray phase contrast, the local atomic order and the electronic structure is accessible by analyzing the x-ray transmission around an absorption edge [144]. For an x-ray absorption technique as extended x-ray absorption fine structure (EXAFS), a narrow energy range ∼1 eV and a low signal-to-noise ratio are required. The typical noise for a signal of N photons follows the Poisson statistic, which provides a signal-to-noise ratio of $1/\sqrt{N}$. This means an ideal setup would collect $N = 1.7 \times 10^5$ photons at the aluminum $K\alpha$ energy of 1.49 keV and it would have a Poisson statistics based error of $1/\sqrt{N} = 0.3\,\%$. The same scenario at the iron $K\alpha$ energy of 6.4 keV would yield 2.6×10^4 photons with an 0.7 % error. In reality, the limited effectiveness of the setup degrades the signal-to-noise ratio.

In comparison with established $K\alpha$-sources [40], betatron radiation also provides a source with a short pulse duration [145] but is far more collimated. Thus, the source can be placed at a larger distance to a backlit object while maintaining the flux. This enables a better signal-to-noise ratio. Potential further applications are discussed in more detail in section 7.

5.5. SUMMARY

In this chapter betatron radiation has been presented as a diagnostic method for the electron dynamics inside the plasma cavity. Using coherence properties, a simple Fresnel diffraction based model was developed and applied to experimental data, resulting in an upper limit of the betatron source size of 3 µm. The analysis of the betatron spectral shape improves the accuracy of the analysis, measuring a betatron radius of ∼1 µm. The pointing of the angular betatron profile was discussed and found to depend on the electron pointing.

The critical parameters of betatron radiation, the total number of photons and photon energy, scale with $N_e\sqrt{\gamma n_e}r_\beta$ and $\gamma^2 n_e r_\beta$, where N_e is the number of electrons.

The plasma density scales with the basic setting for operating a stable LPA, i.e., the matched spot size, as shown in chapter 2. Increasing γ greatly increases the critical energy E_c and the photon energy but it has only a minor impact on the number of photons. Changing N_e is essential and limited by beam loading.

However, r_β can be increased by two approaches: First, electrons are injected with a substantial transverse offset resulting in large oscillation amplitudes. Transverse wave-breaking [146] or strong external magnetic fields are possible implementations. Secondly, the injected electrons can gain transverse momentum during the acceleration process by interacting with the electric field of the laser pulse. This is dominant in the self-modulation LWFA (SMLWFA), where the laser pulse length is longer than the plasma cavity and overlaps in space with the electrons. This has been shown by Albert et al. [147].

6. TRANSVERSE ELECTRON BEAM DYNAMICS IN THE BEAM LOADING REGIME

Recently, the generation of high charge electrons beams, up to 0.5 nC within a quasi-monoenergetic peak, has been demonstrated from LWFAs [9]. The performance of the accelerator has been improved by optimizing the beam loading effect, which results in a flattening of the accelerating field to minimize the energy spread. For applications, in addition to the peak energy and energy spread, the transverse momentum distribution of the electron beam needs to be controlled since it is important for transporting the electron beam into a dedicated setup. In this chapter, the effect of beam loading on the transverse electron beam dynamics is presented.

It has been shown at various experiments that the transverse emittance can be as small as 0.1 mm mrad [94, 103, 104]. However, in combination with large energy spread, it is still very challenging to deploy conventional beam transport elements, e.g., consisting of magnetic quadrupoles and sextupoles for beam collimation and chromaticity correction [148] and dipole magnets. Furthermore, the several milliradians of beam divergence with the micrometer beam size [85, 94] at the end of plasma accelerators causes the transverse beam size to grow very rapidly during propagation in vacuum. Such transverse beam properties are intrinsically limited by the injection scheme. Thus, for high charge beam generation, a method to obtain a small divergence that is not worsened by beam loading is essential for a highly efficient electron beam transport [149].

Beam loading in LWFA is a condition where the amount of injected charge is large enough such that the self-field of the bunch strongly superimposes the acceleration field of the plasma. As depicted in section 2.6, it reshapes and modifies the accelerating fields, locally affecting the acceleration efficiency. At specific electron beam parameters, the beam loading can be optimized leading to a constant accelerating field along the injected bunch. In this case, the electrons within the bunch experience the same accelerating field strength which results in the minimum energy spread. Beside the accelerating field, there also exist focusing fields pushing electrons toward the axis. For an initially off-axis electron, such focusing fields lead to

an oscillatory motion (called betatron oscillation) of electrons around the acceleration axis. While the oscillation amplitude is damped as electrons gain energy, the frequency of betatron oscillation depends on electron energy as shown in chapter 3. Thus, electrons within an energy spread will oscillate at different frequencies. Such frequency differences lead to a so-called betatron phase mixing, increasing the width of the transverse momentum distribution, that can result in a large beam emittance at the end of acceleration.

This chapter presents the generation of high charge electron beams together with betatron measurements, providing a hypothesis on how optimal beam loading leads to a smaller beam divergence. The first section 6.1 shows the recorded energy gain, spread, and divergence of the electron bunch together with the betatron radius and yield for different plasma densities. Then, section 6.2 provides the first attempt to explain the observed minimum in the normalized divergence while discussing the transverse electron dynamic via simulations. Section 6.3 concludes the chapter with a brief summary of the results.

6.1. EXPERIMENTAL DATA

In order to enable a systematic study of the beam loading effect to the electron beam dynamics, we kept most of the experimental parameters constant and only varied the doping concentration, thereby varying the number of injected electrons. This keeps the laser-plasma interaction almost unchanged, so the beam dynamic is expected to arise solely from the injection and acceleration process.

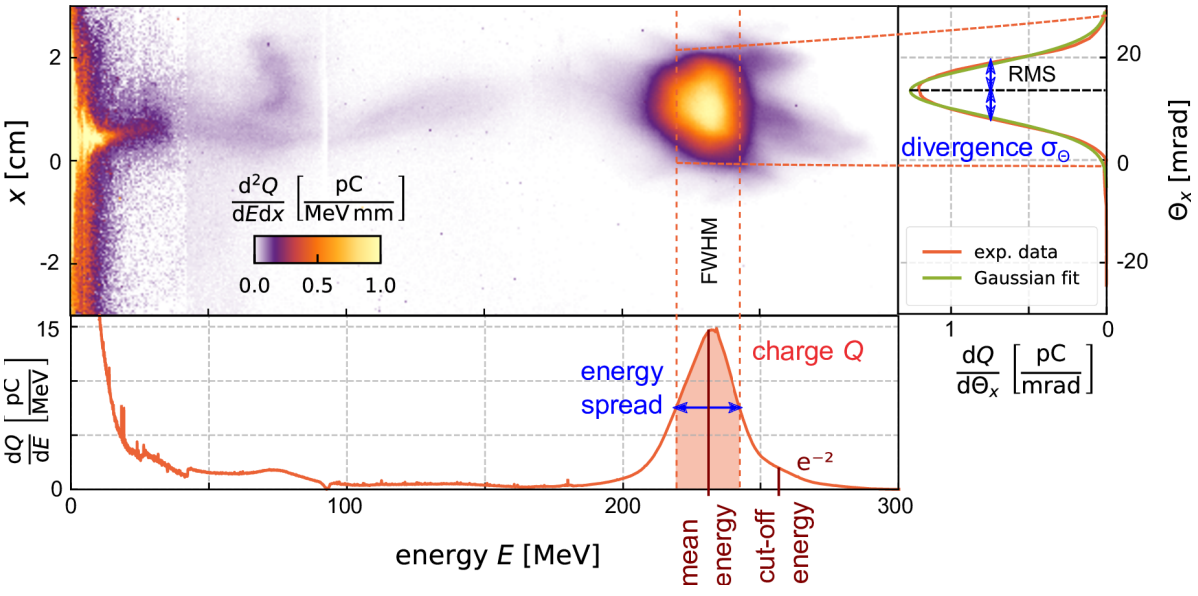

Figure 6.1.: **Typical electron spectrum and parameters:** A typical electron spectrum used for the analysis has a quasi-monoenergetic peak and low background. This allows us to deduce bunch charge, energy spread, cut-off energy, mean energy and beam divergence.

All data points presented in this chapter were recorded within the same experimental campaign and within 24 h to ensure that experimental day-to-day performance issues and setup stability of the laser system were eliminated. Temporal stability, far- and near-field of the laser beam were monitored online to verify a stable operation during the data acquisition. Similar data sets with the same experimental behavior as described below could be reproduced at succeeding measurement campaigns [6, 111]. Detail of the experimental setup is described in chapter 4.

A typical electron energy spectrum from the experiment is shown in figure 6.1. The spectrum was acquired using the electron spectrometer as described in subsection 4.3.3. The charge density $\mathrm{d}Q/\mathrm{d}E$, which is the histogram of the spectrum over the full collection angle, shows a quasi-monoenergetic peak. The peak and its full width at half maximum (FWHM) are used to quantify beam parameters in this thesis. The energy spread is defined as the FWHM of the peak and the center of the FWHM denotes the average electron energy. The charge Q of the bunch is the integrated charge density within the FWHM of the peak. The cut-off energy is defined by the maximum energy where the charge density drops below $e^{-2} \approx 0.135$ of the peak density. A histogram over the energy range within FWHM yields $\mathrm{d}Q/\mathrm{d}\Theta_x$. Then, a fit with a Gaussian function returns the root mean square (RMS) of the bunch divergence σ_Θ. In the following, the set of the electron bunch parameters along with betatron parameters from section 5.2 make a complete set that will be used to study the electron beam dynamics.

6.1.1. ELECTRON ENERGY AND ENERGY SPREAD

Figure 6.2 illustrates the effect of beam loading on the electron energy. Every point denotes a set of up to twenty consecutive shots. Higher plasma densities show a higher energy gain which is due to the stronger maximum field inside the plasma cavity, as discussed in chapter 2. The figure clearly shows the minimum of the energy spread at charge from 250 pC to 300 pC. In the same range of charge, the electron cut-off energy seems to drop to a constant value for higher charges. Since the injection phase space along one plasma density does not change, the different energy gain has to be attributed to a different longitudinal accelerating field gradient and thus to the acceleration process [52, 69], as examined in section 2.6. The large amount of injected charge deforms the fields inside the plasma cavity. The trailing electrons then experience an accelerating field that is reduced by the loading of the leading electrons. The optimal beam loading causes the electric field to be constant along the bunch, resulting in the minimum in energy spread.

To estimate laser-plasma parameters required to obtain optimal beam loading is challenging because it requires the exact knowledge about the laser power that drives the wake. As discussed in chapter 2, the laser pulse inside the bubble is subject to relativistic self-focusing, bunch compression and pump depletion as well as energy losses due to ionization. Furthermore, an assumption of a simplified plasma density profile is normally used. However, with equation (2.29), the required charge for optimal beam loading can be estimated to ∼300 pC, which consistently agrees with the observation in the shown data sets, where optimal beam loading seems to occur from 250 pC to 300 pC.

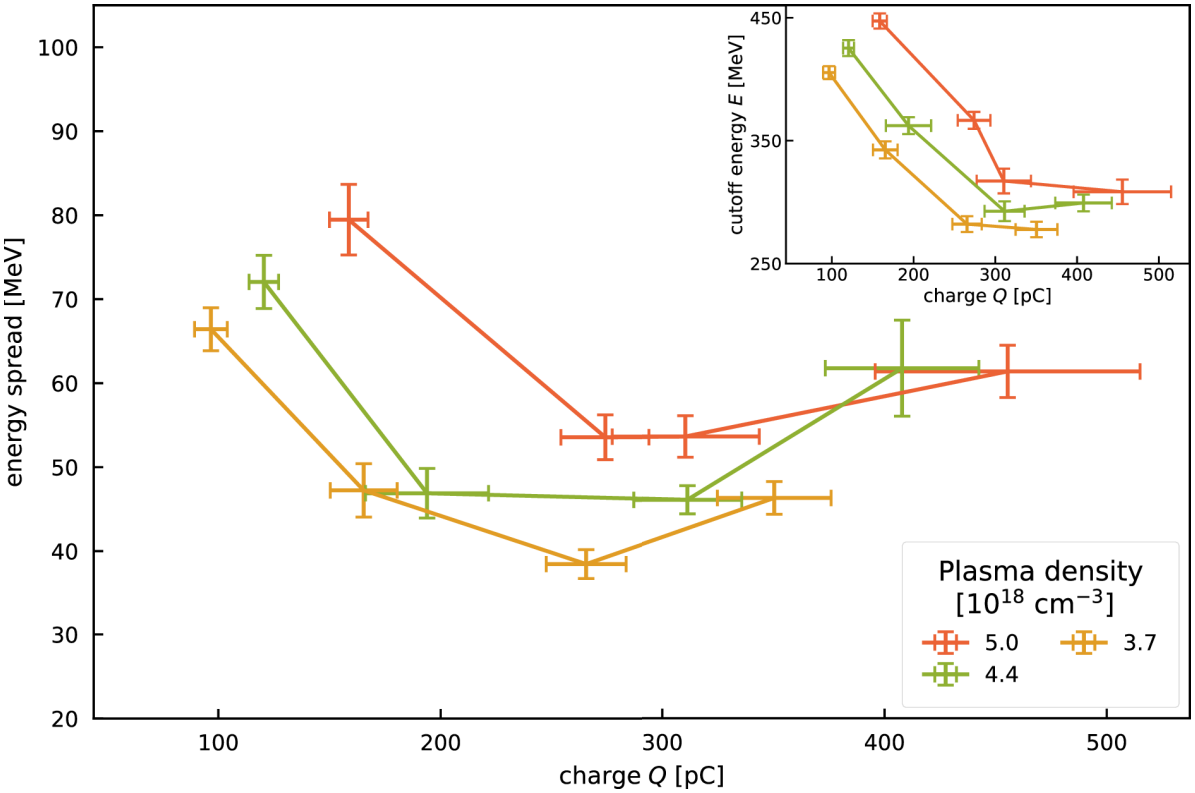

Figure 6.2.: **Influence of beam loading on electron energy:** The main plot illustrates the energy spread over charge for different densities. Each data point consists of up to twenty consecutive shots. A minimum around 300 pC is visible. At the same charge as shown by the inset, the cut-off energy changes from a monotonic decrease with charge to almost constant behavior. Energy spread and cut-off energy from a single shot are illustrated in figure 6.1.

Since the observed features can be attributed to the impact of beam loading on the longitudinal field and phase space, the next logical step is to look at the transverse beam characteristics which will be assessed by beam divergence and betatron radiation as in the following.

6.1.2. ELECTRON DIVERGENCE

The geometric divergence σ_Θ (see appendix figure C.1) of the electron beam can be extracted from the nondispersive plane of the electron spectrometer as shown by figure 6.1. The direct interpretation of σ_Θ is challenging since the geometric divergence measured in the laboratory frame depends on the bunch energy. Therefore, a more convenient figure of merit is the normalized divergence $\gamma\sigma_\Theta$ which enables direct comparison of the normalized transverse momentum. As mentioned in section 3.5, the normalized transverse momentum is the transverse momentum in the average rest frame of the bunch. The same applies to the transverse momentum spread of a bunch which is directly proportional to the normalized divergence. Thus, $\gamma\sigma_\Theta$ can make a direct comparison of the momentum spread of the bunch and does

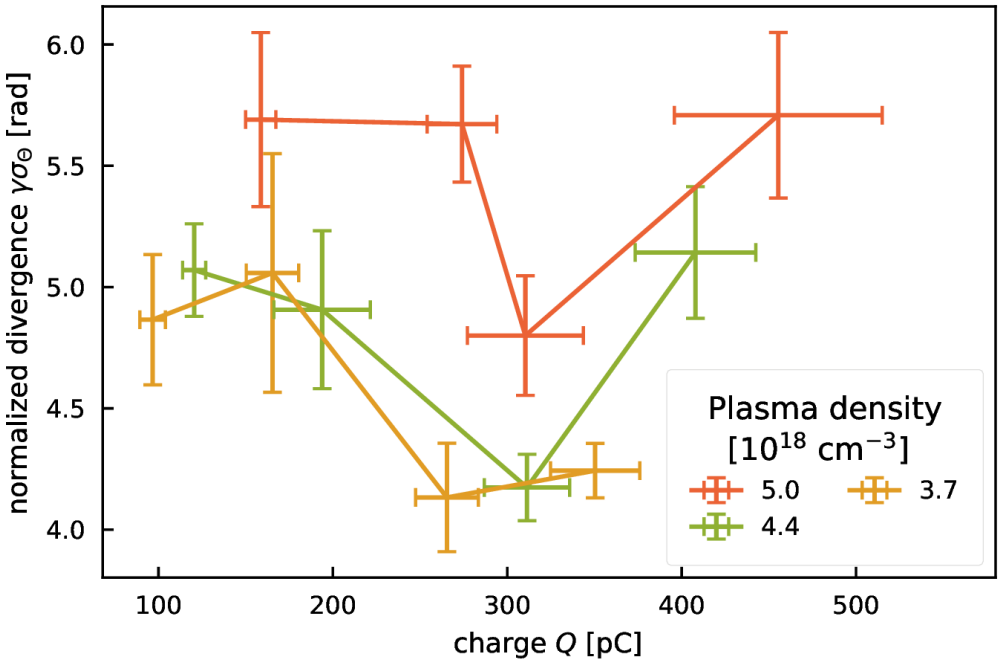

Figure 6.3.: **Normalized electron divergence:** A minimal normalized divergence $\gamma\sigma_\Theta$ can be observed at the same charge where optimal beam loading occurs in energy and energy spread as shown by figure 6.2.

not depend on the energy gain.

Figure 6.3 shows $\gamma\sigma_\theta$ where γ was obtained from the cut-off energy. The normalized divergence for all plasma densities show a clear minimum with less than 5 rad at optimal beam loading. The plasma density of 5×10^{18} cm^{-3} tends to have larger normalized divergences than lower plasma densities. The lowest plasma density of 3.7×10^{18} cm^{-3} has the smallest normalized divergence of 4.1 rad at a charge of 265 pC. As described in section 2.7, the strength of the focusing fields depends on the plasma density. A higher plasma density leads to a stronger focusing force which is proportional to the square root of the plasma density. Thus, after exiting the LPA, the divergence of the electron bunch increases with the plasma density.

The transverse phase space can be explained by two separate parameters as discussed in chapter 3. The first parameter is the transverse momentum spread that can be inferred from the beam divergence as shown above. The second parameter, the beam size, can be accessed by the recorded betatron radiation, as shown below.

6.1.3. BETATRON RADIUS AND YIELD

A complementary measure to the transverse momentum is the electron beam spot size. The small dimensions ~1 µm makes a direct beam profile measurement extremely challenging, i.e., with screens or with CTR [5]. As explained in chapter 5, measuring the spectral shape of emitted radiation from the beam during accelera-

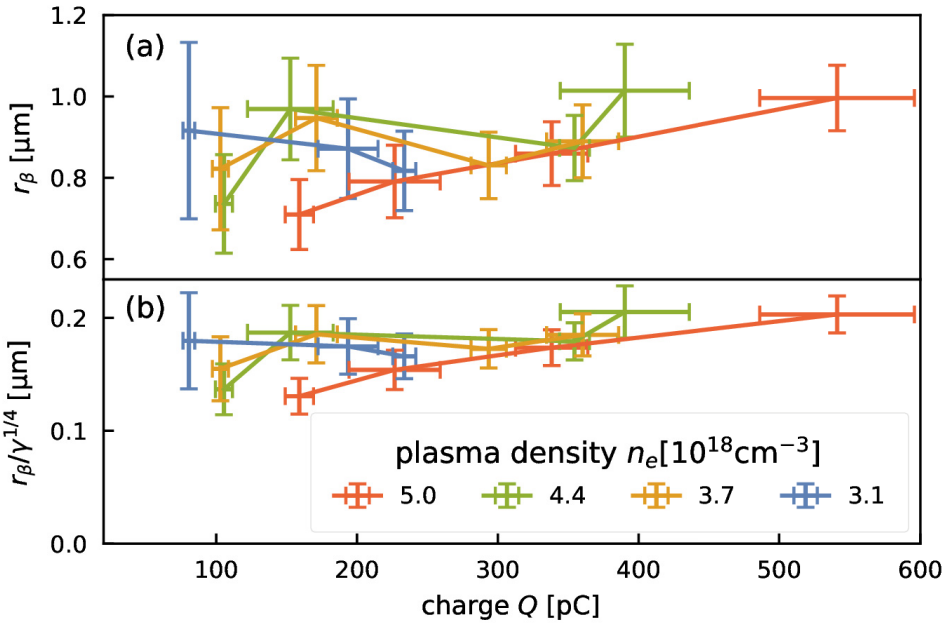

Figure 6.4.: **Betatron radius:** (a) shows the betatron radius r_β for different plasma densities and (b) shows the corresponding normalized betatron radius $r_\beta/\gamma^{1/4}$. The legend in (b) applies accordingly to (a).

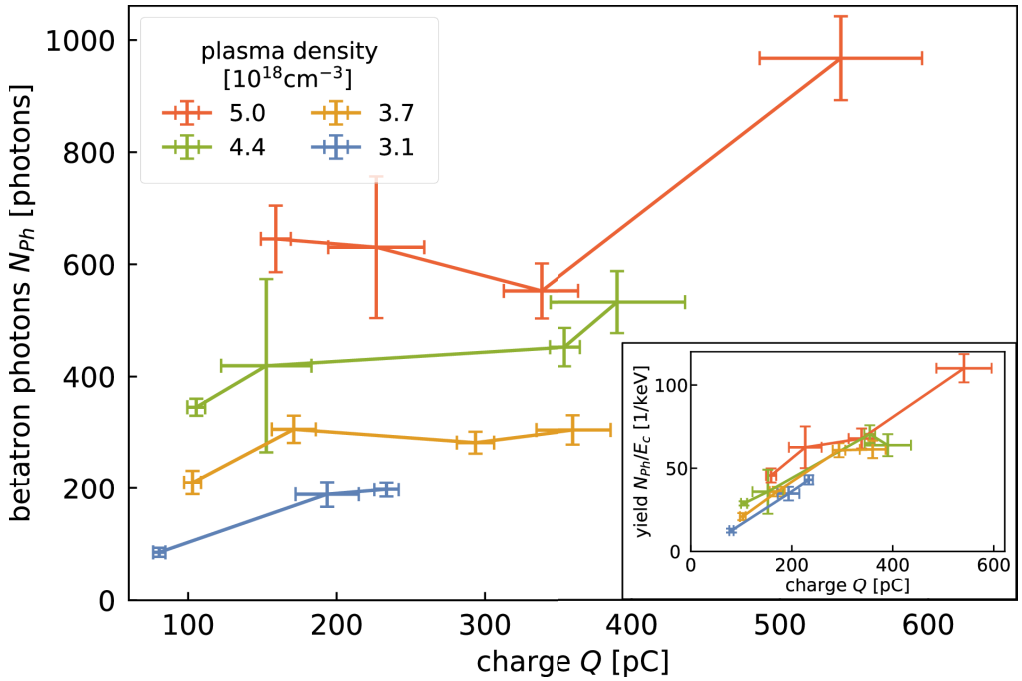

Figure 6.5.: **Betatron photon number N_{Ph} and betatron yield $N_{\mathrm{Ph}}/E_{\mathrm{c}}$:** The number of photons recorded with the detector increases with charge and plasma density. The inset shows the betatron yield, which is the photon number normalized by the critical energy.

tion facilitates the diagnostic of the bunch radius. In the case of betatron radiation, the bunch size at the end of acceleration is directly proportional to the betatron radius [150].

The method described in section 5.2 was applied to extract the betatron parameters. However, some shots were removed from the data sets because of strong fluctuations in the recorded electron spectrum, i.e., large electron pointing, energy fluctuations, and the small collection angle of the betatron spectrometer. For improving the statistical significance, the previously shown data sets were extended with a fourth plasma density of $3.1 \times 10^{18}\,\mathrm{cm}^{-3}$. The new plasma density covers less than the half of the presented charge range and thus did not add any new characteristics to the previously shown energy, energy spread and divergence.

Figure 6.4 illustrates the betatron radius for different injected charges along with different plasma densities. The betatron radius shown in figure 6.4a demonstrates an almost constant behavior at 0.7 µm to 1.0 µm with a very weak tendency to grow with charge. As shown in chapter 3, the betatron radius varies during the acceleration process and can decrease adiabatically with energy gain. To reduce the energy dependency, a normalization of the radius is achieved by dividing by $\gamma^{1/4}$. The result is shown by figure 6.4b. The trend of increasing radius with charge seems to be conserved and no peak or dip linked with the charge of optimal beam loading is visible.

Figure 6.5 shows the number of detected betatron photons N_{Ph} versus bunch charge for different plasma densities. Higher plasma densities consistently produce higher photon numbers at the detector which can be caused by the higher electron energy as well as plasma density. As shown in chapter 5 higher electron energy, betatron radius or plasma density lead to a higher critical energy E_{c} and wiggler parameter K. Here, however, the dependence on r_β can be neglected since it varies only weakly in comparison with energy and density as shown before. Although K is directly proportional to the total photon number as given by equation (3.19), it cannot serve for normalization because the recorded yield is limited by quantum efficiency of the detector and transmission of the beamline. In contrast to that, E_{c} is linked to the average photon energy and can compare the collected energy that is filtered by quantum efficiency and transmission. The inset of figure 6.5 shows the betatron yield divided by E_{c}. A linear charge dependency is clearly visible and indicates an incoherent radiation source. The incoherent radiation can be explained by electrons independently oscillating inside the plasma channel.

6.2. INTERPRETATION AND DISCUSSION

The central question arising from figures 6.3 and 6.4 is what physical processes can cause the different behavior in $\gamma\sigma_\ominus$ and r_β. On the one hand, the normalized divergence shows a significant dip around the optimal beam charge. On the other hand, the betatron radius exposes no such feature at the same charge but remains almost constant. Both parameters can describe the transverse phase space (x, p_x) introduced in section 3.5. Degradation of the transverse phase space can be caused by beam decoherence from betatron phase mixing [98] as well as interaction with the laser pulse [101, 151], longitudinally varying or nonlinear focusing forces [99] and

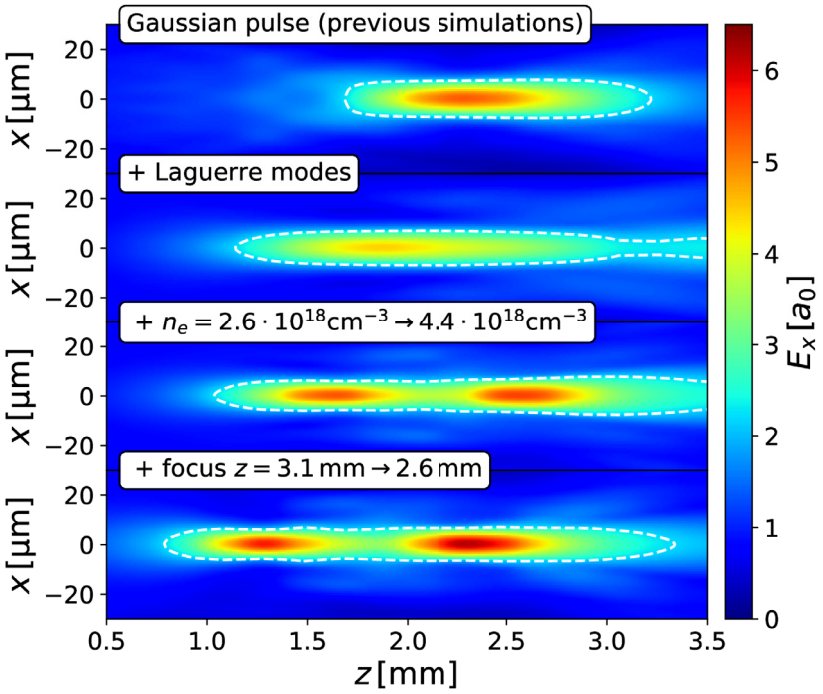

Figure 6.6.: **Focus evolution with optimized simulation setups:** Previous simulations [9] were modified for this thesis. The figure shows how the incremental steps toward the new simulation setup affected the laser evolution. Firstly, the laser pulse model was changed from a Gaussian pulse to a Laguerre pulse which results in the largest shift of the laser focus. Then, the plasma density was increased to the optimal conditions of the experiment. Eventually, the vacuum focus was optimized within the experimental accuracy.
The white dashed line denotes the threshold for ionization of the first K-shell electron of nitrogen (a_0 = 2.2, see section 2.1, table 2.1).

space charge effects [96]. The later will be addressed at the end of this section. This thesis focuses and explores betatron phase mixing [82, 98] as the cause of the minimum divergence at the optimal beam loading. For betatron phase mixing, high-energy electrons rotate slower than low-energy electrons in the transverse phase space, and thus advance slower in the betatron phase. The increase in the phase difference enlarges the occupied area in the phase space. In the case of maximum phase difference, the area becomes saturated and the beam reaches decoherence. In this case, the beam divergence reaches a maximum value. Before beam decoherence occurs, the phase space ellipse can still evolve, i.e. beam size and momentum spread, as shown below. For support of the hypothesis, simulations were performed to examine the six-dimensional phase space, which is typically not accessible by experiment.

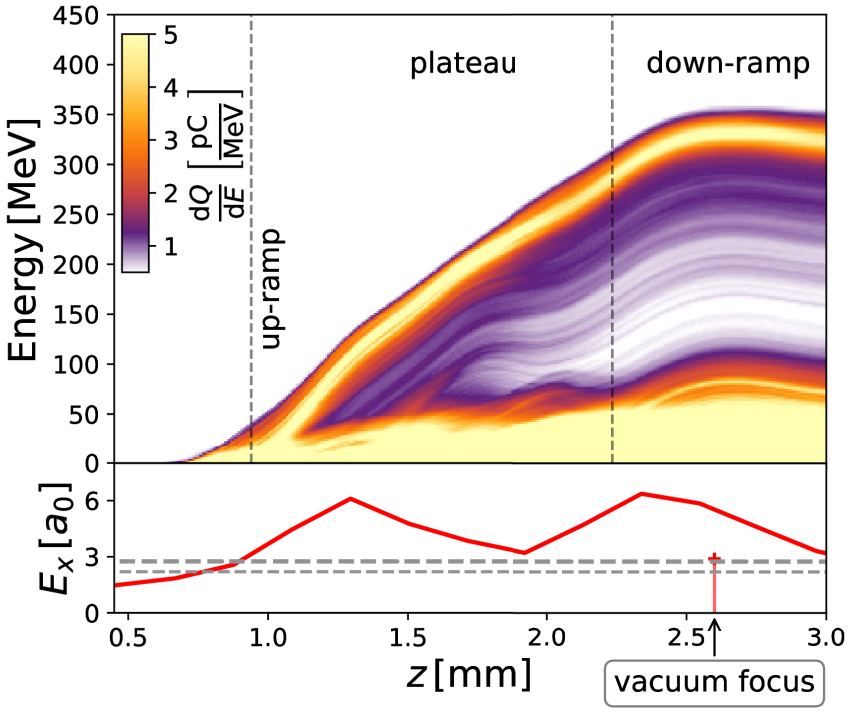

Figure 6.7.: **Energy evolution in simulation:** The top graph illustrates the evolution of the injected electrons originating from the K-shell of nitrogen. Density down-ramp injection of background plasma electrons is visible at the end of the gas jet. The bottom plot shows the corresponding normalized laser intensity. The gray horizontal dashed lines indicate the minimum potential for barrier suppression ionization of the two K-shells of nitrogen as discussed in section 2.1.

6.2.1. PHASE SPACE IN PICONGPU SIMULATIONS

Realistic experimental parameters were used to set up three-dimensional Particle-In-Cell (PIC) simulations running with the PIConGPU code [152, 153]. Previous simulations [9, 43] used an idealized three-dimensional Gaussian model for the laser pulse. During this thesis, new simulations were performed by Pausch as part of his Ph.D. thesis [154] which included some modifications (see appendix D). The incremental impact of these modifications on the evolution of the laser pulse is illustrated in figure 6.6. As shown in chapter 2, the evolution of the laser driver is imperative to the plasma accelerator. The major improvement is the better modeling of the laser pulse that agrees better with the experimental observations given in section 4.3. The new model consists of a Gaussian pulse distribution surrounded by higher Laguerre modes in the transverse plane. With the Laguerre modes, the focusing of the laser pulse in the plasma occurs faster and closer to the beginning of the density profile than with the Gaussian model. Additionally, the plasma density and the vacuum focus position were adjusted to the uncertainties of the experimental settings. The new laser pulse evolution results in an earlier injection and a longer acceleration length. The peak normalized laser intensity is larger by about 20 % and the accelerating field gradients are smaller than in previous simulations. In this thesis, only simulations

with aforementioned modifications were analyzed.

Figure 6.7 shows the energy evolution of the injected electrons. The vacuum laser focus was at $z = 2.6\,\mathrm{mm}$, i.e. in the density down-ramp. In plasma, the self-focusing effect leads to an earlier focus at $z = 1.3\,\mathrm{mm}$. Two injection types as described in section 2.5 are visible: The first injection is STII, occurs right behind the up-ramp of the density profile at $z = 1.1\,\mathrm{mm}$ and has a small energy spread. The total acceleration length is about 1.6 mm. The second injection occurs at the down-ramp, consisting of background plasma electrons. It is broadband and contributes to the low energy background of the electron spectrum. Altogether, the characteristics of the injections are highly consistent with the experimental observations, as shown before by the sample electron spectrum in figure 6.1.

In order to study the effect of different injected charges on the phase space, simulations with three different dopings were performed. However, the current implementation of the ionization model could not precisely reproduce the measured experimental charge. A typical approach for higher charges is adjusting the laser parameters such as normalized laser intensity or spot size. This unfavorable method would cause different injection conditions for different charges. To obtain comparable injection conditions for all charges, the simulated doping of N_2 was manually increased to match with the experimental results. This enabled a qualitative observation of beam loading effects as shown below, despite the fact that the experimentally obtained charge is not fully reached.

LONGITUDINAL PHASE SPACE AND ENERGY

Figure 6.8 shows an overview of the simulation results. The three simulations were performed with different nitrogen dopings and yielded charges of 108 pC, 118 pC and 136 pC within the FWHM of a quasi-monoenergetic peak. In figure 6.8a, the longitudinal phase space and the accelerating field are shown at the end of the acceleration. The bunch is visible for longitudinal momenta of larger than 250 MeV/c. The strong qualitative difference between the three bunches is the existence of the energy chirp. For the lowest charge in red, the electrons in the back of the bunch gained more energy than at the front. In contrast, the highest charge in blue exposes exactly the opposite feature: Electrons in the front of the bunch gained significantly more energy than in the back which can be attributed to the different accelerating field shown by the line plots in the same figure. The differences in energy chirp and accelerating field due to the bunch charge are the typical characteristics of beam loading. The median charge in green consistently merges the attributes of the both extrema.

In general, the longitudinal phase space presents the energy gain of the electrons. Immediately after trapping, the electrons gain energy and start to slip forward in the plasma cavity. As long as the injection continues, newly injected electrons fill up the phase space while already injected electrons are gaining energy. At this early stage, the electron in the bunch's head possess a larger energy because it had more time to gain energy. During the acceleration process, an electron at the back of the bunch gains energy at a faster rate than an electron at the front because of the typical linearity of the accelerating fields in LWFA. The energy spread can then be defined as the energy difference between front and back of the bunch. At some point, electrons

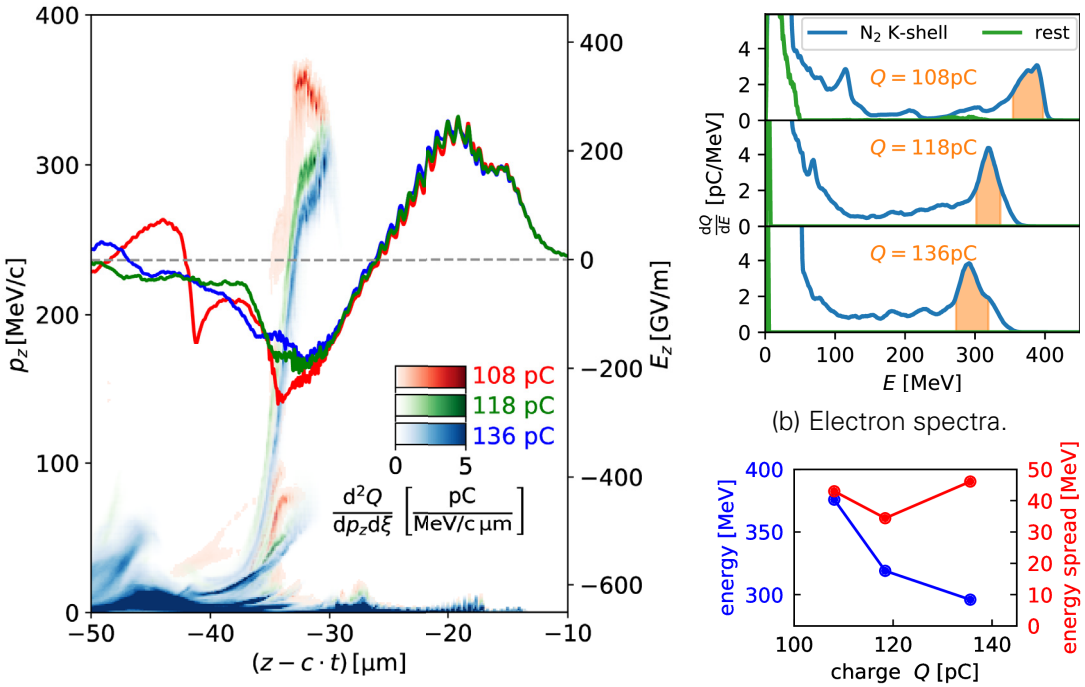

(a) Longitudinal phase space and accelerating field at z = 2.4 mm.

(b) Electron spectra.

(c) Energy and energy spread.

Figure 6.8.: **Overview of PIC simulations:** (a) illustrates the beam loading effect for the simulations with the highest and lowest injected charge. At the end of the plasma channel (z = 2.4 mm), the phase space (left axis, color scale) shows oppositely tilted electron bunches which can be caused by the different on-axis accelerating field (right axis, line plot). (b) shows the electron energy histograms of three simulations with 1 %, 3 % and 5 % nitrogen doping. (c) illustrates the charge dependency of energy and energy spread of the simulations shown in (b).

in the back gain the same energy as electrons at the front. Then, the energy spread becomes minimal. While the acceleration continues, the electron at the back gains more energy than the front and the energy spread increases again.

The three final electron spectra are shown in figure 6.8b. The bunch charge is marked by the orange area in the spectra which shift for higher charges towards lower energies. Furthermore, in figure 6.8c sums up the peak energy and energy spread. In parallel to the experimental results shown before, the energy decreases at higher charges while the minimum energy spread denotes optimal beam loading. This qualitatively demonstrates the effect of beam loading on the longitudinal phase space and agrees with the experimental observations of figure 6.2.

TRANSVERSE PHASE SPACE AND DIVERGENCE

For transverse beam parameters such as divergence and betatron radius, the dynamic in the transverse phase space is explored. Figure 6.9 illustrates the evolution of the injected electrons in the longitudinal and transverse phase space. The left column

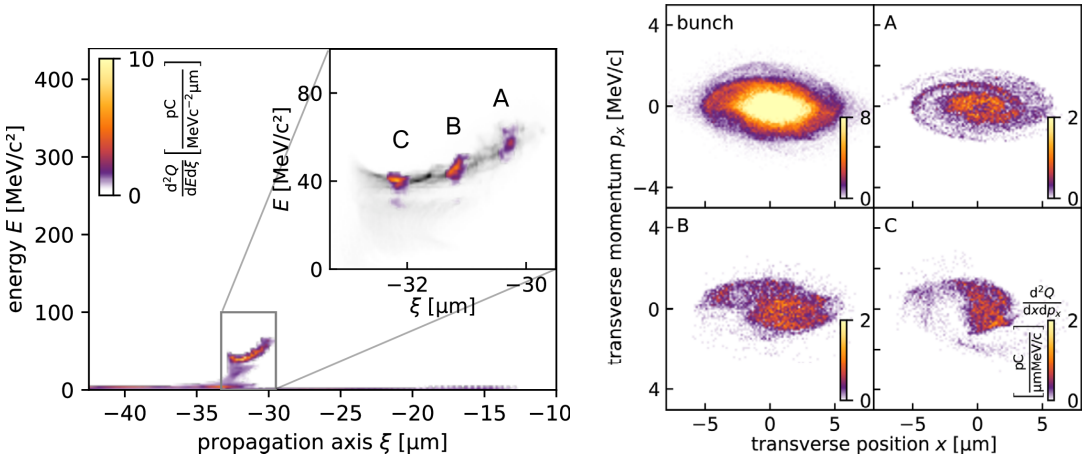

(a) Longitudinal and transverse phase space at z = 1.1 mm.

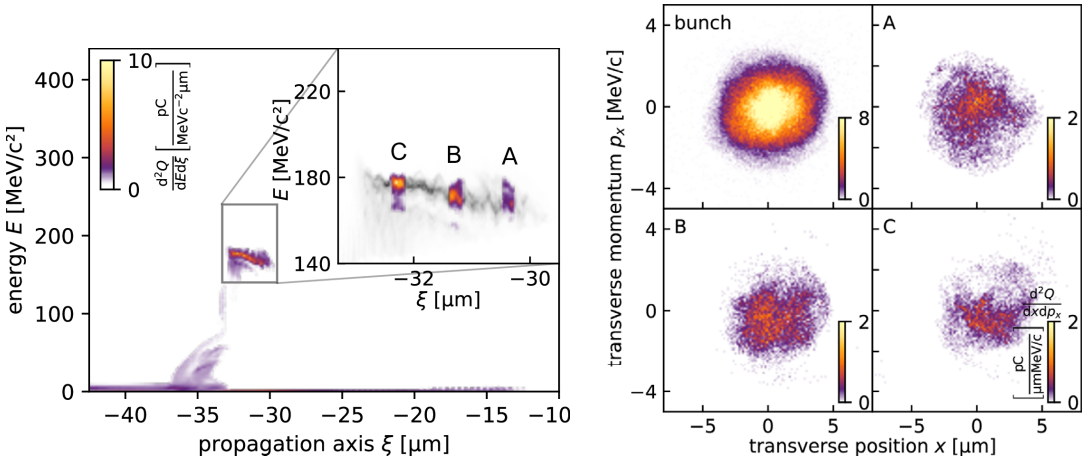

(b) Longitudinal and transverse phase space at z = 1.5 mm.

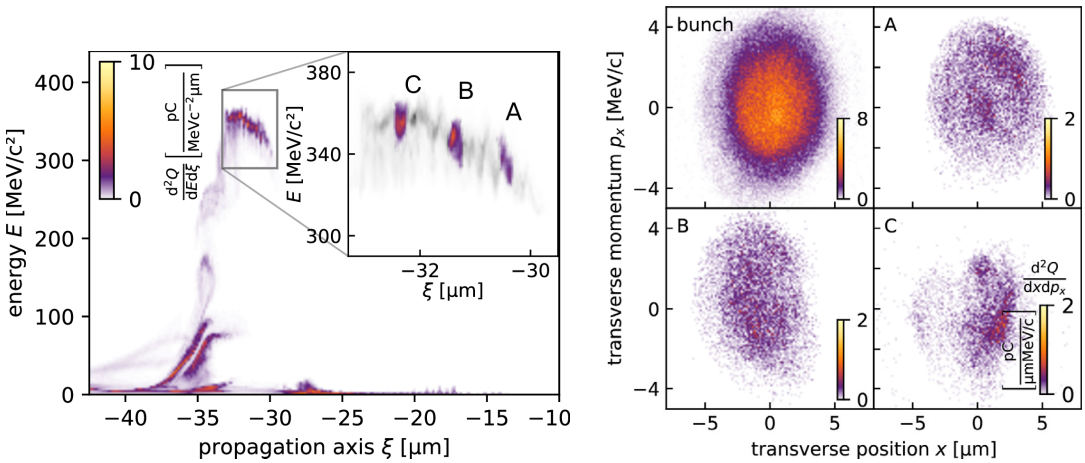

(c) Longitudinal and transverse phase space at z = 2.4 mm.

Figure 6.9.: **Betatron rotation in phase space:** The left column shows the K-shell electrons of nitrogen in the longitudinal phase space. In the zoom-in plots of the bunch, three populations with up to 6×10^5 macro-particles are selected at the head (A), center (B) and tail (C) of the bunch and traced along the simulation. The transverse phase space of these populations and the bunch is shown in the right column. The color scale of the transverse phase space is $\frac{d^2Q}{dxdp_x}$ in pC/(µmMeV/c).

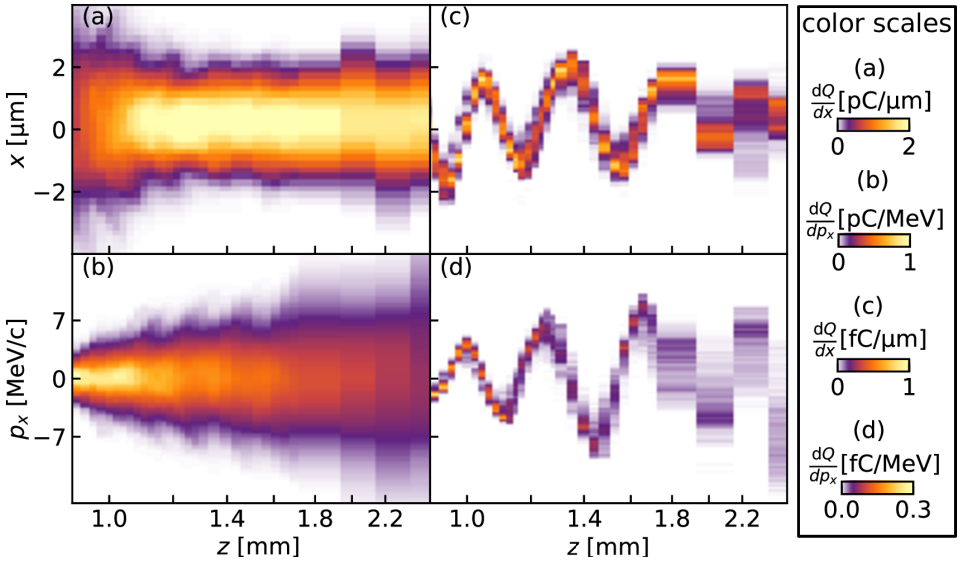

Figure 6.10.: **Temporal evolution of the transverse phase space:** The dynamic of the bunch (left column, (a)&(b)) and a fraction of macro-particles ((c)&(d)) with same parameters in space and momentum is shown for x and p_x. The z scale is mapped to logarithmic scale for a better visibility of the time dependent oscillations in x and p_x.

illustrates the longitudinal phase space (z, E). The horizontal axis is the laser propagation axis where the laser is propagating to positive values and the vertical axis is the particle energy. The right column shows the transverse phase space (x, p_x) in the plane of the laser polarization. The horizontal axis is the particle position and the vertical axis corresponds to the transverse momentum. To demonstrate the evolution of different beam parts, three slices of electrons in the bunch with a width of 0.3 µm were selected and traced by macro-particle identifiers through three different acceleration stages.

Figure 6.9a shows the phase space right after the completed injection. The electrons have been trapped at the back of the cavity and gained a relativistic energy of more than 30 MeV. At this acceleration stage, the electrons in the bunch's head (A) have a larger energy than electrons in the bunch's tail (C). In (x, p_x), the macro-particles are asymmetrically distributed which seems to be an effect of slightly asymmetric injections in the simulation.

As the electrons gain more energy, as shown in figure 6.9b, they climb higher in (z, E) and keep their relative longitudinal position inside the bunch because of the relativistic velocity. Electrons in (C) have gained the same energy as electrons in (A) and thus the energy along the bunch's length is almost constant. In the transverse phase space, caused by the focusing force discussed in section 2.7, the electrons have rotated as seen by different orientations of the populations. The rotation continues as illustrated by figure 6.9c until the end of the acceleration. Additionally, the electrons in (C) have gained more energy than in (A).

This rather discrete description of betatron rotations gives a limited view on the evolution of (x, p_x). Figure 6.10 shows the temporal evolution achieved with a higher

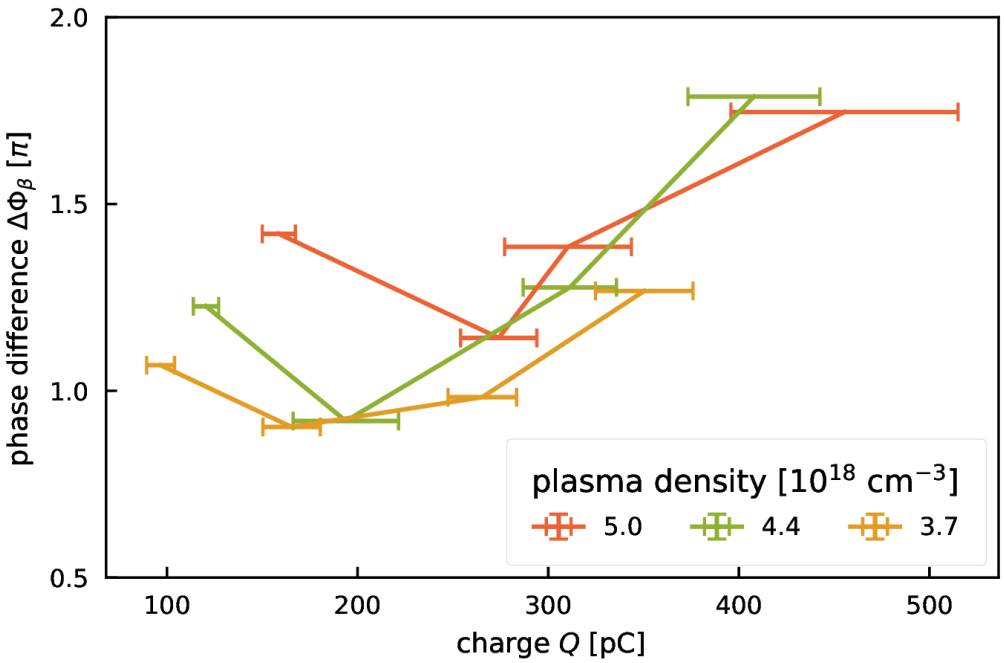

Figure 6.11.: **Phase difference over injected charge:** The phase difference $\Delta\phi_\beta$ was calculated from equation (3.42).

saving rate of time steps. Since the large file size of more than 100 GB per time step is challenging, the amount of saved data has to be carefully balanced with the required resolution. The temporal evolution of the bunch during acceleration inside the focusing channel is shown in figures 6.10a and 6.10b, showing periodic modulations along the acceleration which demonstrate that bunch decoherence is not yet completed. When full beam decoherence is reached in the plasma channel, then the periodic modulations should disappear. As shown by figures 6.10c and 6.10d, the periodic modulations can originate from the betatron oscillations of particle slices. The two subfigures show a fraction of macro-particles selected from the bunch with same energy, longitudinal position, transverse momentum and position. Near the end of the plasma channel with $z > 2$ mm, two effects degrade the temporal resolution. Firstly, the dumping rate of the simulation was decreased because of file system restrictions. Secondly, the macro-particles interact with the laser pulse, which deteriorates the quality of the selected fraction. This effect has to be addressed in the implementation of the field solver, which reproduces an unphysical laser speed and thus eases resonance conditions for laser-bunch interactions.

6.2.2. BUNCH DECOHERENCE AND PHASE DIFFERENCE

Decoherence of an electron bunch means that the evolution in the transverse phase space is completed, i.e., the shape and area of the phase space occupied by the bunch are saturated, as discussed in section 3.5. As mentioned there, bunch decoherence

can already occur at the injection when the injection time is longer than π/ω_P. In our experiments, π/ω_P is typically larger than 24 fs and thus longer than the bunch length of about 5 fs [5, 9]. Therefore, decoherence should not occur at the time of injection. However, decoherence can also occur after a sufficient acceleration length which can be estimated by the decoherence length L_{dc} given by equation (3.36). For the experiment, L_{dc} is larger than 1.7 mm (see figure C.2 in appendix) and so decoherence would not be reached by a typical acceleration length of 1.6 mm as mentioned above. Additionally, the smaller energy spread shown before in figure 6.2 typically implies a longer decoherence length at the optimal beam loading range.

A more detailed discussion of bunch decoherence can be gained by estimating the phase difference $\Delta\phi_\beta$ between the highest to the lowest energy electrons. As discussed in section 2.7, the linear focusing force rotates electrons in the transverse phase space by the angle Φ_β given by equation (3.22). For the typical bunch with an energy chirp as shown by the simulations, the maximum phase difference can exist between electrons with the highest and the lowest energy and it can provide a quantitative measure for the degree of decoherence. Figure 6.11 illustrates $\Delta\phi_\beta$ calculated with equation (3.42) for the data sets with the minimum normalized divergence. The values range from $0.8\,\pi$ to $1.7\,\pi$. Typically, decoherence requires a phase difference of larger than π for symmetric injection volumes in the transverse phase space. Injections that are asymmetric in the phase space can increase this to up to 2π by requiring a full 360° rotation in (x, p_x) of the bunch. Hence, beam decoherence can be shifted to larger phase differences than π.

As shown by figures 6.3 and 6.11, the minimum normalized divergence and the minimum phase difference are visible around a charge from 250 pC to 300 pC. The minimum in phase difference is visible at around 250 pC which is close to the optimal charge for beam loading discussed in this thesis. The small 50 pC deviation between the minima can be explained by the complex phase mixing process which can cause a mismatch of phase difference and obtained transverse momentum [95].

6.2.3. EXCLUSION OF POTENTIAL PHYSICAL PROCESSES

The beam divergence was not measured directly inside the plasma cavity but after the transition from plasma to vacuum and a drift space. Different densities were obtained as explained in section 4.3 by applying different pressures to the gas nozzle. The length of the down-ramp also depends on the applied backing pressure and thus on the plasma density. When the down-ramp length is comparable to the betatron wavelength, the beam divergence adiabatically shrinks and the beam size expands [26].

For the experiment, the length of the down-ramp was ~0.5 mm and the betatron wavelength was estimated to be between 0.5 mm to 0.8 mm which indicates that both parameters are within the same range. However, in general, effects for different densities can be excluded since all data sets were compared and discussed for the same plasma density. In this case, the down-ramp length is kept constant for the discussed data points and the betatron wavelength varies only weakly.

The figure of merit of the phase space is the normalized emittance discussed in

section 3.5. With the shown data for normalized divergence and betatron radius, the uncorrelated emittance can be estimated by equation (3.43). Using the direct proportionality $r_b = r_\beta/\sqrt{2}$ [150] yields a beam size of 0.5 µm to 0.7 µm and a normalized emittance of 2 mm mrad to 4 mm mrad which is comparable with typical values for LWFA [94]. The space charge explosion at the plasma-vacuum boundary can be ruled out by considering the betatron source size measurements and, again, comparing the normalized divergence at one plasma density.

If space-charge was the dominant factor for the beam divergence, then one would expect, for the same initial beam size at the accelerator exit, a monotonic increase of the divergence as the beam charge becomes higher. Furthermore, a smaller normalized divergence could be caused by a larger spot size, but this is not visible in the data, particularly at the charge where the optimum beam loading condition is reached. Additionally for the drift space between plasma exit and electron spectrometer, as pointed out in section 3.5, space charge effects are more dominant for beams with ultra-high currents larger than 17 kA at low energies. While a current of 20 kA [9] is estimated for the experiments, the peak bunch energies are too high according to equation (3.33) to introduce such a significant change in the normalized divergence.

Electrons can gain transverse momentum when they are interacting with the electric field of the laser pulse, as recently shown [101]. The momentum gain requires an overlap in time and space together with resonantly laser-driven betatron oscillations [151]. The simulations indicate an interaction between accelerated electrons and laser pulse. But this is a result from the unphysical behavior of the simulated group velocity of the laser pulse due to the field solver [155].

The spatiotemporal overlap can be expressed by a dimensionless pulse length parameter $T = c\tau_{\text{laser}}/\Lambda$ [100], where τ_{laser} is the laser pulse length and $\Lambda \simeq \sqrt{a_0}\lambda_P$ [100] is the length of the first bucket with the plasma wavelength λ_P. For the experiments shown here, $\tau_{\text{laser}} = 30$ fs (or 9 µm) and Λ is larger than 23 µm for all plasma densities. The parameter T is always smaller than 0.5 and injected electrons do not overlap with the laser pulse. Thus, the injected bunch should not interact with the laser pulse.

As shown in section 3.5, focusing forces that are not linear or depend on the longitudinal beam axis can deteriorate the transverse beam parameters. Linear wakefields have varying focusing forces along the propagation axis. However in the bubble regime, the focusing field is linear and independent of the longitudinal position in the cavity. As shown by figures 2.6, 2.7 and 2.8, the focusing force remains linear even with injection of a large charge.

6.3. SUMMARY

Electron energy, energy spread and normalized divergence were shown for three different plasma densities with bunch charges up to 0.5 nC. Energy and energy spread showed significant characteristics of beam loading consistent with the theoretical predicted value of 300 pC. The normalized divergence was shown to range from 4 rad to 5.7 rad and at the same charge where optimal beam loading minimizes the energy spread, the normalized divergence was found to decrease by up to 20 %.

Betatron radius and yield were analyzed with the same data set extended by a fourth plasma density for improved statistical significance. The betatron radius ranged from 0.7 µm to 1 µm and indicated no dependence on the charge for optimal beam loading such as seen before for energy, spread and divergence. Combining divergence and betatron radius gives an estimate for the uncorrelated emittance of 2 mm mrad to 4 mm mrad. The incoherent origin of the betatron radiation was confirmed by looking at the linearity between charge and normalized yield.

PIC simulations based on the realistic experimental parameter agreed well with the qualitative observations of energy and energy spread. The longitudinal phase space and accelerating field followed the theoretical predicted behavior. The transverse phase space showed periodic modulations which could be related to betatron oscillations and bunch decoherence. The hypothesis, which was given to explain the minimum divergence, was formed based on decoherence caused by betatron phase mixing. The calculated phase difference of the bunch from $0.8\,\pi$ to $1.7\,\pi$ supported the hypothesis where a minimum phase difference close to optimal beam loading was observed. Other processes connected to the divergence could be successfully excluded, such as interaction with the laser pulse, space charge effects, and non-linear or position dependent focusing fields.

7. CONCLUSION AND OUTLOOK

The presented work is the first systematic experimental study on the transverse beam dynamics of LWFA operating in the beam loading regime, generating high charge electron beams within a quasi-monoenergetic peak. The deployed self-truncated ionization injection scheme has significantly improved shot-to-shot stability with tunable bunch charges up to nanocoloumbs. A typical injection duration much shorter than a plasma period allows for betatron phase mixing such that the evolution of the transverse phase space results in minimal beam divergences.

Here, it is shown that the optimal beam loading at 300 pC can result in up to 20 % less normalized beam divergence as well as the minimum energy spread. A hypothesis is given to explain the observation by betatron phase mixing [98, 105] of the phase space during acceleration and is supported by numerical simulations. Plasma accelerated beams with a small divergence and a small energy spread can significantly simplify the beam transport for specific beam applications. The small beam size of LWFA challenges standard diagnostics but can be deduced by utilizing betatron radiation. An upper limit of the betatron source size is estimated by Fresnel diffraction. By utilizing the spectral shape of the betatron radiation, the betatron radius is deduced to be constant at a typical value of 1 µm for the same data sets where the minimum divergence occurs. Combining the betatron radius and divergence, the uncorrelated normalized beam emittance is estimated to range from 2 mm mrad to 4 mm mrad, which is comparable with electron beams from conventional RF accelerators. Moreover, it is shown that the betatron yield is linearly proportional to the charge as expected from an incoherent radiation source. Other possible processes such as space charge effects, nonlinear or position-dependent focusing fields and interaction with the laser driver can be excluded.

An important next step will be the determination of the bunch length and longitudinal structure. The bunch length and charge together provide the peak current which is a crucial parameter for further applications of the LWFA bunch. The bunch length can be measured by the transition radiation (TR) spectrometer discussed in section 4.3.4. Omid Zarini implemented the spectrometer with a temporal resolution better than 0.4 fs for his Ph.D. project [111]. The most recent results returned a preliminary bunch envelope duration of ∼20 fs (FWHM) with ultrashort substructures of ∼1 fs [5, 111]. The spectrometer will allow further research on the bunch length and longitudi-

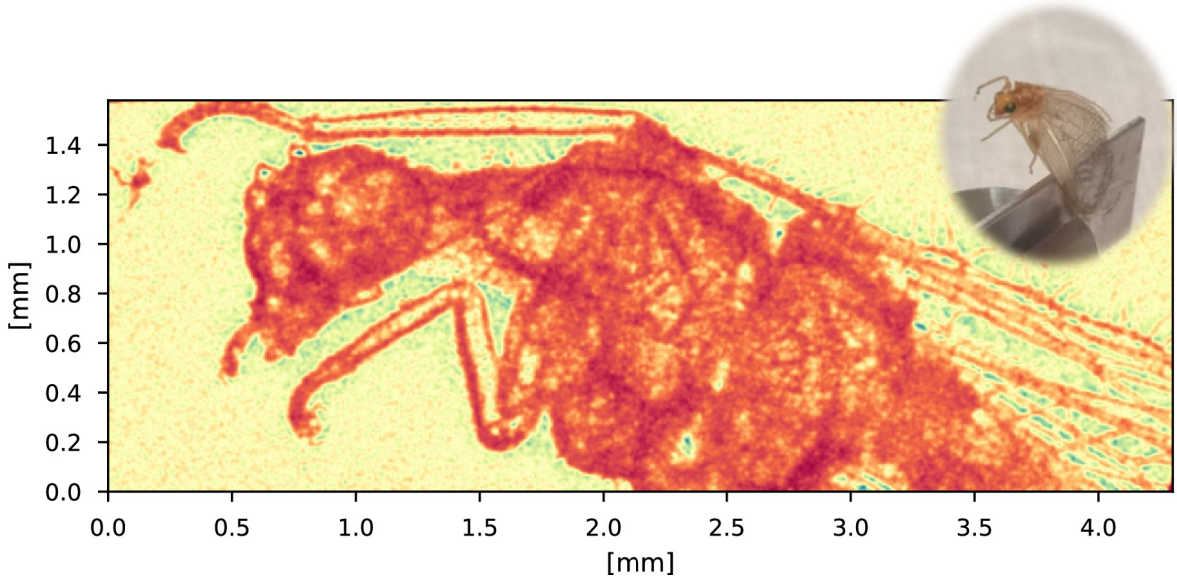

Figure 7.1.: **Radiography of biological samples:** The radiography of a Chrysopidae fly was taken with betatron radiation. The image is obtained by averaging over 21 consecutive shots with a plasma density of $3.1 \times 10^{18}\,\mathrm{cm}^{-3}$. The plasma medium was helium doped with 1 % nitrogen. The magnification on the CCD was 4.2×.

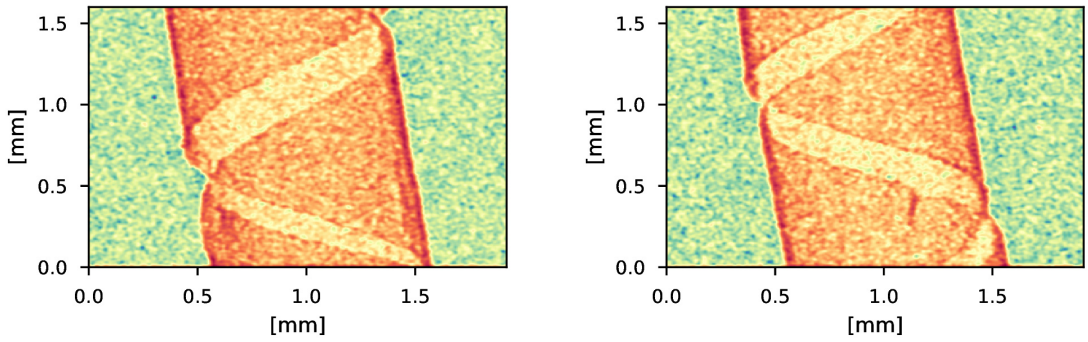

(a) Helix at original orientation.

(b) Helix rotated by 90°.

Figure 7.2.: **Radiography and tomography of a metal helix:** The helix is made of 6.5 µm thick aluminum foil with an inner diameter of ∼1 mm. The images show the average from 5 consecutive shots. The helix is turned by 90° between (a) and (b). The LPA was operated with helium doped with 1 % nitrogen as plasma medium with a density of $3.1 \times 10^{18}\,\mathrm{cm}^{-3}$. The magnification on the CCD was 4.2× and the repetition rate of a single shot was ∼0.1 Hz. Future high repetition targets [114] and laser systems may have the potential to speed up the tomography.

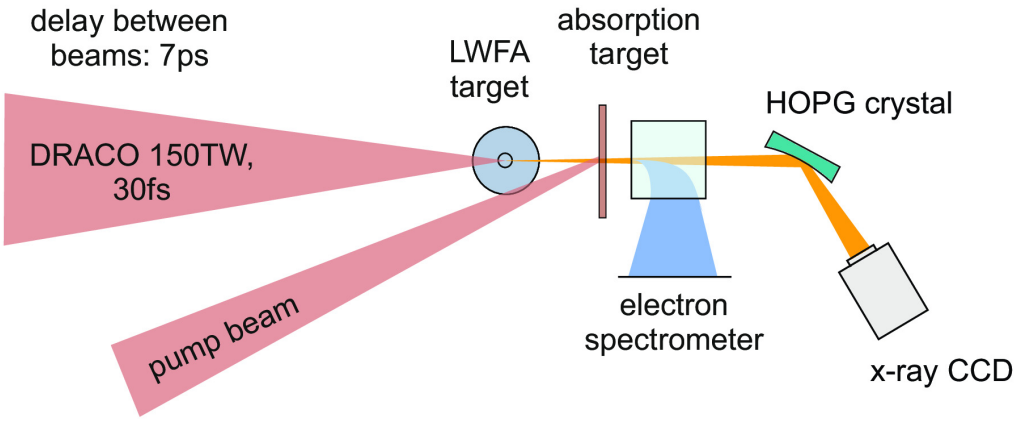

Figure 7.3.: **Schematic of an experiment with betatron radiation as a probe:** The 150 TW DRACO laser is focused on the LWFA target (gas jet target) to drive an LPA which creates the betatron radiation. Electrons are deflected by a magnetic dipole. The x-rays probing the absorption target are analyzed with the x-ray spectrometer. It consists of a Highly Oriented Pyrolytic Graphite (HOPG) and an x-ray detector. The absorption target can be heated by the pump pulse. The probing by the femtosecond short betatron radiation ensures a high temporal resolution.

nal structures as well as their dependencies on different acceleration conditions.

One remarkable feature of betatron radiation is the high photon flux in an ultrashort, femtosecond pulse with a broadband spectrum as shown in this work as well as by other groups before [85, 87, 127]. Figure 7.1 impressively demonstrates such high flux which is typically available during the experiments. Here, a fly is backlit by the betatron x-ray beam and an x-ray camera recorded the transmitted x-rays. As shown in figure 7.2, the stable betatron flux allows for an object to be imaged under various angles with reliable conditions. The figure shows an aluminum helix under two different angles acquired with the same experimental settings. After optimization of object and detector positioning, a similar setup can be utilized to perform tomography with an improved spatial resolution by phase contrast imaging, as demonstrated by Wenz et al. [42].

The broadband, high photon flux of betatron radiation is ideal for experiments that require a homogeneous flux within an energy bandwidth of ∼1 keV, e.g. absorption edge measurements. X-ray absorption spectroscopy (XAS) near an absorption edge can be utilized to obtain information about an element's electronic and ionic structure. The charge state and orbital occupancy can be accessed within ∼50 eV from the absorption edge by x-ray absorption near-edge spectroscopy. At a slightly higher energy offset of 50 eV to 1000 eV, the extended x-ray absorption fine structure enables access to the type and number of lattice neighbors as well as the bond distance.

Time-resolved spectroscopy of the absorption edge is typically applied in research of Warm Dense Matter (WDM) in the laboratory. WDM has a near solid density and temperatures ranging from 0.1 eV to 100 eV (10^3 K to 10^6 K). The wide span of thermodynamic conditions challenges the theoretical description. However, experiments investigating the equation of state and transport properties of WDM can lead to a

more detailed understanding, for example, for astrophysical objects [156]. The study of the WDM regime in the laboratory compliments the measurements from telescopes and space probes. Altogether, the gathered data can serve for modeling the inner structure and evolution of giant gaseous planets [157]. Possible other research fields are ultra-fast laser processes, solid-liquid-plasma phase transitions, correlated electron systems and high-pressure & shock physics.

The high pressures and temperatures of typical WDM experiments challenge experimental setups which are able to tolerate these conditions only temporarily and in a non-equilibrium state, i.e., using laser-driven shocks. For XAS, broadband pulses of picosecond duration from synchrotron facilities can be used. But studying the transient, non-equilibrium state requires femtosecond-short pulses for probing. Such short pulses can be produced by $K\alpha$ sources [40], which, however, have only a very limited spectral bandwidth [41]. In contrast, betatron radiation possesses both required attributes for a probing source. It has a femtosecond-short pulse duration and a synchrotron-like spectrum with a homogeneous flux of several keV.

Figure 7.3 illustrates a possible setup with betatron radiation probing an absorption target. The pump pulse can be a high power laser pulse, an intense x-ray pulse, electron or proton bunch [156]. The betatron beam would probe the heated or exposed target for measuring the absorption edge. Spectroscopy at the absorption edge is a powerful method for measuring the local electronic and atomic structure of a specimen but requires a highly resolved x-ray spectrum. The necessary resolution can be obtained by a novel diagnostic described by Smid et al. [158]. In the setup, highly oriented pyrolytic graphite crystals reflect and disperse x-rays while providing an energy resolution of better than 5 eV. More such experiments will become possible at the European XFEL (x-ray free-electron laser) which provides worldwide unique ultrashort and bright x-ray pulses. Several experimental setups for WDM experiments will be operated and contributed by the Helmholtz International Beamline for Extreme Fields (HIBEF) as an international user consortium.

One other aspect of laser-plasma acceleration is that it can provide a compact radiation source [159] which can ignite practical utilization as a driver for compact photon sources in the x-ray [36] and γ-ray [38] regions. The laser-accelerated electron bunches shown in this work possess a tremendous amount of charge and for optimized beam loading conditions a small energy spread and a minimal beam divergence. Further improvement of this beam parameters will facilitate beam transport [149] to specific applications, e.g., synchrotron light sources [36, 37] and FELs [160].

In summary, the utilization of a tailored injection scheme enabled a systematic study of the transverse beam divergence. The shown results are expected to be applied in the design of future plasma accelerators with strong intentions toward applications. Considerations about the minimum beam divergence achieved by an incomplete phase space mixing will become essential for future designs of LPA and beam transport lines.

Betatron radiation implemented as a source will allow investigations of new states of matter with high temporal resolution. Non-equilibrium states will be accessible by femtosecond short x-ray probe pulses and will allow the further exploration of the states of solid matter under high temperature and pressure in the WDM regime.

BIBLIOGRAPHY

[1] A. Köhler et al. "Minimizing betatron coupling of energy spread and divergence in laser-wakefield accelerated electron beams". In: *Physical Review Letters* (submitted).

[2] O. Zarini et al. "A Single-shot, ultra-broadband and highly sensitive spectrometer for short pulse, high resolution and low light diagnostic applications". In: (in preparation).

[3] J. P. Schwinkendorf et al. "Charge calibration of DRZ scintillation phosphor screens". In: *Journal of Instrumentation* (accepted).

[4] A. Lumpkin et al. "Observations of Coherent Optical Transition Radiation Interference Fringes Generated by Laser Plasma Accelerator Electron Beamlets". In: *IEEE conf. proc. of 18th AAC* (Aug. 2018), pp. 1–5. DOI: 10.1109/AAC.2018.8659381.

[5] O. Zarini et al. "Advanced Methods For Temporal Reconstruction Of Modulated Electron Bunches". In: *2018 IEEE Advanced Accelerator Concepts Workshop (AAC)* (Aug. 2018), pp. 1–5. DOI: 10.1109/AAC.2018.8659388.

[6] A. Irman et al. "Improved performance of laser wakefield acceleration by tailored self-truncated ionization injection". In: *Plasma Physics and Controlled Fusion* 60.4 (2018). ISSN: 13616587. DOI: 10.1088/1361-6587/aaaef1.

[7] J. M. Krämer et al. "Making spectral shape measurements in inverse Compton scattering a tool for advanced diagnostic applications". In: *Scientific Reports* 8.1 (Dec. 2018), p. 1398. ISSN: 2045-2322. DOI: 10.1038/s41598-018-19546-0.

[8] T. Kurz et al. "Calibration and cross-laboratory implementation of scintillating screens for electron bunch charge determination". In: *Review of Scientific Instruments* 89.9 (2018), p. 093303. DOI: 10.1063/1.5041755.

[9] J. P. Couperus et al. "Demonstration of a beam loaded nanocoulomb-class laser wakefield accelerator". In: *Nature Communications* 8.1 (Dec. 2017), p. 487. ISSN: 2041-1723. DOI: 10.1038/s41467-017-00592-7.

[10] T. Heinemann et al. "Investigating the Key Parameters of a Staged Laser- and Particle Driven Plasma Wakefield Accelerator Experiment". In: *Proceeding of IPAC2017* (2017).

[11] U. Schramm et al. "First Results with the Novel Peta-Watt Laser Acceleration Facility in Dresden". In: *Proc. of International Particle Accelerator Conference (IPAC'17), Copenhagen, Denmark, 14-19 May, 2017*. (Copenhagen, Denmark). International Particle Accelerator Conference 8. Geneva, Switzerland: JACoW, May 2017, pp. 48–52. ISBN: 978-3-95450-182-3. DOI: 10.18429/JACoW-IPAC2017-MOZB1.

[12] J. P. Couperus et al. "Tomographic characterisation of gas-jet targets for laser wakefield acceleration". In: *Nuclear Instruments and Methods in Physics Research, Section A: Accelerators, Spectrometers, Detectors and Associated Equipment* 830 (2015), pp. 504–509. ISSN: 01689002. DOI: 10.1016/j.nima.2016.02.099.

[13] A. Köhler et al. "Single-shot betatron source size measurement from a laser-wakefield accelerator". In: *Nuclear Instruments and Methods in Physics Research, Section A: Accelerators, Spectrometers, Detectors and Associated Equipment* 829 (2016), pp. 265–269. ISSN: 01689002. DOI: 10.1016/j.nima.2016.02.031.

[14] J.M. Krämer et al. "Bunch Arrival-Time Monitoring for Laser Particle Accelerators and Thomson Scattering X-Ray Sources". In: *Proceedings of IBIC2016, Barcelona, Spain* (2016), pp. 468–470. DOI: 10.18429/JACoW-IBIC2016-TUPG53.

[15] R. Pausch et al. "Computing Angularly-resolved Far Field Emission Spectra in Particle-in-cell Codes using GPUs". In: *Proc. 5th International Particle Accelerator Conference (IPAC'14), Dresden, Germany, June 15-20, 2014*. (Dresden, Germany). International Particle Accelerator Conference. Geneva, Switzerland: JACoW, July 2014, pp. 761–764. ISBN: 978-3-95450-132-8. DOI: 10.18429/JACoW-IPAC2014-MOPRI069.

[16] A. Köhler. "Charakterisierung von Plasmatargets für Laser Wakefield Experimente". Diploma thesis. Technische Universität Dresden, 2013.

[17] G. R. Werner. "Probing and modeling voltage breakdown in vacuum". PhD thesis. Cornell University, 2004.

[18] T. Tajima and J.M. Dawson. "Laser electron accelerator". In: *Physical Review Letters* 4.4 (1979), pp. 267–270.

[19] K. Nakajima et al. "A proof-of-principle experiment of laser wakefield acceleration". In: *Physica Scripta* 61.T52 (1994).

[20] S.P.D. Mangles et al. "Monoenergetic beams of relativistic electrons from intense laser–plasma interactions". In: *Nature* 431.7008 (Sept. 2004), pp. 535–538. ISSN: 0028-0836. DOI: 10.1038/nature02939.

[21] J. Faure et al. "A laser – plasma accelerator producing monoenergetic electron beams". In: *Nature* 431.September (2004), pp. 541–544. DOI: 10.1038/nature02900.1..

[22] C.G.R. Geddes et al. "High-quality electron beams from a laser wakefield accelerator using plasma-channel guiding". In: *Nature* 431.7008 (Sept. 2004), pp. 538–541. ISSN: 0028-0836. DOI: 10.1038/nature02900.

[23] X. Wang et al. "Quasi-monoenergetic laser-plasma acceleration of electrons to 2GeV." In: *Nat. Commun.* 4.May (2013), p. 1988. ISSN: 2041-1723. DOI: 10.1038/ncomms2988.

[24] W. P. Leemans et al. "Multi-GeV Electron Beams from Capillary-Discharge-Guided Subpetawatt Laser Pulses in the Self-Trapping Regime". In: *Physical Review Letters* 113.24 (Dec. 2014), p. 245002. ISSN: 0031-9007. DOI: 10.1103/PhysRevLett.113.245002.

[25] M. C. Downer et al. "Diagnostics for plasma-based electron accelerators". In: *Rev. Mod. Phys.* 90 (3 Aug. 2018), p. 035002. DOI: 10.1103/RevModPhys.90.035002.

[26] C.M.S. Sears et al. "Emittance and divergence of laser wakefield accelerated electrons". In: *Physical Review Special Topics - Accelerators and Beams* 13.9 (2010), p. 092803. ISSN: 10984402. DOI: 10.1103/PhysRevSTAB.13.092803.

[27] S. Wang et al. "X-Ray Emission from Betatron Motion in a Plasma Wiggler". In: *Physical Review Letters* 88.13 (Mar. 2002), p. 135004. ISSN: 0031-9007. DOI: 10.1103/PhysRevLett.88.135004.

[28] A. Rousse et al. "Production of a keV X-Ray Beam from Synchrotron Radiation in Relativistic Laser-Plasma Interaction". In: *Physical Review Letters* 93.13 (Sept. 2004), p. 135005. ISSN: 0031-9007. DOI: 10.1103/PhysRevLett.93.135005.

[29] S. Corde. "Des accélérateurs laser-plasma aux sources de rayonnement X femtoseconde: étude, développement et applications". PhD thesis. Ecole Polytechnique, 2012. URL: http://tel.archives-ouvertes.fr/pastel-00680257/.

[30] C. Thaury et al. "Angular-momentum evolution in laser-plasma accelerators". In: *Physical Review Letters* 111.13 (2013), p. 135002. ISSN: 00319007. DOI: 10.1103/PhysRevLett.111.135002.

[31] K. Ta Phuoc et al. "Imaging Electron Trajectories in a Laser-Wakefield Cavity Using Betatron X-Ray Radiation". In: *Physical Review Letters* 97.22 (Nov. 2006), p. 225002. ISSN: 0031-9007. DOI: 10.1103/PhysRevLett.97.225002.

[32] M. Schnell et al. "Characterization and application of hard x-ray betatron radiation generated by relativistic electrons from a laser-wakefield accelerator". In: *Journal of Plasma Physics* (2015), pp. 1–28. ISSN: 0022-3778. DOI: 10.1017/S0022377815000379. eprint: 1503.07304.

[33] A. Döpp et al. "Stable femtosecond X-rays with tunable polarization from a laser-driven accelerator". In: *Light: Science & Applications* 6.11 (Nov. 2017), e17086. ISSN: 2047-7538. DOI: 10.1038/lsa.2017.86.

[34] W. K. Röntgen. *Über eine neue Art von Strahlen: vorläufige Mitteilung*. Tech. rep. 1895. URL: http://cds.cern.ch/record/261889.

[35] J. Deisenhofer et al. "Structure of the protein subunits in the photosynthetic reaction centre of Rhodopseudomonas viridis at 3Å resolution". In: *Nature* 318.6047 (Dec. 1985), pp. 618–624. ISSN: 0028-0836. DOI: 10.1038/318618a0. eprint: /books.google.com/books?id=gRh-0dtTnf8C (https:).

[36] M. Fuchs et al. "Laser-driven soft-X-ray undulator source". In: *Nature Physics* 5.11 (2009), pp. 826–829. ISSN: 1745-2473. DOI: 10.1038/nphys1404.

[37] H.-P. Schlenvoigt et al. "A compact synchrotron radiation source driven by a laser-plasma wakefield accelerator". In: *Nature Physics* 4.2 (Feb. 2008), pp. 130–133. ISSN: 1745-2473. DOI: 10.1038/nphys811.

[38] K. Ta Phuoc et al. "All-optical Compton gamma-ray source". In: *Nature Photonics* 6.5 (May 2012), pp. 308–311. ISSN: 1749-4885. DOI: 10.1038/nphoton.2012.82. eprint: 1301.3973.

[39] N. D. Powers et al. "Quasi-monoenergetic and tunable X-rays from a laser-driven Compton light source". In: *Nature Photonics* 8.1 (Jan. 2014), pp. 28–31. ISSN: 1749-4885. DOI: 10.1038/nphoton.2013.314.

[40] M.M. Murnane et al. "Ultrafast X-ray Pulses from Laser-Produced Plasmas". In: *Science* 251.4993 (1991), pp. 531–536. DOI: 10.1126/science.251.4993.531.

[41] M. Suggit et al. "Nanosecond x-ray Laue diffraction apparatus suitable for laser shock compression experiments". In: *Review of Scientific Instruments* 81.8 (Aug. 2010), p. 083902. ISSN: 1089-7623. DOI: 10.1063/1.3455211.

[42] J. Wenz et al. "Quantitative X-ray phase-contrast microtomography from a compact laser-driven betatron source". In: *Nat. Commun.* 6.5 (2015), p. 7568. ISSN: 2041-1723. DOI: 10.1038/ncomms8568.

[43] J. P. Couperus. "Optimal beam loading in a nanocoulomb-class laser wakefield accelerator". PhD thesis. Technische Universität Dresden, 2018.

[44] A. Kramida et al. NIST Atomic Spectra Database (ver. 5.5), [Online]. Available: https://physics.nist.gov/asd [2017, November 1]. National Institute of Standards and Technology, Gaithersburg, MD. 2017.

[45] P. Gibbon. *Short pulse laser interactions with matter : an introduction /*. London : Imperial College Pr., 2005. ISBN: 9781860941351.

[46] D. Attwood and A. Sakdinawat. *X-Rays and Extreme Ultraviolet Radiation: Principles and Applications*. 2nd ed. Cambridge University Press, 2017. DOI: 10.1017/CBO9781107477629.

[47] E. Esarey et al. "Self-focusing and guiding of short laser pulses in ionizing gases and plasmas". In: *IEEE J. Quantum Electron.* 33.11 (1997), pp. 1879–1914. ISSN: 00189197. DOI: 10.1109/3.641305.

[48] A. Pukhov and J. Meyer-ter-Vehn. "Laser wake field acceleration: the highly non-linear broken-wave regime". In: *Appl. Phys. B Lasers Opt.* 74.4-5 (Apr. 2002), pp. 355–361. ISSN: 0946-2171. DOI: 10.1007/s003400200795.

[49] Eugene Hecht. *Optics*. 4th ed. Vol. 48. 1. Addison Wesley, 2002, p. 698. ISBN: 0-321-18878-0.

[50] M. Messmer. "Führung von Laserstrahlen hoher Intensität in Plasmakanälen". Master thesis. Technical University Dresden, 2014.

[51] G. Sun et al. "Self-focusing of short intense pulses in plasmas". In: *Physics of Fluids* 30.2 (1987).

[52] W. Lu et al. "Generating multi-GeV electron bunches using single stage laser wakefield acceleration in a 3D nonlinear regime". In: *Phys. Rev. Spec. Top. - Accel. Beams* 10.6 (2007), pp. 1–12. ISSN: 10984402. DOI: 10.1103/PhysRevSTAB.10.061301. eprint: 0612227 (physics).

[53] J. E. Ralph et al. "Self-guiding of ultrashort, relativistically intense laser pulses through underdense plasmas in the blowout regime". In: *Physical Review Letters* 102.17 (2009), pp. 1–4. ISSN: 00319007. DOI: 10.1103/PhysRevLett.102.175003.

[54] C. D. Decker et al. "The evolution of ultra-intense, short-pulse lasers in underdense plasmas". In: *Physics of Plasmas* 3.5 (1996), p. 2047. ISSN: 1070664X. DOI: 10.1063/1.872001.

[55] P. Sprangle, E. Esarey, and A. Ting. "Nonlinear theory of intense laser-plasma interactions". In: *Physical Review Letters* 64.17 (Apr. 1990), pp. 2011–2014. ISSN: 0031-9007. DOI: 10.1103/PhysRevLett.64.2011.

[56] E. Esarey, C. B. Schroeder, and W. P. Leemans. "Physics of laser-driven plasma-based electron accelerators". In: *Rev. Mod. Phys.* 81.3 (2009), pp. 1229–1285. ISSN: 00346861. DOI: 10.1103/RevModPhys.81.1229.

[57] J. B. Rosenzweig et al. "Acceleration and focusing of electrons in two-dimensional nonlinear plasma wake fields". In: *Physical Review A* 44.10 (1991). ISSN: 10502947. DOI: 10.1103/PhysRevA.44.R6189.

[58] A. Irman. "Integral design of a laser wakefield accelerator with external bunch injection". PhD thesis. 2009.

[59] S. Bulanov, F. Pegoraro, and J. Sakai. "Variety of nonlinear wave-breaking". In: *Nuclear Instruments & Methods in Physics Research Section a-Accelerators Spectrometers Detectors and Associated Equipment* 410.3 (1998), pp. 477–487. ISSN: 0168-9002. DOI: Doi10.1016/S0168-9002(98)00155-7.

[60] F. S. Tsung et al. "Near-GeV-Energy Laser-Wakefield Acceleration of Self-Injected Electrons in a Centimeter-Scale Plasma Channel". In: *Physical Review Letters* 93 (18 Oct. 2004), p. 185002. DOI: 10.1103/PhysRevLett.93.185002.

[61] K. Schmid et al. "Density-transition based electron injector for laser driven wakefield accelerators". In: *Phys. Rev. Spec. Top. - Accel. Beams* 13.9 (Sept. 2010), pp. 1–5. ISSN: 1098-4402. DOI: 10.1103/PhysRevSTAB.13.091301.

[62] A. Pak et al. "Injection and Trapping of Tunnel-Ionized Electrons into Laser-Produced Wakes". In: *Physical Review Letters* 104.2 (Jan. 2010), pp. 1–4. ISSN: 0031-9007. DOI: 10.1103/PhysRevLett.104.025003.

[63] C. McGuffey et al. "Ionization Induced Trapping in a Laser Wakefield Accelerator". In: *Physical Review Letters* 104.2 (Jan. 2010), pp. 1–4. ISSN: 0031-9007. DOI: 10.1103/PhysRevLett.104.025004.

[64] E. Oz et al. "Ionization-induced electron trapping in ultrarelativistic plasma wakes". In: *Physical Review Letters* 98.8 (2007), pp. 1–4. ISSN: 00319007. DOI: 10.1103/PhysRevLett.98.084801.

[65] M. Zeng et al. "Self-truncated ionization injection and consequent monoenergetic electron bunches in laser wakefield acceleration". In: *Physics of Plasmas* 21.3 (2014). ISSN: 10897674. DOI: 10.1063/1.4868404. eprint: 1312.5825.

[66] M. Mirzaie et al. "Demonstration of self-truncated ionization injection for GeV electron beams". In: *Scientific reports* (2015), pp. 1–9. ISSN: 2045-2322. DOI: 10.1038/srep14659.

[67] T. Katsouleas et al. "Beam Loading in Plasma Waves". In: *Particle Accelerators* 22.2 (1987), pp. 210–217. ISSN: 0093-3813. DOI: 10.1109/TPS.1987.4316687.

[68] S. van der Meer. *Improving the power efficiency of the plasma wakefield accelerator*. Tech. rep. CERN-PS-85-65-AA. CLIC-Note-3. Geneva: CERN, 1985. URL: https://cds.cern.ch/record/163918.

[69] M. Tzoufras et al. "Beam loading in the nonlinear regime of plasma-based acceleration". In: *Physical Review Letters* 101.14 (2008), pp. 1–4. ISSN: 00319007. DOI: 10.1103/PhysRevLett.101.145002. eprint: 0809.0227.

[70] M. Tzoufras et al. "Beam loading by electrons in nonlinear plasma wakes". In: *Physics of Plasmas* 16.5 (2009). ISSN: 1070664X. DOI: 10.1063/1.3118628.

[71] W. Lu et al. "Nonlinear theory for relativistic plasma wakefields in the blowout regime". In: *Physical Review Letters* 96.16 (2006), pp. 1–4. ISSN: 00319007. DOI: 10.1103/PhysRevLett.96.165002.

[72] C. E. Clayton et al. "Self-mapping the longitudinal field structure of a nonlinear plasma accelerator cavity". In: *Nature Communications* 7.X (2016), p. 12483. ISSN: 2041-1723. DOI: 10.1038/ncomms12483.

[73] W. K. H. Panofsky and W. A. Wenzel. "Some Considerations Concerning the Transverse Deflection of Charged Particles in Radio-Frequency Fields". In: *Review of Scientific Instruments* 27.11 (Nov. 1956), pp. 967–967. ISSN: 0034-6748. DOI: 10.1063/1.1715427.

[74] D. W. Kerst and R. Serber. "Electronic Orbits in the Induction Accelerator". In: *Phys. Rev.* 60 (1 July 1941), pp. 53–58. DOI: 10.1103/PhysRev.60.53.

[75] J.D. Jackson. *Classical electrondynamics*. 5th ed. John Wiley & Sons, 2005.

[76] *Lightsources.org*. https://lightsources.org/. Accessed: 2019-01-12.

[77] I. Kostyukov, A. Pukhov, and S. Kiselev. "Phenomenological theory of laser-plasma interaction in "bubble" regime". In: *Physics of Plasmas* 11.11 (2004), p. 5256. ISSN: 1070664X. DOI: 10.1063/1.1799371.

[78] J.D. Jackson. *Classical electrondynamics*. 3rd ed. John Wiley & Sons, 1999.

[79] E. Esarey et al. "Synchrotron radiation from electron beams in plasma-focusing channels". In: *Phys. Rev. E* 65.5 (May 2002), p. 056505. ISSN: 1063-651X. DOI: 10.1103/PhysRevE.65.056505.

[80] J. Schwinger. "On the Classical Radiation of Accelerated Electrons". In: *Physical Review* 75 (1949), pp. 1912–1925.

[81] S. Corde et al. "Femtosecond x rays from laser-plasma accelerators". In: *Reviews of Modern Physics* 85.1 (Jan. 2013), pp. 1–48. ISSN: 0034-6861. DOI: 10.1103/RevModPhys.85.1.

[82] A. G. Khachatryan et al. "Femtosecond electron-bunch dynamics in laser wakefields and vacuum". In: *Physical Review Special Topics - Accelerators and Beams* 10.12 (2007), pp. 1–13. ISSN: 10984402. DOI: 10.1103/PhysRevSTAB.10.121301.

[83] S.P.D. Mangles et al. "Laser-wakefield acceleration of monoenergetic electron beams in the first plasma-wave period". In: *Physical Review Letters* 96.21 (2006), p. 215001. ISSN: 00319007. DOI: 10.1103/PhysRevLett.96.215001.

[84] F. Albert et al. "Angular Dependence of Betatron X-Ray Spectra from a Laser-Wakefield Accelerator". In: *Physical Review Letters* 111.23 (Dec. 2013), p. 235004. ISSN: 0031-9007. DOI: 10.1103/PhysRevLett.111.235004.

[85] M. Schnell et al. "Deducing the electron-beam diameter in a laser-plasma accelerator using x-ray betatron radiation". In: *Physical Review Letters* 108.7 (2012), p. 075001. ISSN: 00319007. DOI: 10.1103/PhysRevLett.108.075001.

[86] F. Albert et al. "Betatron oscillations of electrons accelerated in laser wakefields characterized by spectral x-ray analysis". In: *Phys. Rev. E* 77.5 (May 2008), p. 056402. ISSN: 1539-3755. DOI: 10.1103/PhysRevE.77.056402.

[87] S. Kneip et al. "Observation of synchrotron radiation from electrons accelerated in a petawatt-laser-generated plasma cavity". In: *Physical Review Letters* 100.10 (2008), p. 105006. ISSN: 00319007. DOI: 10.1103/PhysRevLett.100.105006.

[88] S. Fourmaux et al. "Demonstration of the synchrotron-type spectrum of laser-produced Betatron radiation". In: *New Journal of Physics* 13 (2011). ISSN: 13672630. DOI: 10.1088/1367-2630/13/3/033017. eprint: 1104.2243.

[89] Y. Glinec et al. "Direct observation of betatron oscillations in a laser-plasma electron accelerator". In: *EPL (Europhysics Letters)* 81.6 (2008), p. 64001. ISSN: 0295-5075. DOI: 10.1209/0295-5075/81/64001.

[90] A. G. R. Thomas. "Scalings for radiation from plasma bubbles". In: *Physics of Plasmas* 17.5 (2010). ISSN: 1070664X. DOI: 10.1063/1.3368678.

[91] T. Matsuoka et al. "On electron betatron motion and electron injection in laser wakefield accelerators". In: *Plasma Physics and Controlled Fusion* 56.8 (2014), p. 084009. ISSN: 0741-3335. DOI: 10.1088/0741-3335/56/8/084009.

[92] R. Pausch et al. "How to test and verify radiation diagnostics simulations within particle-in-cell frameworks". In: *Nuclear Instruments and Methods in Physics Research Section A: Accelerators, Spectrometers, Detectors and Associated Equipment* 740 (Mar. 2014), pp. 250–256. ISSN: 01689002. DOI: 10.1016/j.nima.2013.10.073.

[93] R. Pausch. "Electromagnetic Radiation from Relativistic Electrons as Characteristic Signature of their Dynamics". In: (2012). DOI: 10.5281/zenodo.843510.

[94] G. R. Plateau et al. "Low-Emittance Electron Bunches from a Laser-Plasma Accelerator Measured using Single-Shot X-Ray Spectroscopy". In: *Physical Review Letters* 109.6 (Aug. 2012), p. 064802. ISSN: 0031-9007. DOI: 10.1103/PhysRevLett.109.064802.

[95] S. Humphries. *Charged particle beams*. New York, NY (USA); John Wiley and Sons Inc., 1990.

[96] M. Reiser. *Theory and Design of Charged Particle Beams*. Ed. by Martin Reiser. Weinheim, Germany: Wiley-VCH Verlag GmbH, Sept. 2004. ISBN: 9783527617623. DOI: 10.1002/9783527617623.

[97] R. Lehe. "Improvement of the quality of laser-wakefield accelerators: towards a compact free-electron laser". PhD thesis. 2014.

[98] P. Michel et al. "Radiative damping and electron beam dynamics in plasma-based accelerators". In: *Physical Review E - Statistical, Nonlinear, and Soft Matter Physics* 74.2 (2006), pp. 1–14. ISSN: 15393755. DOI: 10.1103/PhysRevE.74.026501.

[99] T. Mehrling et al. "Transverse emittance growth in staged laser-wakefield acceleration". In: *Physical Review Special Topics - Accelerators and Beams* 15.11 (2012), pp. 1–7. ISSN: 10984402. DOI: 10.1103/PhysRevSTAB.15.111303.

[100] J. L. Shaw et al. "Role of Direct Laser Acceleration of Electrons in a Laser Wakefield Accelerator with Ionization Injection". In: *Physical Review Letters* 118.6 (2017), p. 064801. ISSN: 10797114. DOI: 10.1103/PhysRevLett.118.064801.

[101] J. L. Shaw et al. "Experimental Signatures of Direct-Laser-Acceleration-Assisted Laser Wakefield Acceleration". In: *Plasma Physics and Controlled Fusion* 60.4 (Feb. 2018), p. 044012. ISSN: 0741-3335. DOI: 10.1088/1361-6587/aaade1.

[102] T. P. Wangler et al. "Relation between Field Energy and RMS Emittance in Intense Particle Beams". In: *IEEE Transactions on Nuclear Science* 32.5 (Oct. 1985), pp. 2196–2200. ISSN: 0018-9499. DOI: 10.1109/TNS.1985.4333859.

[103] S. Kneip et al. "Characterization of transverse beam emittance of electrons from a laser-plasma wakefield accelerator in the bubble regime using betatron x-ray radiation". In: *Phys. Rev. Spec. Top. - Accel. Beams* 15.2 (2012), p. 021302. ISSN: 10984402. DOI: 10.1103/PhysRevSTAB.15.021302. eprint: 1105.5559.

[104] S. Fritzler et al. "Emittance measurements of a laser-wakefield-accelerated electron beam". In: *Physical Review Letters* 92.16 (2004), pp. 165006–1. ISSN: 00319007. DOI: 10.1103/PhysRevLett.92.165006.

[105] X. L. Xu et al. "Phase-space dynamics of ionization injection in plasma-based accelerators". In: *Physical Review Letters* 112.3 (2014), p. 035003. ISSN: 00319007. DOI: 10.1103/PhysRevLett.112.035003.

[106] F. Gabriel et al. "The Rossendorf radiation source ELBE and its FEL projects". In: *Nuclear Instruments and Methods in Physics Research Section B: Beam Interactions with Materials and Atoms* 161-163 (2000), pp. 1143–1147. ISSN: 0168583X. DOI: 10.1016/S0168-583X(99)00909-X.

[107] M. Siebold et al. "PEnELOPE: a high peak-power diode-pumped laser system for laser-plasma experiments". In: *Proc.SPIE* 8780 (2013), pp. 8780–8780. DOI: 10.1117/12.2017522.

[108] A. Jochmann et al. "High Resolution Energy-Angle Correlation Measurement of Hard X Rays from Laser-Thomson Backscattering". In: *Physical Review Letters* 111.11 (Sept. 2013), p. 114803. ISSN: 0031-9007. DOI: 10.1103/PhysRevLett.111.114803.

[109] A. Jochmann. "Development and characterization of a tunable ultrafast x-ray source via inverse-compton-scattering". PhD thesis. Technische Universität Dresden, 2014.

[110] J. Krämer. "To be published". PhD thesis.

[111] O. Zarini. "Single-shot bunch duration measurement by using ultra broadband transition radiation spectrometer". PhD thesis. Technische Universität Dresden, 2019.

[112] D. Strickland and G. Mourou. "Compression of Ampified Chirped Optical Pulses". In: *Optics Communications* 55.6 (1985), pp. 447–449. ISSN: 00304018. DOI: 10.1016/0030-4018(85)90151-8.

[113] Y. Petit et al. "1-J white-light continuum from 100-TW laser pulses". In: *Physical Review A* 83.1 (Jan. 2011), p. 013805. ISSN: 1050-2947. DOI: 10.1103/PhysRevA.83.013805.

[114] I. Prencipe et al. "Targets for high repetition rate laser facilities: needs, challenges and perspectives". In: *High Power Laser Science and Engineering* 5 (July 2017), e17. ISSN: 2095-4719. DOI: 10.1017/hpl.2017.18.

[115] T. A. W. Wolterink. "High-gradient gas-jet targets for laser wakefield acceleration". Master Thesis. Twente, 2011.

[116] J. P. Couperus. "Master of Science Thesis Laser Wakefield Acceleration in the nonlinear bubble regime and Gas-jet target characterization Master of Science Thesis Laser Wakefield Acceleration in the nonlinear bubble regime and Gas-jet target characterization". Master Thesis. University of Twente, 2011.

[117] *VACODYM 764 TP VACUUMSCHMELZE GmbH & Co. KG*. 2018. URL: https://www.vacuumschmelze.de/en/products/permanent-magnets-assemblies/permanent-magnets/nd-fe-b/vacodym/vacodym-764-tp.html (visited on 05/25/2018).

[118] Pulsar Physics. *General Particle Tracer*. Version 3.01. URL: http://www.pulsar.nl/gpt.

[119] A. Buck et al. "Absolute charge calibration of scintillating screens for relativistic electron detection". In: *Review of Scientific Instruments* 81.3 (2010). ISSN: 00346748. DOI: 10.1063/1.3310275.

[120] A. D. Debus et al. "Electron bunch length measurements from laser-accelerated electrons using single-shot thz time-domain interferometry". In: *Physical Review Letters* 104.8 (2010), p. 084802. ISSN: 00319007. DOI: 10.1103/PhysRevLett.104.084802.

[121] S. I. Bajlekov et al. "Longitudinal electron bunch profile reconstruction by performing phase retrieval on coherent transition radiation spectra". In: *Physical Review Special Topics - Accelerators and Beams* 16.4 (2013), p. 040701. ISSN: 10984402. DOI: 10.1103/PhysRevSTAB.16.040701.

[122] O. Zarini. "Entwicklung eines breitbandigen optischen Spektrometers zur Pulsdauermessung ultrakurzer Elektronenpulse". Diploma Thesis. Technical University Dresden, 2013.

[123] S. Cipiccia et al. "Gamma-rays from harmonically resonant betatron oscillations in a plasma wake". In: *Nature Physics* 7.11 (Nov. 2011), pp. 867–871. ISSN: 1745-2473. DOI: 10.1038/nphys2090.

[124] F. Horst et al. "Nuclear Instruments and Methods in Physics Research A A TLD-based ten channel system for the spectrometry of bremsstrahlung generated by laser-matter interaction". In: *Nuclear Inst. and Methods in Physics Research, A* 782 (2015), pp. 69–76. ISSN: 0168-9002. DOI: 10.1016/j.nima.2015.02.010.

[125] S. Singh et al. "Compact high energy x-ray spectrometer based on forward Compton scattering for high intensity laser plasma experiments". In: *Review of Scientific Instruments* 89.8 (2018), p. 085118. DOI: 10.1063/1.5040979. URL: https://doi.org/10.1063/1.5040979.

[126] *IF-1 Beryllium High Purity Foil – Materion*. 2018. URL: https://materion.com/-/media/files/electrofusion/eqf3006_if1.pdf (visited on 05/25/2018).

[127] C. Fourment et al. "Broadband, high dynamics and high resolution charge coupled device-based spectrometer in dynamic mode for multi-keV repetitive x-ray sources." In: *Rev. Sci. Instrum.* 80.8 (Aug. 2009), p. 083505. ISSN: 1089-7623. DOI: 10.1063/1.3189004.

[128] *PIXIS-XO: 400B*. 9. Rev. N2. Princeton Instruments. June 2012.

[129] B. L. Henke, E. M. Gullikson, and J. C. Davis. "X-Ray Interactions: Photoabsorption, Scattering, Transmission, and Reflection at E = 50-30,000 eV, Z = 1-92". In: *Atomic Data and Nuclear Data Tables* 54 (July 1993), pp. 181–342. DOI: 10.1006/adnd.1993.1013.

[130] A. Higginbotham et al. "Single photon energy dispersive x-ray diffraction". In: *Review of Scientific Instruments* 85.3 (2014). ISSN: 10897623. DOI: 10.1063/1.4867456.

[131] E. I. Gorokhova et al. "Luminescence properties of ceramics based on terbium-doped gadolinium oxysulfide". In: *J. Opt. Technol.* 70.10 (Oct. 2003), pp. 693–698. DOI: 10.1364/JOT.70.000693.

[132] K. Zeil et al. "Absolute response of Fuji imaging plate detectors to picosecond-electron bunches". In: *Review of Scientific Instruments* 81.1 (2010). ISSN: 00346748. DOI: 10.1063/1.3284524.

[133] *Edmunds Optics | Acktar Light Absorbent Foil*. 2018. URL: https://www.edmundoptics.com/lab-production/general-tools/Acktar-Light-Absorbent-Foil/ (visited on 05/25/2018).

[134] R. Shah et al. "Coherence-based transverse measurement of synchrotron x-ray radiation from relativistic laser-plasma interaction and laser-accelerated electrons". In: *Phys. Rev. E* 74.4 (Oct. 2006), p. 045401. ISSN: 1539-3755. DOI: 10.1103/PhysRevE.74.045401.

[135] S. Kneip et al. "Bright spatially coherent synchrotron X-rays from a table-top source". In: *Nat. Phys.* 6.12 (Oct. 2010), pp. 980–983. ISSN: 1745-2473. DOI: 10.1038/nphys1789.

[136] P. Kirkpatrick. "On the Theory and Use of Ross Filters". In: *Review of Scientific Instruments* 10.6 (June 1939), pp. 186–191. ISSN: 0034-6748. DOI: 10.1063/1.1751523.

[137] D. Attwood. *Soft X-Rays and Extreme Ultraviolet Radiation: Principles and Applications*. Cambridge University Press, 1999. DOI: 10.1017/CBO9781139164429.

[138] J. W. Goodman. *Introduction to Fourier optics*. 3. ed. Englewood, Colo. : Roberts, 2005. ISBN: 9780974707723.

[139] F. Albert. "Rayonnement synchrotron base sur l'interaction laser-plasma en regime relativiste". Dissertation. Ecole Polytechnique Paris, 2009.

[140] K. Ta Phuoc. "Etude du rayonnement XUV produit lors de l'interaction relativiste entre un laser femtoseconde intense et un plasma d'hélium". PhD thesis. école Polytechnique, 2002.

[141] Y. Ueshima et al. "Laser Larmor X-ray radiation from low- Z matter". In: 17.1 (1999), pp. 45–58.

[142] R. Storn and K. Price. "Differential Evolution – A Simple and Efficient Heuristic for Global Optimization over Continuous Spaces". In: *Journal of Global Optimization* 11.4 (1997), pp. 341–359. ISSN: 09255001. DOI: 10.1023/A:1008202821328.

[143] F. Albert and A.G.R. Thomas. "Applications of laser wakefield accelerator-based light sources". In: *Plasma Physics and Controlled Fusion* 58.10 (2016), p. 103001. ISSN: 0741-3335. DOI: 10.1088/0741-3335/58/10/103001.

[144] F. Albert et al. "Laser wakefield accelerator based light sources: potential applications and requirements". In: *Plasma Phys. Control. Fusion* 56.8 (Aug. 2014), p. 084015. ISSN: 0741-3335. DOI: 10.1088/0741-3335/56/8/084015.

[145] K. Ta Phuoc et al. "Demonstration of the ultrafast nature of laser produced betatron radiation". In: *Phys. Plasmas* 14.8 (2007), p. 080701. ISSN: 1070664X. DOI: 10.1063/1.2754624.

[146] S. Corde et al. "Observation of longitudinal and transverse self-injections in laser-plasma accelerators." In: *Nat. Commun.* 4 (Jan. 2013), p. 1501. ISSN: 2041-1723. DOI: 10.1038/ncomms2528.

[147] F. Albert et al. "Observation of Betatron X-Ray Radiation in a Self-Modulated Laser Wakefield Accelerator Driven with Picosecond Laser Pulses". In: *Physical Review Letters* 118.13 (2017), p. 134801. ISSN: 0031-9007. DOI: 10.1103/PhysRevLett.118.134801.

[148] S. Becker et al. "Characterization and tuning of ultrahigh gradient permanent magnet quadrupoles". In: *Physical Review Special Topics - Accelerators and Beams* 12.10 (2009), p. 102801. ISSN: 1098-4402. DOI: 10.1103/PhysRevSTAB.12.102801. eprint: 0902.2371.

[149] T. André et al. "Control of laser plasma accelerated electrons for light sources". In: *Nature Communications* 9.1 (2018), p. 1334. ISSN: 2041-1723. DOI: 10.1038/s41467-018-03776-x.

[150] A. Curcio et al. "Trace-space reconstruction of low-emittance electron beams through betatron radiation in laser-plasma accelerators". In: *Physical Review Accelerators and Beams* 20.1 (2017), p. 012801. ISSN: 2469-9888. DOI: 10.1103/PhysRevAccelBeams.20.012801.

[151] K. Nemeth et al. "Laser-Driven Coherent Betatron Oscillation in a Laser-Wakefield Cavity". In: *Physical Review Letters* 100.9 (2008), p. 95002. ISSN: 0031-9007. DOI: 10.1103/PhysRevLett.100.095002.

[152] H. Burau et al. "PIConGPU: A Fully Relativistic Particle-in-Cell Code for a GPU Cluster". In: *IEEE Transactions on Plasma Science* 38.10 (Oct. 2010), pp. 2831–2839. ISSN: 0093-3813. DOI: 10.1109/TPS.2010.2064310.

[153] M. Bussmann et al. "Radiative Signatures of the Relativistic Kelvin-Helmholtz Instability". In: *Proceedings of the International Conference on High Performance Computing, Networking, Storage and Analysis*. SC '13. Denver, Colorado: ACM, 2013, 5:1–5:12. ISBN: 978-1-4503-2378-9. DOI: 10.1145/2503210.2504564.

[154] R. Pausch. "Synthetic radiation diagnostics as a pathway for studying plasma dynamics". PhD thesis. Technische Universität Dresden, 2019.

[155] K. Yee. "Numerical solution of initial boundary value problems involving maxwell's equations in isotropic media". In: *IEEE Transactions on Antennas and Propagation* 14.3 (May 1966), pp. 302–307. ISSN: 0018-926X. DOI: 10.1109/TAP.1966.1138693.

[156] K. Falk. "Experimental methods for warm dense matter research". In: *High Power Laser Science and Engineering* 6 (2018), e59. ISSN: 2095-4719. DOI: 10.1017/hpl.2018.53.

[157] D. Kraus et al. "Formation of diamonds in laser-compressed hydrocarbons at planetary interior conditions". In: *Nature Astronomy* 1.9 (2017), pp. 606–611. ISSN: 23973366. DOI: 10.1038/s41550-017-0219-9.

[158] M. Šmíd et al. "Highly efficient angularly resolving x-ray spectrometer optimized for absorption measurements with collimated sources". In: *Review of Scientific Instruments* 88.6 (2017). ISSN: 10897623. DOI: 10.1063/1.4986464. eprint: 1706.06403.

[159] F. Sylla et al. "Development and characterization of very dense submillimetric gas jets for laser-plasma interaction." In: *Rev. Sci. Instrum.* 83.3 (Mar. 2012), p. 033507. ISSN: 1089-7623. DOI: 10.1063/1.3697859.

[160] F. Grüner et al. "Space-charge effects in ultrahigh current electron bunches generated by laser-plasma accelerators". In: *Physical Review Special Topics - Accelerators and Beams* 12.2 (2009), p. 020701. ISSN: 10984402. DOI: 10.1103/PhysRevSTAB.12.020701.

[161] S. Kneip. "Laser Plasma Accelerator and Wiggler". Diss. Imperial College London, 2010.

[162] A. Huebl et al. *PIConGPU 0.3.0: Bremsstrahlung, EmZ, Thomas-Fermi, Improved Lasers, C++11*. June 2017. DOI: 10.5281/ZENODO.810041.

[163] A. Huebl et al. *PIConGPU 0.4.1: Minor Bugs and Example Updates*. Nov. 2018. DOI: 10.5281/ZENODO.1478937.

[164] J.P. Boris. "Relativistic Plasma Simulation - Optimization of a Hybrid Code". In: *Proc. 4th Conf. on Num. Sim. of Plasmas.* ADA023511. Naval Research Laboratory, Washington, D.C. http://www.dtic.mil/docs/citations/ADA023511/: Defense Technical Information Center, 1970, pp. 3–67.

[165] T.Zh. Esirkepov. "Exact charge conservation scheme for Particle-in-Cell simulation with an arbitrary form-factor". In: *Computer Physics Communications* 135.2 (2001), pp. 144–153. ISSN: 0010-4655. DOI: 10.1016/S0010-4655(00)00228-9.

[166] R. W. Hockney and J. W. Eastwood. *Computer Simulation Using Particles*. Bristol, PA, USA: Taylor & Francis, Inc., 1988. ISBN: 0-85274-392-0.

[167] P. Mulser and D. Bauer. *High power laser matter interaction*. Berlin; Heidelberg: Springer, 2010. ISBN: 9783540460657.

[168] N.B. Delone and V.P. Krainov. "Tunneling and barrier-suppression ionization of atoms and ions in a laser radiation field". In: *Physics-Uspekhi* 41.5 (1998), pp. 469–485. DOI: 10.1070/pu1998v041n05abeh000393.

Appendices

A. SINGLE PHOTON DETECTION AND PILE-UP EVENT CORRECTION

BACKGROUND SUBTRACTION

The recorded images are subtracted by a background image averaged over 50 shots with no detectable absorption events. This background is multiplied by the average count of pixels below the signal threshold of the recorded shot and divided by the background average.

SINGLE PHOTON DETECTION

When a photon is absorbed on a CCD, it deposits its energy in a charge cloud with a distinct radius. Depending on photon energy and impinging position, the charge signal is distributed over one or more adjacent pixels. An algorithm to detect such events was implemented as follows:

First, events that are identified as single photon absorption events are collected.

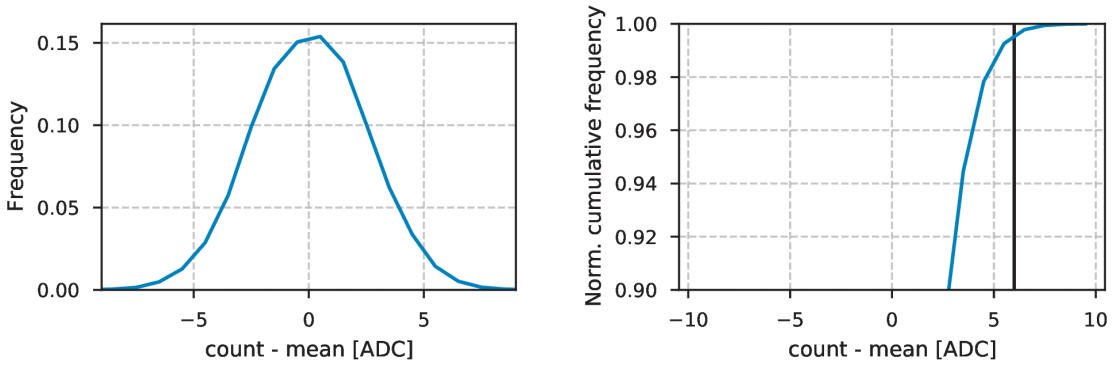

Figure A.1.: The frequency and cumulative frequency of the dark current of the CCD indicating a >99 % probability at 6 ADU.

Then, the value of every pixel of the recorded data is read out and compared with the signal threshold th_{sig}. Typically, th_{sig} = 15 Analog-Digital-Units (ADU) and it is the lower detection limit of the detector. Pixels below the threshold are discarded.

For pixels with values larger than the signal threshold the values of each of the eight adjacent pixel are compared with the noise threshold th_{noise}. Two standard deviations of the dark current gives th_{noise} = 6, as shown in figure A.1 with respect to the cumulative function. If all adjacent pixels are below the threshold, a single pixel event is appended to the list with the value of the pixel at the center. If not and all of the 18 surrounding pixel of the adjacent pixels are below the noise threshold, a multi pixel event is appended to the list with the pattern and sum of all pixel values above the noise level. The histogram of all of the detected events binned with energy calibrated counts then gives the detected raw x-ray spectrum.

PILE-UP EVENT CORRECTION

A pile-up of pixel absorption events occurs when two or more photons are absorbed by the same pixel or two adjacent pixels. This events are than detected as a single event with the sum of the photon energy of all contributing photons. A correction for pile-up events can become necessary because of the observed high flux of photons.

The pile-up correction work as follows: First, the pattern of all detected absorption events from one shot are loaded as a list and normalized to energy, i.e. 5 keV. Then, a virtual CCD with the same size as experimentally used. A Gaussian distributed dark current noise corresponding to the CCD is added. The impinging photons are simulated by adding entries from the pattern list at random positions. This process continues until the same number of pixels with a count above the signal threshold as in the experiment is reached. Then, the photon absorption detection algorithm compiles a synthetic spectrum. The synthetic spectrum has a peak at the normalized energy and pile-up peaks at a multiple of it. Typcally, pile-up events with more than the double energy are negligible. The pile-up factor f_{pileup} is the ratio of counts in the double energy peak and normalized energy peak.

The pile-up spectrum $\frac{\mathrm{d}N}{\mathrm{d}E}_{\text{pileup}}$ is calculated by summing all possible combinations of photon energies:

$$\frac{\mathrm{d}N}{\mathrm{d}E}_{\text{pileup}}(E) = \sum_i \frac{\mathrm{d}N}{\mathrm{d}E}_{exp}(E_i)\frac{\mathrm{d}N}{\mathrm{d}E}_{exp}(E_i - E)/N^2, \tag{A.1}$$

where N is the total number of detected events. Finally, the pile-up corrected spectrum $\frac{\mathrm{d}N}{\mathrm{d}E}_{corr}$ is calculated by subtracting the pile-up spectrum:

$$\frac{\mathrm{d}N}{\mathrm{d}E}_{corr}(E) = \frac{\mathrm{d}N}{\mathrm{d}E}_{exp}(E) - f_{\text{pileup}}N\frac{\mathrm{d}N}{\mathrm{d}E}_{\text{pileup}}(E) + \frac{2f_{\text{pileup}}}{N}\frac{\mathrm{d}N}{\mathrm{d}E}_{exp}(E). \tag{A.2}$$

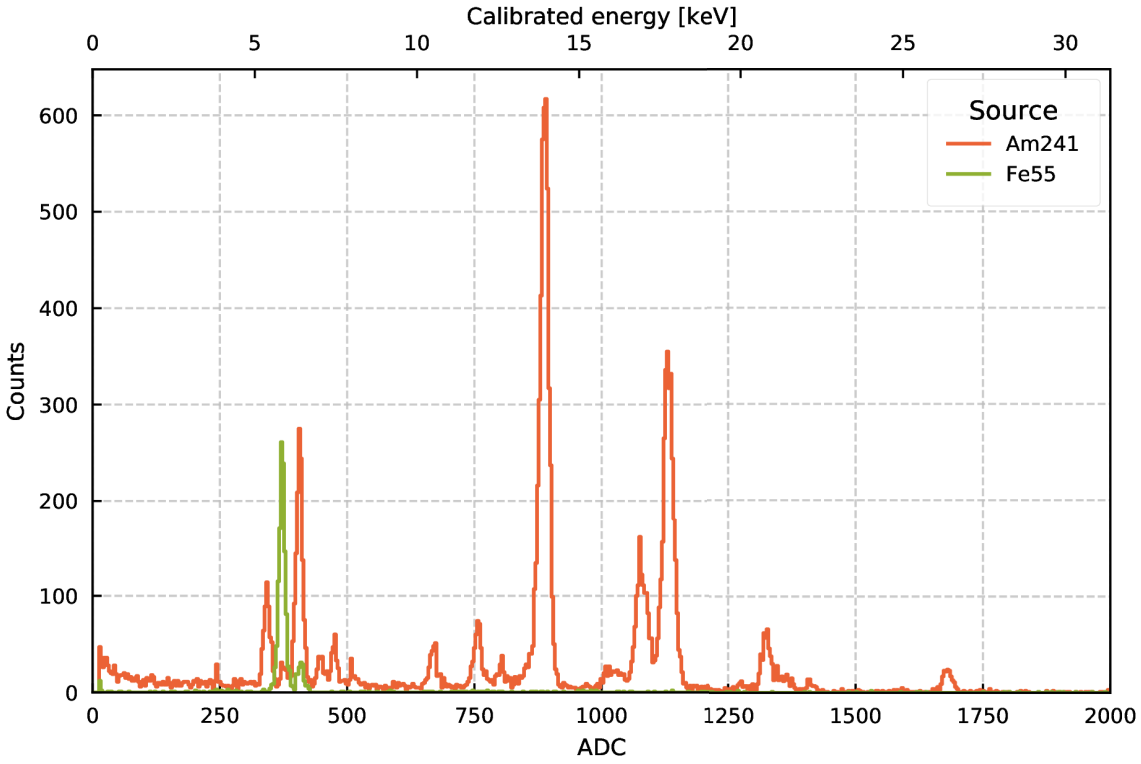

Figure A.2.: Calibration of Pixis CCD with Am-241 and Fe-55: The lower x-axis corresponds to counts from the analog-to-digital converter channel. The upper x-axis is obtained by the calibration using the peaks in the Am-241 spectrum.

PIXIS ENERGY CALIBRATION

The Pixis-XO camera was mounted to a small vacuum chamber, which supported a vacuum better than 1×10^{-6} mbar. The setup was placed in a radiation shielded area at the experimental cave 111c inside the ELBE building. No other artificial radiation sources were present and the natural radiation background was found to be negligible. The chip was cooled down to −75 °C. In front of the CCD was a light-tight x-ray window (14 µm Pokalon and 75 µm Kapton). The radioactive sources americium-241 and iron-55 were mounted separately on a lead block. Both sources were placed separately in front of the x-ray window. The corresponding background data was acquired with the same CCD settings by removing the source.

Figure A.2 presents the recorded spectra for the two different radioactive sources. The peaks in the Am-241 spectrum were used for calibration. The iron spectrum was used to estimate the energy resolution. The energy calibration is not different within the energy resolution for different pixel absorption events (single or multiple pixels). The energy resolution for single pixel events is better (150 eV) than for multiple pixel events (300 eV).

B. BACKLIT HALF-PLANE AND FRESNEL DIFFRACTION

EDGE SHADOW

A backlit half-plane can be utilized to quantify the size of the illuminating source. In the case of plane geometric optics and absence of Fresnel and Fraunhofer diffraction, the intensity variation perpendicular to the edge is given by the convolution of the backlit object with the source. Assuming a perfect half-plane as the backlit object represented by a step function in transmission and a Gaussian distribution with width σ of the source, this gives an intensity variation $I(y)$ on the detector [161]:

$$I(y) = \frac{1}{2}\left(1 + \operatorname{erf}\left(\frac{y}{M\sigma}\right)\right), \tag{B.1}$$

where M is the magnification of the setup and $\operatorname{erf}(x)$ is the error function.

FRESNEL DIFFRACTION

When an electromagnetic wave passes an aperture or edge and diffracts in the near-field, the diffraction pattern on a detector is called Fresnel diffraction. It depends on the wavelength λ of the wave, the distance v between diffracting object with characteristic size A and detector. The Fresnel regime requires a Fresnel number $F = A^2/(\lambda v)$ larger than 1.

Fresnel diffraction from an obstacle like a half-plane as shown in figure B.1 is well described in literature [49]. The electric field $\mathrm{d}E$ at a point P on a detector from a source S emitting spherical waves of wavelength λ diffracted at the position (x, y, z) is given by Fresnel-Kirchhoff equation:

$$\mathrm{d}E(P) = -\frac{K(\theta)E_0}{\lambda\rho r}\exp \mathrm{i}\left[k(\rho + r) - \omega t\right]\mathrm{d}\sigma, \tag{B.2}$$

where $k = 2\pi/\lambda$, $\omega = c/k$, t is the obstacle thickness, K is the Kirchhoff function,

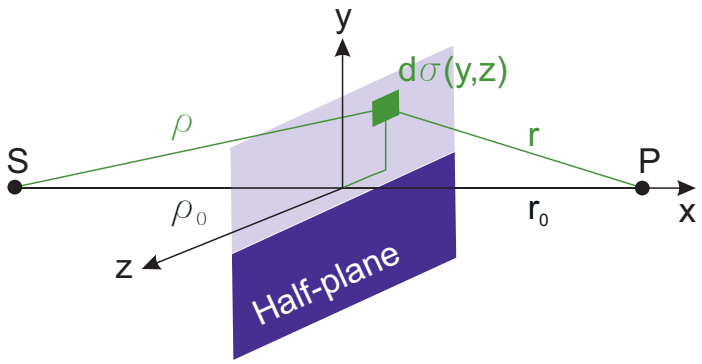

Figure B.1.: Sketch of Fresnel diffraction.

E_0 is the source strength and r, ρ are shown in Figure B.1. The amplitude can be estimated with small angle approximation ($K \approx 1$, $\rho \approx \rho_0$ and $r \approx r_0$) as $\frac{K(\theta)E_0}{\lambda\rho r} \approx \frac{E_0}{\lambda\rho_0 r_0}$, where ρ_0 and r_0 are the distances source-object and object-detector, respectively.

The phase needs to be more carefully handled. With the Pythagorean theorem for r and ρ and the sum of both rewritten as a binomial series expansion this gives:

$$\rho = \sqrt{\rho_0^2 + y^2 + z^2} \tag{B.3}$$

$$r = \sqrt{r_0^2 + y^2 + z^2} \tag{B.4}$$

$$\rho + r \approx \rho_0 + r_0 + (y^2 + z^2)\frac{\rho_0 + r_0}{2\rho_0 r_0} \tag{B.5}$$

and integration then gives:

$$E(P) = -\frac{E_0 \exp(-\mathrm{i}\omega t)}{\lambda\rho_0 r_0}\int_{-\infty}^{+\infty}\int_{y_0}^{+\infty}\exp(\mathrm{i}\left[k(\rho + r)\right])\mathrm{d}y\mathrm{d}z. \tag{B.6}$$

With the substitution:

$$u = y\sqrt{2\frac{\rho_0 + r_0}{\lambda\rho_0 r_0}} \tag{B.7}$$

$$v = z\sqrt{2\frac{\rho_0 + r_0}{\lambda\rho_0 r_0}} \tag{B.8}$$

the integral changes to:

$$E(P) = \frac{E_0}{2(\rho_0 + r_0)}e^{\mathrm{i}(k(\rho_0+r_0)-\omega t)}\int_{-\infty}^{+\infty}e^{\mathrm{i}\frac{\pi}{2}v^2}\mathrm{d}v\int_{w}^{+\infty}e^{\mathrm{i}\frac{\pi}{2}u^2}\mathrm{d}u. \tag{B.9}$$

The integral can be rewritten as Fresnel integrals[1]:

$$\int_0^w \mathrm{d}w' e^{\mathrm{i}\frac{\pi}{2}w'^2} = \mathcal{C}(w) + \mathrm{i}\mathcal{S}(w). \tag{B.10}$$

[1] They are defined as $\mathcal{C}(w) = \int_0^w \cos\frac{\pi}{2}x^2\mathrm{d}x$ and $\mathcal{S}(w) = \int_0^w \sin\frac{\pi}{2}x^2\mathrm{d}x$

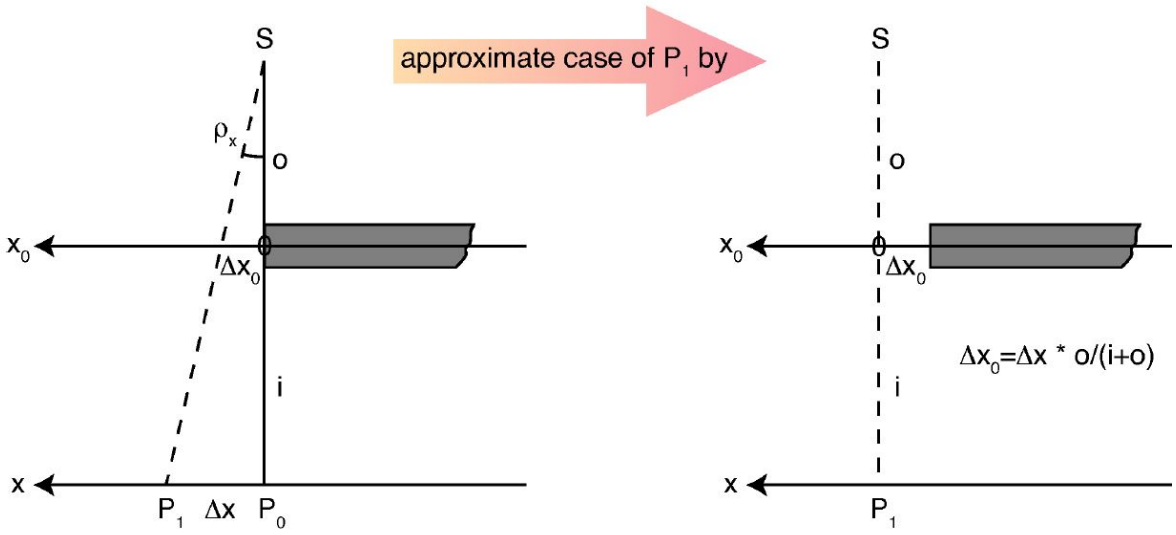

Figure B.2.: From [161].

So the integrals become:

$$\int_{-\infty}^{+\infty} e^{\mathrm{i}\frac{\pi}{2}v^2}\mathrm{d}v = 1 + \mathrm{i} \tag{B.11}$$

$$\int_{w}^{+\infty} e^{\mathrm{i}\frac{\pi}{2}u^2}\mathrm{d}u = 1 + \mathcal{C}(w) + \mathrm{i}\mathcal{S}(w) \tag{B.12}$$

$$\text{with } w = y_0\sqrt{2\frac{\rho_0 + r_0}{\lambda\rho_0 r_0}} \tag{B.13}$$

$$E(P) = \frac{E_0}{2(\rho_0 + r_0)} e^{\mathrm{i}(k(\rho_0+r_0)-\omega t)}(1 + \mathrm{i})(1 + \mathcal{C}(w) + \mathrm{i}\mathcal{S}(w)). \tag{B.14}$$

SMALL ANGLE APPROXIMATION

Equation (B.14) gives the electric field at point P as a function of the axis S-P. The formula becomes more complex for calculating all interesting points on the detection plane. So $E(y)$ and not $E(P)$ is interesting for the analysis. Instead, the S-P axis is kept constant and the position of the half plane is moved by Δy_0. This is effectively moving the diffraction pattern from point $P(x_0, y_0 + \Delta y, z_0)$ to $P(x_0, y_0, z_0)$, as shown in Figure B.2. The geometric magnification gives $\Delta y_0 = \Delta y \frac{\rho_0}{\rho_0+r_0}$ and thus the electric field may rewritten as:

$$E(P) = E(w(y)) \tag{B.15}$$

with $w(y) = y\frac{\rho_0}{\rho_0+r_0}\sqrt{2\frac{\rho_0+r_0}{\lambda\rho_0 r_0}}$.

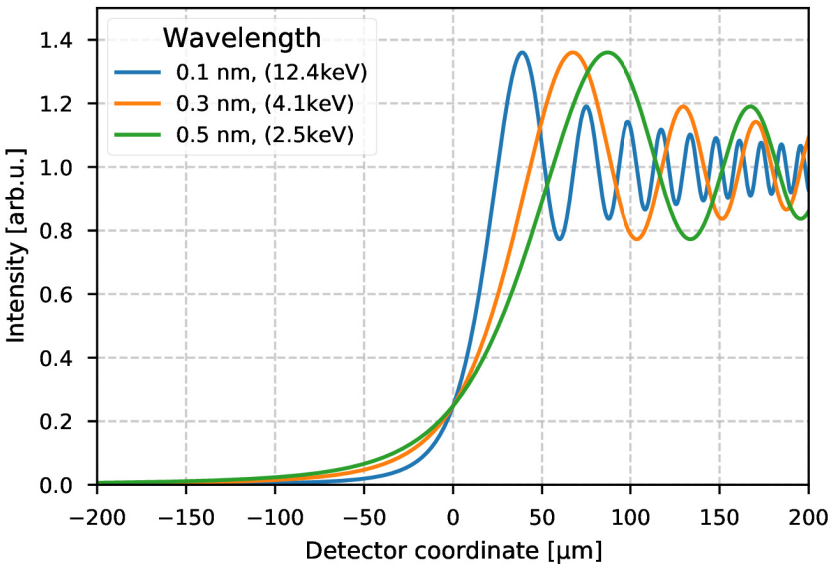

Figure B.3.: Theoretical intensity of an x-ray beam from a monochromatic point-like source diffracted by a half-plane. The distances between source, half-plane and detection plane are the same as the experimental conditions described in 5.1.2.

SOURCE SIZE AND SPECTRAL RESPONSE

For a source with non-negligible size and a broadband spectrum of wavelengths, the electric field must be convoluted with the source function $g(\xi)$ and spectral sensitivity $S(\lambda)$ of the detector:

$$E(y) = \int_{\xi}\int_{\lambda} \mathrm{d}\xi \mathrm{d}\lambda S(\lambda) g(\xi) E(\lambda, y - v/u\xi) \tag{B.16}$$

The detected intensity $I(y)$ is then:

$$I(y) = \frac{c\varepsilon_0}{2}|E(y)|^2, \tag{B.17}$$

where c is the speed of light in vacuum and ε_0 is the vacuum permittivity.

Figures B.3 and B.4 show numerically calculated intensity distributions for a monochromatic point-like source and polychromatic source with different sizes. The spectral distribution for different critical energies has a negligible effect on the intensity distribution. The spectral distribution is the same as in the experiment shown in chapter 5.

EDGE RECONSTRUCTION

Figure B.5 shows how the edge of the tantalum foil is reconstructed. The half-shadow images are background subtracted. For a better signal-to-noise ratio (SNR), the horizontal lineouts were integrated along the vertical oriented edge. The edge had a

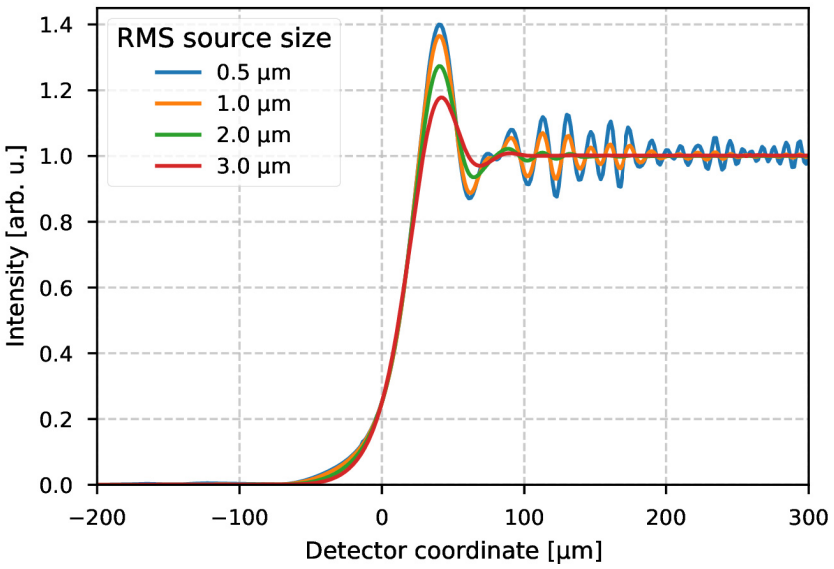

Figure B.4.: Theoretical intensity of a Fresnel diffracted source with different source sizes. The spectral response, the distances between source, half-plane and detection plane are the same as in figure B.3.

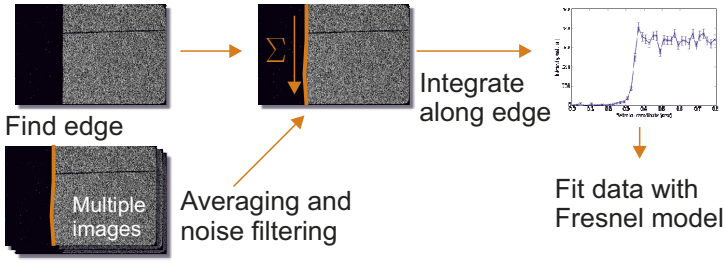

Figure B.5.: The workflow for reconstruction of the tantalum edge.

variation from a straight line of 2 pixel at maximum. To obtain the pixel exact horizontal position of the edge on the CCD, horizontal lineouts were fitted with equation (B.1). Averaged over the five brightest shots of the experimental campaign with 50 % to 80 % pixel occupancy, this gives the path for the vertical integration. Then the measured radiograph is integrated along the edge and the data is then used for further Fresnel analysis.

C. SUPPLEMENTARY FIGURES

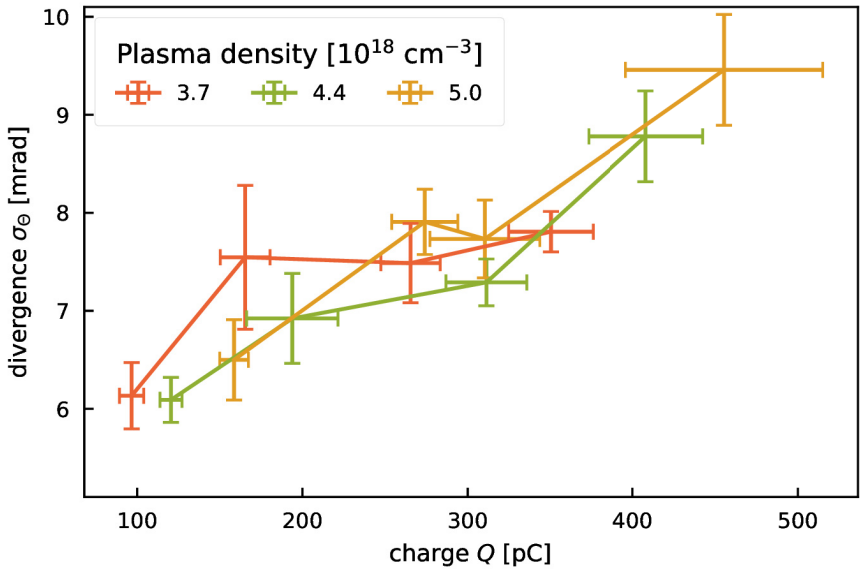

Figure C.1.: **Geometrical bunch divergence:** The geometric divergence σ_Θ of the electron beam is extracted from the nondispersive plane of the electron spectrometer as shown in figure 6.1. This plane is in parallel to the laser polarization axis. The data points correspond to figure 6.3 without normalization with the electron energy γ.

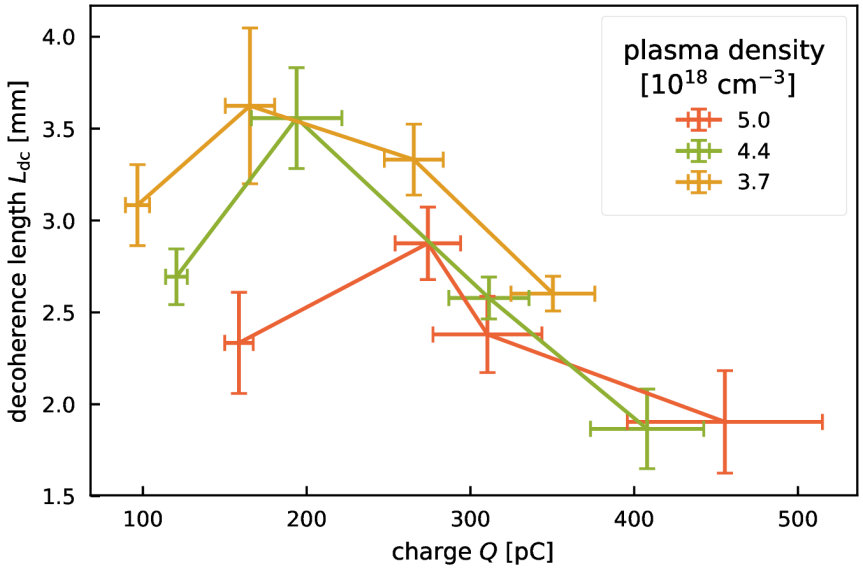

Figure C.2.: **Decoherence length:** The decoherence length L_{dc} is calculated by using equation (3.36) with the average electron energy within the FWHM of the charge and the mean energy. The error bars for the decoherence length are calculated by using the Gaussian error law and utilizing the shot-to-shot errors of the energy and energy spread and 1 % uncertainty on the plasma density.

D. PARTICLE-IN-CELL SIMULATIONS

Richard Pausch and Alexander Debus set up the particle-in-cell simulations using the versions 0.3.0-dev [162] and 0.4.1 [163] of PIConGPU [152].

The simulation frame had $768 \times 768 \times 2016$ cells with a resolution of $\Delta x = \Delta y = 265.8\,\text{nm}$ (transversely) and $\Delta z = 44.3\,\text{nm}$ (longitudinal). The temporal resolution was 143.68 as. The electromagnetic fields and macro-particles propagation were compiled with the field solver by Yee [155] and the particle pusher by Boris [164], respectively. The current was calculated with the Esirkepov deposition scheme [165] and a triangular shaped density cloud interpolation [166]. The simulations utilized BSI [167] and ADK [168] methods for ionization implementation.

Artificial increased N_2 doping enabled beam loading studies as shown in section 6.2. The plasma density model based on an experimentally determined density profile [12].

An 800 nm laser pulse was modeled using a Gaussian-Laguerre envelope in space and a Gaussian envelope in time which reached a vacuum peak intensity of $a_0 = 2.8$ at focus position. The pulse duration was 30 fs and the spot size was 19 µm (both at full-width-half-maximum in intensity).

All simulations were performed with activated particle identifiers, which allowed a particle tracking of injected electrons from the nitrogen K-shell.

EQUATIONS

Laser and plasma parameter

Plasma wavelength	$\lambda_P[\mu m] = 33.4/\sqrt{n_e[10^{18}cm^{-3}]}$
Normalized laser intensity	$a_0 = 0.855 \times \lambda_0[\mu m] \times \sqrt{I[10^{18}Wcm^{-2}]}$
Relativistic wavebreaking limit	$E_0[GV/m] = 96 \times \sqrt{n_e[10^{18}cm^{-3}]}$
Ponderomotive energy	$U_p[eV] = 0.93 \times I[10^{-15}Wcm^{-2}] \times \lambda_0^2[\mu m]$
Peak electric laser field	$E_L[TV/m] = 3.21 \times a_0/\lambda_0[\mu m]$

LWFA parameter

Matched bubble radius	$R_b[\mu m] = 10 \times \sqrt{a_0/n_e[10^{18}cm^{-3}]}$
Dephasing length	$L_{deph}[\mu m] = \frac{2}{3} \times R_b[\mu m] \times \lambda_P^2[\mu m]/\lambda_0^2[\mu m]$
Pump depletion length	$L_{pd}[\mu m] = 0.3 \times \tau[fs] \times \lambda_P^2[\mu m]/\lambda_0^2[\mu m]$
Maximum energy gain	$\Delta E[GeV] = 1.7 \times \left(\frac{P}{[100TW]}\right)^{1/3} \left(\frac{n_e}{[10^{18}cm^{-3}]}\right)^{-2/3} \left(\frac{\lambda_0}{[0\,8\mu m]}\right)^{4/3}$
Optimal beam loading	$Q_s[pC] = 1.54 \times \lambda_0[\mu m] \times \sqrt{P[GW]}$

Betatron radiation

Betatron wavelength	$\lambda_\beta[\mu m] = 471 \times \sqrt{\gamma/n_e[10^{18}cm^{-3}]}$
Critical energy	$E_c[keV] = 5.24 \times 10^{-6} \times \gamma^2 \times n_e[10^{18}cm^{-3}] \times r_\beta[\mu m]$
Wiggler strength	$K = 0.133 \times \sqrt{\gamma \times n_e[10^{18}cm^{-3}]} \times r_\beta[\mu m]$

ACKNOWLEDGMENTS – DANKSAGUNG – MERCI

Ich danke Prof. Dr. Ulrich Schramm und Prof. Dr. Thomas Cowan für die Möglichkeit zur Promotion und zur Vertiefung meiner Arbeit in die Laser-Elektronen-Beschleunigung.

Special thanks goes to my experimental supervisor Dr. Arie Irman for facilitating the experimental cave and experiments. Thank you Arie for your help and advice throughout my work.

Für die konstruktive Zusammenarbeit im Büro danke ich: Lieselotte Obst-Hübl, Martin Rehwald, Omid Zarini und Tim Ziegler.

Many thanks to the electron team for their great support during experimental campaigns: Jurjen P. Couperus Cabadağ, Omid Zarini, Axel Jochmann, Jakob Krämer as well as Thomas Kurz, Susanne Schöbel and Vincent Chang.

Für das Verbessern des (auch theoretischen) Verständnisses und für eine Vielzahl von PIConGPU Simulationen danke ich: Richard Pausch, Alexander Debus, Klaus Steiniger, Marco Garten, Malte Zacharias, Axel Hübl und Michael Bussmann.

Special thanks go to Prof. Michael Downer from the University of Texas at Austin and his great team: Rafal Zgadzaj, Andrea Hannasch and Maxwell LaBerge.

Vielen Dank an das Laser Team, das den Draco Laser zu seiner unglaublichen Leistung gebracht hat: René Gebhardt, Uwe Helbig, Thomas Püschel und Stefan Bock. Christoph Eisenmann, Simon Grams, Gunter Harzendorf, Harald Nehring und Manfred Sobiella danke ich für Antworten, Lösungen und Hilfe bei technischen Problemen beim Vorbereiten von Experimenten. Jörg Grenzer und Andreas Wagner danke ich für die Unterstützung bei meinen ersten Versuchen mit Röntgenstrahlung für den Betatronprofiler. Thank you, Katerina Falk and Michal Smid, for your great expertise and helping hand for setting up the first experiments with betatron radiation as a probe source for XAS and WDM. Für die gute Zusammenarbeit bedanke ich mich bei Stephan Kraft, Hans-Peter Schlenvoigt, Florian Kroll, Alessandro Laso Garcia, Anna Ferrari, Irene Prencipe, Melanie Rödel, Diana Jahn, Karl Zeil, Josephine Metzkes-Ng und Nicholas Hartley. Der Graduiertenakademie danke ich für die Kurse, die ich besuchen konnte.

Der AG DSN und im speziellen Hagen danke ich für die Unterstützung, die ich bei der Organisierung der LPI-Vorlesungen erhalten habe und die vielen Aktivitäten rund um das Netz der Studentenwohnheime. Nora, Hannah, Clements und den anderen aus den Theaterkurs danke ich für die schöne Zeit und den vielen Spaß, den wir zusammen auf der Bühne hatten und hoffentlich noch haben werden. Ich danke meinen Freunden Anne, Claudi, Claudia, Frank, Gertrude, Kathleen, Lars, Maria, Marie, Peter und Torsten für die schönen Momente und Unternehmungen, die das Leben lebenswert machen. La vie, c'est un chemin plein de découvertes.

Ein großer Dank gehört meiner Familie, vorallem für die Unterstützung, die sie mir entgegen gebracht hat. Ohne sie wäre ich nicht hier. Danke Sibel, dass du die Hochs und Tiefs der Dissertation mit mir durchgemacht hast. Danke für dein Verständnis, dass die lange Schreibphase mitgemacht hast und mich nach aller Kraft unterstützt hast. Es gibt so viel, wofür ich dir danke.
Teşekkür ederim, Sibel!

Erklärungen

Hiermit versichere ich, dass ich die vorliegende Arbeit ohne unzulässige Hilfe Dritter und ohne Benutzung anderer als der angegebenen Hilfsmittel angefertigt habe; die aus fremden Quellen direkt oder indirekt übernommenen Gedanken sind als solche kenntlich gemacht. Die Arbeit wurde bisher weder im Inland noch im Ausland in gleicher oder ähnlicher Form einer anderen Prüfungsbehörde vorgelegt.
Die Dissertation wurde unter der wissenschaftlichen Betreuung von Prof. Dr. Ulrich Schramm und Dr. Arie Irman am Helmholtz-Zentrum Dresden–Rossendorf angefertigt.
Die Promotionsordnung der Fakultät Mathematik und Naturwissenschaften an der Technischen Universität Dresden vom Februar 2011 mit letzten Änderungen vom Juni 2014 erkenne ich an.

Dresden, der 25.01.2019

Alexander Köhler

HZDR
HELMHOLTZ
ZENTRUM DRESDEN
ROSSENDORF

Bautzner Landstr. 400
01328 Dresden, Germany
Tel. +49 351 260-3663
Fax +49 351 260-13663
a.koehler@hzdr.de
http://www.hzdr.de